PHARMACOLOGICAL INTERVENTION OF ARRHYTHMIAS

by

Ashish Parikh

Bachelor of Biomedical Engineering, University of Mumbai, 2006

Master of Biomedical Engineering, Cornell University, 2007

Submitted to the Graduate Faculty of

The Swanson School of Engineering in partial fulfillment

of the requirements for the degree of

Doctor of Philosophy

University of Pittsburgh

2012

UNIVERSITY OF PITTSBURGH

SWANSON SCHOOL OF ENGINEERING

This dissertation was presented

by

Ashish Parikh

It was defended on

June 27, 2012

and approved by

Harvey Borovetz, PhD, Chair, Department of Bioengineering

Barry London, MD, PhD, Professor, Department of Medicine

Sanjeev Shroff, PhD, Associate Chair, Department of Bioengineering

Dissertation Director: Guy Salama, PhD, Professor, Department of Medicine

PHARMACOLOGICAL INTERVENTIONS OF ARRHYTHMIAS

Ashish Parikh, PhD

University of Pittsburgh, 2012

Multiple mechanisms have been implicated in the genesis of early afterdepolarizations (EADs) leading to torsade de pointes (TdP) under long QT syndrome (LQTS). In atrial fibrillation (AF), recent studies have provided new insights into the molecular determinants of atrial structural remodeling pointing out to the importance of fibrosis, as both a cause and a therapeutic target. Physiological experiments combined with mathematical modeling have direct implications to the understanding the effect of drugs and to the treatment of cardiac arrhythmias.

Ranolazine (Ran) approved by the FDA in 2006 as an anti-anginal and anti-ischemic drug, is known to inhibit multiple ionic currents. Functionally, Ran has been shown to suppress EADs in drug-induced long QT type 2 (LQT2), however, its mode of action still remains unknown. Our studies indicated that Ran reduces the open probability (Po) of ryanodine receptors (RyR2), inhibits the SR Ca^{2+} overload and combined with its effect on late sodium current ($I_{Na,Late}$) suppressed EADs. Reactivation of the L-type Ca^{2+} channel ($I_{Ca,L}$) has also been shown to play a major role in EAD formation under LQTS. In several pathological conditions, $I_{Ca,L}$ has a larger window current promoting Ca^{2+} overload and EADs. Dauricine (Dau), a Chinese herb has been shown to impart antiarrhythmic properties. Our experimental studies confirmed that Dau suppressed EADs primarily by reducing $I_{Ca,L}$ by slowing down its kinetics. Further investigation suggested that a minor shift in voltage-dependent activation and/or

inactivation parameters can suppress EADs and can be utilized as a novel antiarrhythmic strategy.

Atrial Fibrillation (AF) is associated with substantial cardiovascular morbidity and mortality. In this study, we tested the hypothesis that atrial fibrosis plays a key role in AF inducibility in spontaneously hypertensive rats (SHR) and evaluated the efficacy of relaxin (RLX) at reducing AF inducibility by reducing fibrosis. Wistar Kyoto (WKY), SHR, and SHR treated with RLX (SHR+RLX) were optically mapped, tested for AF inducibility. SHR had slower conduction velocity (CV), higher fibrosis and a greater AF inducibility compared to WKY. RLX-treatment significantly reduced fibrosis levels, improved CV, and attenuated the AF inducibility in SHR. These studies demonstrate the relationship between fibrosis and AF and provide compelling evidence that reversal of fibrosis, by drugs such as RLX may provide a novel therapy in the management of AF.

TABLE OF CONTENTS

LIST OF TABLES

LIST OF FIGURES

PREFACE

I would like to thank my advisor Dr. Guy Salama for providing me with the opportunity to work in his laboratory. I am extremely grateful to him for keeping me focused on my projects, helping me develop my scientific writing skills and develop expertise in the area of cardiac electrophysiology.

I would also like to thank the members of my advisory committee Dr. Harvey Borovetz, Dr. Sanjeev Shroff and Dr. Barry London for their guidance and suggestions for my dissertation. I would like to acknowledge Jamie Haney, Wenyu Xiang, Dr. Jose Luis Puglisi, Dr. Alain Karma, Dr. Charles McTiernan, Dr. Sanjeev Shroff, and Dr. David Schwartzman for their endeavors on our projects.

I am grateful to the members of the Salamalab, especially Divyang Patel, Bethann Gabris, Dr. Rita Papp and Dr. Jan Němec for making my experience working in the lab extremely worthwhile and rewarding. I would also like to thank the Department of Bioengineering especially Dr. Sanjeev Shroff for their support and guidance.

I thank my parents, my brother, sister in law, cousins and friends without whom none of this would have been possible.

1.0 INTRODUCTION

The long QT 2 (LQT2 type) is the second most common type of congenital long QT syndrome (LQT), comprising about 25 to 30 percent of all cases. This form of LQT involves mutations of the human ether-a-go-go related gene (*hERG*) also known as *KCNH2* on the long arm of chromosome 7. The *hERG* gene product, Kv11.1 is the pore-forming subunit of the I_{Kr} potassium channel (the rapid component of the delayed rectifier current). The I_{Kr} current is mainly responsible for the termination of the cardiac action potential, and therefore the length of the QT interval. Many substances used in clinical medicine inhibit I_{Kr} causing drug-induced LQT2.[1, 2]

Factors that prolong the duration of the action potential (AP), mainly by delaying the repolarization phase 3, and increasing duration of the plateau phase 2 would lead to QT prolongation. Thus, potential proarrhythmic indicators at the protein level would include changes in ion channel properties consistent with increases in AP phases 1, 2 and/or 3. Phase 1 is the notch caused by transient outward potassium current (I_{to}). The plateau phase, phase 2, is maintained by inward Ca^{2+} current flowing through L-type Ca^{2+} channels ($I_{Ca,L}$) that inactivate slowly and outward K^+ flowing potassium channels primarily via the inward rectifier current (I_{K1}) and followed by the delayed potassium currents I_{Kr} and I_{Ks}. Thus, proarrhythmic conditions associated with phase 2 sustained depolarization include increases in maximum conductances of $I_{Ca,L}$ and I_{Na}, and changes in gating parameters consistent with slowing of inactivation and/or

increases in the reversibility of inactivation. Repolarization (phase 3) is accomplished through the activity of two types of outward potassium currents, I_{Kr}, and I_{Ks}.[3] Prolongation of the action potential can result from decreased inactivation of the inward Na^+ or Ca^{2+} currents, increased activation of the Ca^{2+} current, or inhibition of one or more of the outward K^+ currents. The rapid and slow components of the delayed rectifying potassium current, I_{Kr} and I_{Ks}, play a crucial role in determining the duration of the action potential and thus the QT interval.

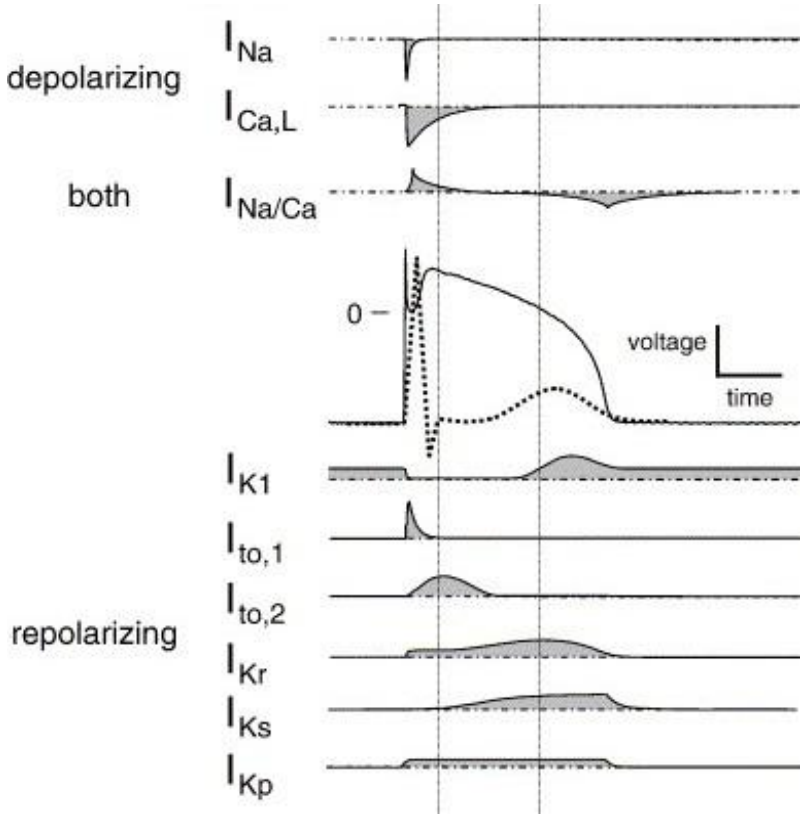

Figure 1: Ventricular action potential

A schematic of the activity of the currents during an action potential
Reproduced with permission from Kinter et al

While there is a general consensus in the literature that EADs are the events that initiate Torsade de Pointes (TdP), controversy still exists regarding the initiation of EADs. Experiments have suggested that EADs occurs primarily at the conduction system. However, dual optical mapping of APs and intracellular Ca^{2+} (Ca_i) showed that Ca_i rises before the rise of EADs and that the occurrence of EADs was the same in intact hearts and hearts with cryoablated Purkinje fibers.[4] Recently our lab has shown that in LQT2, Ca_i oscillations (Ca_iO) precede EADs by minutes, indicating that they result from spontaneous sarcoplasmic reticulum Ca^{2+} release rather than spontaneous $I_{Ca,L}$ reactivation. Ca_iO leads to oscillations in I_{NCX}. Depolarizing I_{NCX} during the AP plateau contributes to the generation of EADs by re-activating Ca^{2+} channels that have recovered from inactivation.[5] The arrhythmia phenotype is the result of complex interplay between a loss of function of I_{Kr} and an up-regulation of $I_{Ca,L}$ and $I_{NCX.}$

1.1 PREDICTORS OF DRUG-INDUCED TDP

The concept of '*repolarization reserve'* was introduced to explain congenital variability and sex-differences in the response to reduced or loss of function of I_{Kr}.[6] Reduced I_{Kr} may not lead to clinical consequences, if, as proposed, I_{Ks} remains intact and functions as a major source of 'repolarization reserve' that protects against Torsade de Pointes (TdP) during I_{Kr} block.[7] However, it should be emphasized that I_{Ks} is typically a very weak current until activated by β-adrenergic agonist and is heterogeneously distributed, being high at the base and low at the apex of the ventricles.[8, 9] Multiple mechanisms are increasingly recognized as contributing to normal repolarization. It is clear that none of the 'gold standard' QT-related assays (*hERG*, APD and in vivo QT assays) alone can sufficiently predict the risk of TdP nor is there consensus on the

parameters that best predict proarrhythmia, highlighting the complexity of the issue and the need for proarrhythmic models that encompass most if not all of the predisposing factors. The emergence of proarrhythmic models and in particular *in vitro* and *in silico* models is a testament to the prevalence of the problem and the urgency with which it is being tackled.[7]

In addition to the prolongation of APDs, it is now recognized that transmural and apex-base dispersion of repolarization (DOR) and other properties, such as EADs, reverse frequency dependence, and triangulation of the AP, are associated with TdP.[8, 10] Although there may be disagreement on which is the most predictive proarrhythmic model or which variable(s) are of greater importance, there is a general consensus that a key event linked to the induction of TdP is the development of EADs. EADs have been identified in every model as being the primary trigger of TdP.[11] Of equal importance is to identify the components critical to the development of EADs and to target them as an antiarrhythmic therapy to prevent TdP.

1.2 DRUG INDUCED QT PROLONGATION AND TDP

The congenital and drug induced forms of LQT2 are associated with an increased risk of polymorphic ventricular tachyarrhythmia (PVT), called TdP. Pharmacological agents were developed to inhibit I_{Kr}, prolong QT interval to presumably increase refractoriness and to act as antiarrhythmic. These agents called class III antiarrhythmics where found to be highly proarrhythmic in clinical tests due to LQT-related EADs that progressed to TdP. Quinidine, Dofetilide and E4031 are examples of such drugs. Besides class III agents, many non-cardiac drugs have also been reported to cause QT prolongation and/or TdP by blocking I_{Kr}. It has since become apparent that *hERG* is a promiscuous peptide that readily interacts with a wide range of

compounds to prolong APD. The danger of drug induced pro-arrhythmia is therefore widespread and remains a serious problem. However, an increase in the QT interval does not necessarily lead to TdP, and the correlation between the degree of QT prolongation and the risk of TdP is relatively weak.[12] This issue has been identified as a considerable public health problem and has attracted attention from the drug regulatory authorities. Several *in vitro* strategies are currently being used to assess the proarrhythmic risk of new compounds. These include (i) the arterially perfused left ventricular wedge preparation, (ii) SCREENIT, a Langendorff-perfused isolated rabbit heart preparation and (iii) a Langendorff-perfused isolated rabbit heart preparation using bradycardia and hypokalemia. The rabbit heart has been routinely used in langendorff preparations, primarily because of its sensitivity to TdP-like arrhythmias and its similarities to human hearts. This sensitivity results from the rabbit heart having long APD, very low expression of I_{Ks} (slow component of the delayed rectifier potassium current) at the abse of the heart and a repolarization reserve similar to man.[7] The ICHS7B guideline recommends a non-clinical evaluation of the potential for delayed ventricular repolarization to 1) identify the potential of a test substance and its metabolites to delay ventricular repolarization, and 2) relate the extent of delayed ventricular repolarization to the concentrations of a test substance and its metabolites. The study results can be used to elucidate the mechanism of action and, when considered with other information, estimate risk for delayed ventricular repolarization and QT interval prolongation in humans (QT Interval Prolongation) by pharmaceutical therapeutics.[13]

1.3 OPTICAL MAPPING

Optical mapping is an especially powerful tool in studies of electrophysiology. Due to overwhelming stimulus-induced artifacts, the conventional electrode techniques are not able to record electrical activity during and immediately after a stimulus. In contrast, optical recordings provide an accurate account of transmembrane potential changes and calcium transients (Ca_iT) in the heart.

Fluorescence imaging at high spatial resolution but low dynamic range and low temporal resolution was first used to visualize ocular dominance and orientation selectivity from the primate visual cortex using a video camera. Development of CMOS cameras offer considerable advantages compared to CCDs, photodiode arrays and video cameras by achieving outstanding acquisition rates (up to 10,000 fps), high dynamic range (10^5), high spatial resolution (100x100 pixels), low background noise, and large pixel dimensions.

Application of CMOS cameras of high spatio-temporal resolution compared to CCDs, photodiode arrays assures the accuracy of the recordings. Depending on optical magnification, the fluorescent signal comes from hundreds or thousands of cells or from multiple sites on a single myocyte. Also, based on the scan length, multiple action potentials can be recorded as a function of time from each pixel.

1.4 CARDIAC ELECTROPHYSIOLOGY MODELS

Mathematical modeling of cardiac cellular electrophysiology has undergone significant development over the last few years driven by major technological developments that have

provided improved experimental techniques and ever-increasing computational power. Improved experimental techniques have allowed scientists to examine cellular structure and function from the whole cell down to individual molecules and atoms while increased computational power has provided modelers with a critical tool required for the analysis of an immense amount of experimental data available. Over the last 50 years, the use of computer modeling to better understand the heart and its functions has reached a high level of complexity. Furthermore, experimental cardiac electrophysiology has been increasingly complemented by computational models of action potential propagation that embed models of membrane excitability within a framework that describes cardiac tissue and can provide a quantitative description of action potential propagation, and have explanatory power because they can be used to test and generate hypotheses that are difficult to address experimentally.[14] These models are becoming increasingly useful tools with an important part to play in understanding human physiology, whilst reducing and replacing animal use in cardiac electrophysiology, and possibly in the study of other diseases and organ systems in the future. While it appears straightforward to build models of cardiac tissue electrophysiology, these models embed several important assumptions which limit their applicability in clinical situations.[15] Computational models for profiling proarrhythmic risk have made significant advances in recent years. Highly sophisticated *in silico* models have been developed to predict *hERG* channel activity[16], AP duration in rabbit[17-19], canine[20], and human ventricular myocytes[21, 22] and electrical wave propagation throughout the intact myocardium.[23, 24] These models may be useful to examine the mechanism of a particular aspect of cardiac function. However, biological systems are vastly more complex than any modeled system and so it is extremely unlikely that we will be able to reproduce the complex properties found in nature with high fidelity with just a few decades of investigations.

1.5 MODELS OF APs AND Ca_iT

Models of APs and Ca_iT are based on ionic currents, ionic concentrations, subcellular organelles, membrane processes and other processes which regulate intercellular Ca^{2+} concentration. All models depict ionic fluxes of each species as independent of the others. When a current *I* is included as one of the reactions in a model, that current will appear on the right hand side (RHS) of 2 ordinary differential equations (ODEs): *dV/dt* (voltage) and *d[c]/dt* (where *[c]* is an ionic concentration). Equation 1 is a representative of the monovalent time- independent Nernst current and applies to all the ionic currents; hence a similar equation is used for Na^+, K^+, Ca^{2+} and Cl^-. For this current,

$$I = G g_\infty \left(V - \frac{RT}{F} \ln \frac{c_0}{c_i}\right) \qquad \textit{Equation 1}$$

where

$$g_\infty = \frac{1}{1 + e^{-(V - V_{1/2})}} \qquad \textit{Equation 2}$$

G, n, $[c]_o$, $V_{1/2}$, are parameters. *[c]* and *V* (voltage) are state variables. *T, R,* and *F* are constants.

Several models of ion channel dynamics are used in the literature. The original Hodgkin-Huxley formulation [25] assumed that the transition from a closed state [C] to an open state [O] (and vice versa) were determined by a voltage dependent rate constant $\alpha(V)$ and ($\beta(V)$ for the reverse reaction) that depended exponentially on V. The differential equation that results from this model (assuming only 1 open and 1 closed state) is,

$$[\dot{O}] = \propto (1 - [O]) - \beta [O] \qquad \textit{Equation 3}$$

can then be reorganized in terms of new quantities $[O]_{inf}$ and τ, such that

$$O_{inf} = \frac{1}{1 + \frac{\beta(V)}{\alpha(V)}}$$ *Equation 4*

$$\tau = \frac{1}{\alpha(V) + \beta(V)}$$ *Equation 5*

However, investigators have generalized this model such that the quantities [O]inf and τ no longer are forced to take on the form given above. [26, 27] Therefore, we will define any transition between any states of an ion channel in which the rate constants are exponential functions of V to be of "Markov type". An example of a Markov formulation is given below:

$$C \underset{\beta}{\overset{\alpha}{\leftrightarrow}} O$$ *Equation 6*

$$\alpha = e^{a1+b1V}$$

$$\beta = e^{a2+b2V}$$ *Equation 7*

$$\dot{C} = -\alpha C + \beta O$$

$$\dot{O} = \alpha C - \beta O$$ *Equation 8*

2.0 RANOLAZINE STABILIZES CARDIAC RYANODINE RECEPTORS: A NOVEL MECHANISM FOR THE SUPPRESSION OF EADS AND TDP IN LONG QT TYPE 2

2.1 SPECIFIC AIMS

Ranolazine (Ran) is known to inhibit multiple targets, including: the late Na^+ current, $I_{Na,Late}$, the rapid delayed rectifying K^+ current, I_{Kr}, L-type Ca^{2+} current, $I_{Ca,L}$, and fatty-acid metabolism. Functionally, Ran suppresses EADs during phase 2 and/or phase 3 and TdP in drug-induced LQT2, presumably by decreasing intracellular $[Na^+]_i$ and Ca^{2+} overload.

The goal of the proposed research was to compare the available *in silico* models of rabbit ventricular myocytes to experimental data and to elucidate the mechanism(s) whereby Ran alters APs, Ca_iT and suppresses EADs and (TdP) in LQT2 using optical mapping and mathematical modeling.

Aim 1: To test the hypothesis that in LQT2 (or I_{Kr} inhibition) elevation of $I_{Ca,L}$ promotes EADs based on the best available *in silico* models of ventricular APs and Ca_i handling.

Several *in silico* models for the rabbit cardiac ventricular myocytes were tested and the best available model based was selected based on its ability to predict correct AP and Ca^{2+} dynamics. The AP and Ca_iT were quantitatively and qualitatively compared with experimental data recorded at 3 different heart rates. The model/models that best predicted the correct Ca^{2+}

dynamics were used for further studies. The models were also tested for their ability to generate EADs based on the inhibition of I_{Kr} and elevation of $I_{Ca,L.}$

Aim 2: To test the hypothesis that Ran suppresses arrhythmias in a drug-induced LQT2 using optical mapping and elucidate its mode of action using bilayer studies and mathematical modeling.

A therapeutic concentration of Ran was tested in rabbit hearts to study its effect on a) APD, Ca_iT, Ca_i rise time and V_m-Ca_i delay, b) antiarrhythmic properties in the suppression of arrhythmias in a model of drug-induced LQT2 and c) it's effect on the open probability of ryanodine receptors (RyR2). The action of Ran on various ionic currents and RyR2 was modelled in a step wise manner in the best available *in silico* model as determined from Aim 1 and was used to explain its primary mode of action.

2.2 INTRODUCTION

Ran (2-6 µM) is approved for the treatment of *angina pectoris* and ischemic heart disease, but its exact therapeutic mode of action remains controversial. Early studies suggested that Ran altered myocardial energy metabolism by reducing fatty acid oxidation and glucose oxidation.[37] The inhibition of fatty oxidation by Ran appeared at relatively high concentrations (12% inhibition at 100 µM) which brought into question the validity of this mode of action.[37-39] Alternatively, Ran at therapeutic doses (<10 µM) was shown to inhibit $I_{Na,Late}$.[40] Besides its efficacy in the treatment of angina pectoris, Ran suppressed EADs and TdP in animal models of acquired LQT2[41] despite its tendency to prolong the QT interval by inhibiting I_{Kr}.[42]

Ryanodine receptor (RyR2) plays a major role in cytosolic Ca^{2+} release and is critical in arrhythmogenesis of different pathologies and as a target of antiarrhythmic drugs. Ca^{2+} released from the sarcoplasmic reticulum (SR) occurs in a wavelike form with a swing of levels from 100 nM to 1 μM. For ventricular contraction, Ca^{2+} release occurs via the entry of extra cellular Ca^{2+} via $I_{Ca,L}$ in small sparks[28] that unleash a large release from SR via RyR2 [29] and the withdrawal via SERCA pump[30, 31]. The amplitude of the transient is governed several factors – SR calcium load[32], luminal Ca^{2+} [33, 34], and is proportional to the contractility [31, 35, 36]. The inhibition of the $I_{Na,Late}$ window results in a decrease of intracellular Na^{+} and improved extrusion of Ca^{2+} via I_{NCX}.[43-45] Inhibition of $I_{Na,Late}$ could account for the therapeutic effects of Ran because it would lead to a reduced Ca_i load, which would reduce bioenergetic stress, protect the heart from ischemic injury, and suppress the incidence of EADs. But, contrary to expectations, ranolazine had no significant effect on peak Ca_i. This observation lead us to the hypothesis that ranolazine lowered the SR Ca^{2+} leak, primarily by reducing the open probability of RyR2.

Modeling the actions of Ran based on its IC_{50} values at its known targets failed to predict Ran's suppression of EADs in LQT2. We hypothesize that antiarrhythmic effect of Ran in the setting of LQT2 cannot be understood without including additional sites of action that alter intracellular Ca^{2+} handling, which to date have not been identified.

2.3 MATERIALS AND METHODS

2.3.1 Heart preparations and optical mapping

New Zealand White rabbits, (adult females >60 days old, ~2kg) were injected with pentobarbital (35 mg kg^{-1}, I.V.) and heparin (200 U kg^{-1}) via an ear vein; the heart was excised and retrogradely perfused through the aorta with Tyrode's solution (in mM): 130 NaCl, 24 $NaHCO_3$, 1.0 $MgCl_2$, 4.0 KCl, 1.2 NaH_2PO_4, 50 dextrose, 1.25 $CaCl_2$, at pH 7.4, gassed with 95% O_2 and 5 % CO_2. Temperature was maintained at 37.0 ± 2 °C and perfusion pressure was adjusted to ~70 mmHg with a peristaltic pump.[46] The atrio-ventricular node was ablated by cauterization to control rate (500-2000 ms). The heart was stained with a bolus of a voltage-sensitive dye (RH 237 or PGHI; 50 µl of 1 $mgml^{-1}$ in dimethyl sulfoxide, DMSO) and a Ca^{2+} indicator (Rhod-2/AM, 300 µl of 1 $mgml^{-1}$ in DMSO) delivered through the bubble trap, above the aortic cannula. The hearts were oriented to view the anterior surface, record control APs and Ca_iT then add E4031 (0.5 µM) and/or Ran to the perfusate. E4031 was purchased from Sigma-Aldrich (St Louis, MO) and Ran was the kind gift of Dr. Luiz Belardinelli (Gilead Sciences, Palo Alto, CA). The optical apparatus based on 2 (16x16 pixels) photodiode arrays has been previously described.[46, 47] Each pixel viewed a 0.9x0.9 mm^2 area of myocardium and images were acquired at 1,000 frames/s.

2.3.2 Single channel recordings of cardiac ryanodine receptors (RyR2)

Cardiac SR vesicles (5-10 µg/ml) isolated from sheep ventricles [48] were added to the *cis*-chamber of a planar bilayer setup containing 400 mM $Cs^+CH_3O_3S^-$, 25 mM Hepes, pH 7.4, while

the *trans*-side contained 40 mM $Cs^+CH_3O_3S^-$, 25 mM Hepes, pH 7.4. Bilayers were made of 5:3:2 phosphatidylethanolamine (PE): phosphatidylserine (PS): phosphatidylcholine (PC) (Avanti Polar Lipids – Coagulation reagent 1) painted across a 150 µm hole separating two compartments. Following fusion of an SR vesicle to the bilayer, 4M $Cs^+CH_3O_3S^-$, 25mM Hepes, pH 7.4 was added to the *trans*-side to equalize the salt concentration at 400 mM. Channel output was filtered at 0.8-1.0 kHz and traces were recorded at a holding potential of -40 mV, for not less than three minutes following an addition of Ran to the *cis*-chamber. Single channel analysis was carried out using the ClampFit program (Axon Instruments: pClamp software). The P_o (mean ± SE) normalized to 1 (control without Ran) was plotted as a function of [Ran] (n = 7).[49]

2.3.3 Ca^{2+} dependent ryanodine binding to RyR2

Equilibrium ryanodine-binding was measured as a function of free Ca^{2+} (Ca_f) in buffer containing 250 mM KCl, 15 mM NaCl, 2 nM [^{3}H]ryanodine, 13 nM unlabeled ryanodine, 20 mM PIPES, pH 7.1 ± 30 µM Ran at an SR concentration of 0.5 mg/ml, following 3 hours incubation at 37^{o}C.[50] Nonspecific binding, measured in the presence of 200 nM unlabeled ryanodine and 50 µM Ca^{2+}+ 4 mM EGTA, was subtracted from all measurements. Ca^{2+} was buffered with EGTA and Ca_f was calculated with established binding constants and measured with a Ca^{2+}-selective electrode.

2.3.4 Mathematical modeling

The mathematical representation of a typical ionic current is based upon the Hodgkin Huxley representation,

*Current = Conductance * Driving Force*

For instance, the kinetics of the rapid delayed rectifier current I_{Kr} is shown below,

$$I_{Kr} = G_{Kr} * X * R *(V - E_{Kr})$$ *Equation 9*

G_{Kr} = Conductance of the channel, X = activation gate of I_{Kr}, R = inactivation gate of I_{Kr}, V= Membrane potential, E_{Kr}= Reversal potential of potassium.

In order to mimic low expression levels of the I_{Kr} (the blockade of the I_{Kr} channel), we multiply the conductance by a numerical value < 1. For 50% blockade of I_{Kr}, G_{Kr} is multiplied by a numerical value of 0.50; for 40% blockade 0.6. Similarly, to increase the expression levels of $I_{Ca,L}$, the conductance of L-type calcium channel is multiplied by a numerical value > 1. For 10% increase in $I_{Ca,L}$, we multiply the conductance by 1.10; for 30% increase, we multiply by 1.30.

APs and Ca_iT predicted by the *Shannon*[17] and *Mahajan*[51] models were compared to optical recordings at various CLs (500, 1000, 2000 ms). Simulations of LQT2 included: a) a 50 % decrease of I_{Kr}, to mimic the effect of E4031, b) a 32% increase of $I_{Ca,L}$ to mimic the increase in $I_{Ca,L}$ expression measured in females hearts and shown to be a key factor for the higher risk of TdP in female hearts,[52] c) an increase in cycle length to 1 or 2s since bradycardia is a critical co-factor to promote EADs. The multifaceted action of Ran was modeled by modifying the channel conductance using the following values: I_{Kr} (IC_{50} = 12 µM), $I_{Na,Late}$ (IC_{50} = 5.9 µM), $I_{Ca,L}$ (IC_{50} = 50 µM), and I_{NCX} (IC_{50} = 91 µM).[42] To incorporate a dose dependent effect the conductance of the major ionic currents (I_{Kr}, $I_{Na,Late}$, $I_{Ca,L}$ and I_{NCX}) was scaled using the equation,

$$G_{i,Ran} = \frac{G_i}{1 + Dose/IC_{50}}$$ *Equation 10*

where $G_{i,\ Ran}$: Conductance of ionic current 'i' with Ranolazine, G_i: Original conductance for current 'i', i = I_{Kr} or $I_{Na,Late}$ or $I_{Ca,L}$ or $I_{NCX.}$

The code for *Shannon* model was provided by Dr. Jose Luis Puglisi (UC Davis, CA) and was compiled in Matlab, while the code for the *Mahajan* model was provided by Dr. Alain Karma (Northeastern University, Boston, MA) and was compiled in C++.

2.3.5 Analysis

APDs, Ca_iT, rise-times, durations, amplitudes and V_m to Ca_i delays were measured at regular intervals. Measurements of duration are expressed as mean ± SEM; Student's t –Test (paired) was applied to determine statistical significance based on $p < 0.05$.

2.4 RESULTS

2.4.1 Effects of ranolazine on APs and Ca_iTs after I_{Kr} block

Figure 2 illustrates representative traces of optical APs and Ca_iT from the base of the left ventricle. Control recordings showed that Ca_iT followed the AP upstroke by 10 ms and recovered after the local repolarization (panel A). E4031 (0.5 μM) added to the perfusate prolonged APD, induced Ca_iT oscillations and elicited EADs (panel B, n = 7/7). The latter increased in frequency degenerating into salvos of EADs (<10 min). However, perfusion with Ran (10 μM) plus E4031 suppressed EADs within 5 min (panel C) and abolished the progressive worsening of the electrical instabilities to TdP. In panels A' to D', the order of addition of the

two drugs was reversed; Ran (10 μM) added alone prolonged APDs (204 ± 6.1 ms to 240 ± 7.8 ms; $p < 0.05$), Ca_iT (249 ± 23.5 ms to 275 ± 43.1 ms) and Ca_i rise-time (26 ± 1.2 ms to 42 ± 3.0 ms; $p < 0.05$) (compare A' to B'). The subsequent addition of E4031 (0.5 μM) failed to prolong APDs and to elicit EADs (panel C'). Ran was then washed out while keeping E4031 resulting in a marked APD prolongation, giving rise to EADs and TdP (panel D'). The washout of Ran exposed the proarrhythmic effect of E4031 and the protective effects of Ran. Table 2 summarizes the statistically significant effects of Ran and E4031 on APDs and Ca_iT.

Table 1: Summary of Parameters - Effect of E4031 and ranolazine

	APD (ms)	**Ca_iT Duration (ms)**	**V_m-Ca_i delay (ms)**	**Ca_iTRise-Time (ms)**
Control (n = 8)	204 ± 6.1	249 ± 23.5	6.3 ± 0.7	26 ± 1.2
E4031 only (n = 7)	546 ± 34.9*	582 ± 21.9*	5.8 ± 0.7	43 ± 2.7*
Ranolazine only (n = 6)	240 ± 7.8 *	275 ± 43.1	5.8 ± 0.8	42 ± 3.0*
E4031+Ranolazine (n = 7)	306 ± 27.1*!	343 ± 51.0*!	6.0 ± 1.3	43 ± 4.6*

* versus Control $p < 0.05$; ‡versus E4031 only $p < 0.05$

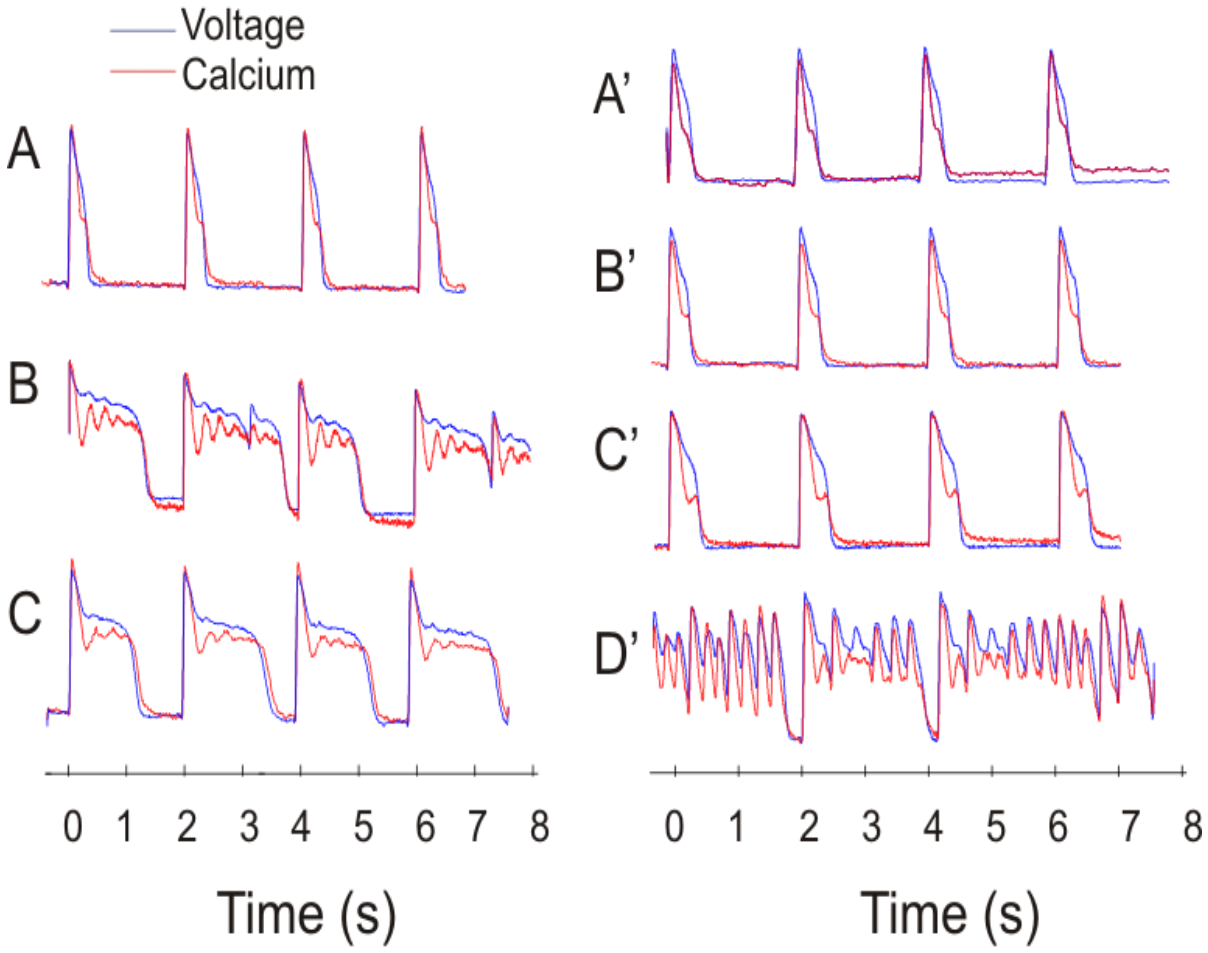

Figure 2: Ranolazine suppresses EADs and TdP in LQT2

Left Panel: V_m (blue) and Ca_i (red) measured from the same site at the base of the heart.
A: Control AP and CaiT with the heart was paced at 2 s CL
B: 10 min after E4031 (0.5 µm)
C: 10 min after E4013 plus Ran (10 µM)
Right Panel: The two drugs were added in the reverse order.
A': Control, 15 min after Ran
B': 10 min after Ran plus E4031
C': 5 min after washout of Ran but with E4031
D': Washout of Ran prolonged APD and unmasked EADs due to the presence of E4031

2.4.2 Modeling I- Selection of the model and modeling the action of ranolazine

Highly sophisticated *in silico* models have been developed to predict the shape and time-course of APs and Ca_iT in ventricular myocytes for different species [53], with the *Shannon* [17] and the *Mahajan*[51] models being specifically designed to incorporate experimentally determined properties of rabbit ventricular myocytes. The *Shannon* model contains a robust representation of excitation-contraction coupling, in which the properties of SR Ca^{2+} release include inactivation/adaptation and a non-linear dependence on SR Ca^{2+}-load. Apart from the addition of a subsarcolemmal compartment to the other two commonly formulated cytosolic compartments (junctional and bulk) because ion channels in the membrane sense ion concentrations that differ from bulk; it also included, a reversible sarcoplasmic reticulum (SR) Ca pump and a scheme for Na-Ca exchange transport that is $[Na]_i$ dependent and allosterically regulated by $[Ca]_i$.

On the other hand, the *Mahajan* model includes a minimal seven-state Markovian model of $I_{Ca,L}$, which incorporates voltage-dependent inactivation (VDI) and Ca^{2+}-dependent inactivation (CDI) and an Ca_i cycling component, to incorporate a phenomenological model emulating local control that produces the appropriate instability leading to Ca_iT alternans at rapid heart rates. Both the models include advanced calcium cycling kinetics, critical for the development of EADs.

Figure 3A compares the APs and Ca_iT obtained with the *Shannon* (a) or *Mahajan* (b) model and the experimental data (c) at three different CLs (500, 1,000 and 2,000 ms). In Figure 3B, APD_{90}, Ca_iTD_{75}, Ca_i rise-time and Peak-Ca_iT amplitude were calculated and compared at the three CLs for the experimental data (blue bars), the *Shannon* (red bars) and the *Mahajan* (green

bars) models. Based on quantitative comparisons, APD_{90} for the two models predicted closely the optical recordings at 500 ms CL, but at 1,000 ms CL, the *Shannon* was close but the *Mahajan* model deviated significantly predicting longer APD_{90} than optical APD_{90} and at 2,000 ms CL, the *Shannon* model underestimated and the *Mahajan* model overestimated the experimental APD_{90} (Figure 3Ba). The duration of Ca_iT measured at 75% recovery to baseline, Ca_iTD_{75} were similar for the *Shannon* and experimental values but the *Mahajan* model deviated significantly, at all three CLs. Similarly, the *Shannon* and experimental values were considerably closer to each other than the values predicted by the *Mahajan* model for the rise time and peak of Ca_iT. For peak-Ca_iT the signals were normalized at 500 ms CL and changes in peak-Ca_iT were compared for the longer CLs. The *Mahajan* model predicted markedly slower rise-times and smaller peak-amplitudes of Ca_iT and rather abnormal shape and time courses of Ca_iT, particularly at longer CLs.

When the models were tested for their ability to mimic experimental LQT2 conditions, the *Shannon* model generated EADs. However, the *Mahajan* model failed to generate EADs (Figure 3C). Upon further inhibition of I_{Kr}, and elevation of $I_{Ca,L,}$ there was an increase in the APD but no EADs appeared (Figure 3C). Based on the closer fit to experimental data and ability to generate EADs, we chose the *Shannon* model to simulate the actions of Ran.

The effect of Ran was simulated based on its IC_{50} values on the major ionic currents.[54] However, the model failed to predict the suppression of EADs by Ran (Figure 4), suggesting that our understanding of the actions of Ran was incomplete within the context of prescribed model parameter changes.

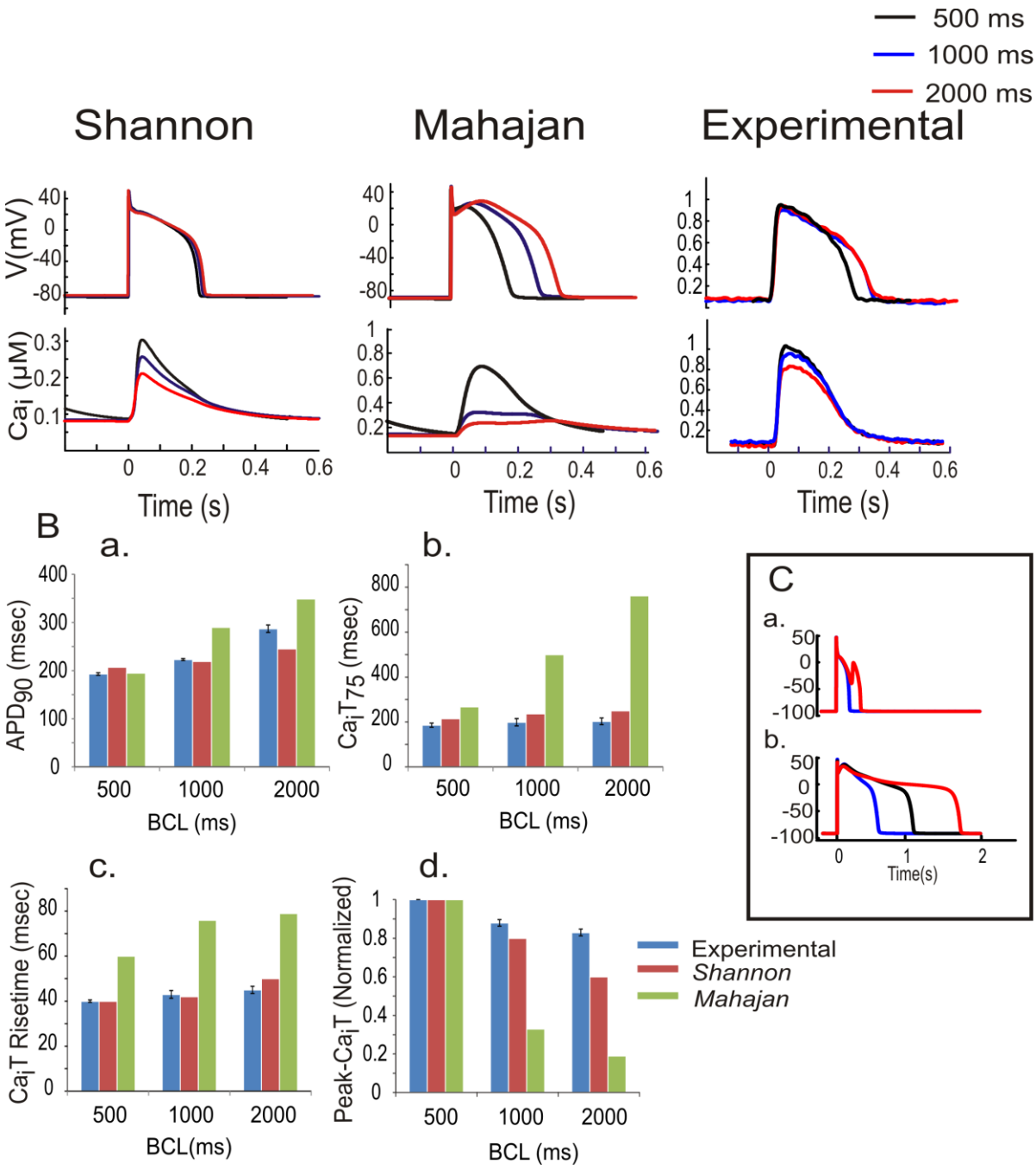

Figure 3: Comparison of mathematical models with experimental data

A: APs (top) and Ca_iT (bottom) derived from Shannon (a) and Mahajan (b) models and optical signals from rabbit hearts (c) at different CLs (500 (black), 1,000 (blue) and 2,000 ms (red)). B: Quantitative comparison of APD_{90} (a), Ca_iT_{75} (b), Ca_iT rise-time (c) and peak-Ca_iT (d) between mathematical models (Shannon, red; Mahajan, green) and experimental data (blue). C: Predicted APs at 2 s CL by the Shannon model (a); control in blue and LQT2 in red and by the Mahajan model (b); control in blue and LQT2 in red.

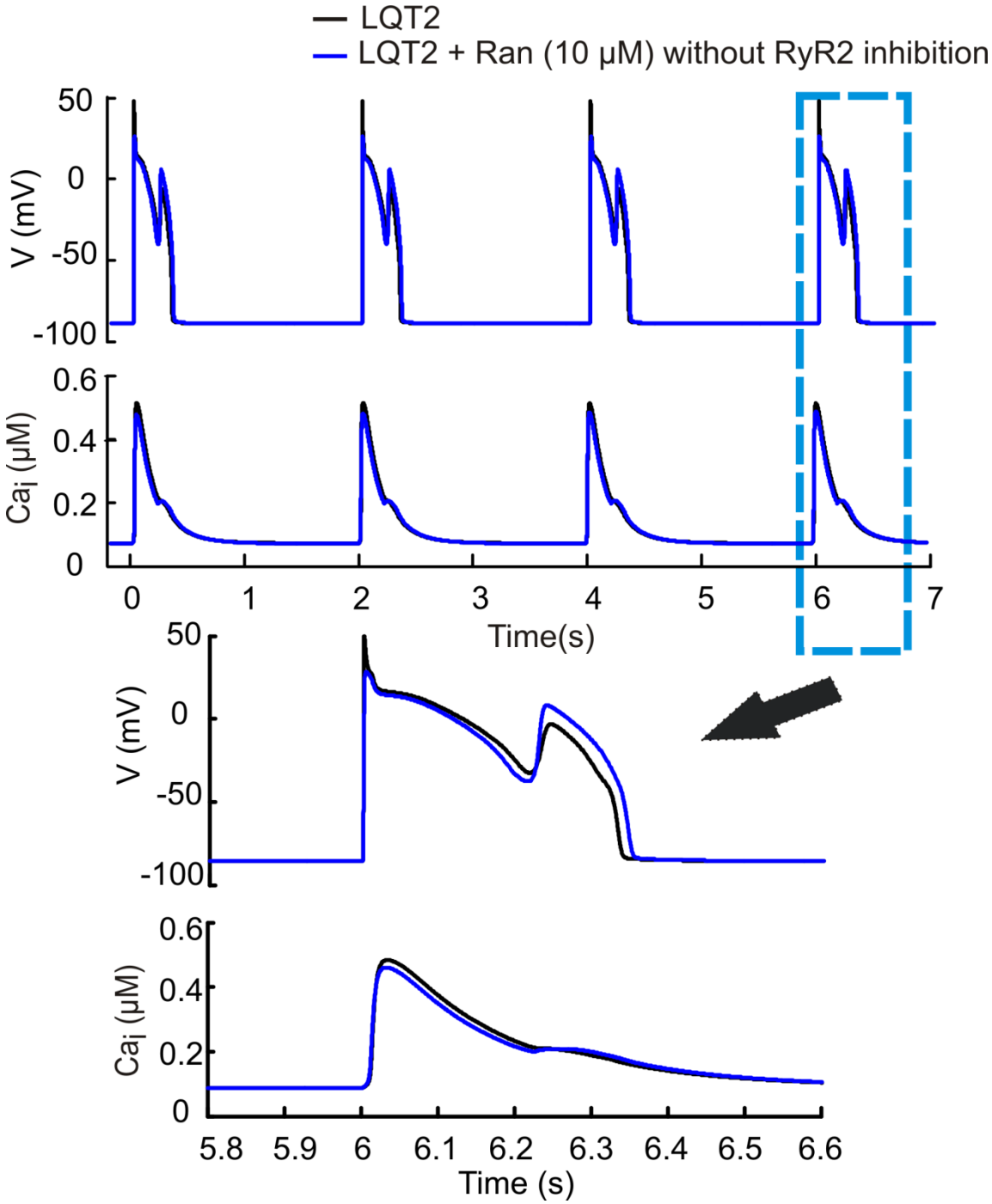

Figure 4: Modeling I - Antiarrhythmic effect of ranolazine

Steady state APs and Ca_iTs for the last four beats in a train of 75 pulses at 2 s CL under LQT2 condition (black); under LQT2 plus 10 μM Ran (blue). Ran failed to suppress EADs.

2.4.3 Effects of ranolazine on RyR2

Cardiac SR vesicles isolated from sheep ventricles were fused to planar bilayers and single channel open-probability (P_o) was recorded in the presence of 50 µM Ca^{2+} on the *cis*-side at pH 7.4. Figure 4A illustrates single channel recordings as a function of [Ran] from the same bilayer. Figure 5B plots the normalized P_o (derived from 2 min of continuous recordings) as a function of [Ran]. The data were fit to a four parameter logistic curve (Sigma-Plot) which yielded an IC_{50} of RyR2 inhibition equal to 10 ± 3 µM (mean ± SE, n = 7). In figure 5C, equilibrium high-affinity ryanodine binding is plotted vs. [Ca^{2+}] in the absence and presence of 30 µM Ran. These data was fitted to a Hill Plot. Ran shifted the EC_{50} for Ca^{2+} dependent activation of ryanodine binding from 0.42 ± 0.02 µM to 0.64 ± 0.02 µM, but has negligible effect on the degree of co-operativity (Hill co-efficient=2.5) or the maximum level of ryanodine binding. At 10 and 30 µM Ran, the Ca^{2+} dependence of [^{3}H] ryanodine binding shifted to the right, respectively by 80 (not shown) and 220 nM Ca^{2+} (Figure 5C).

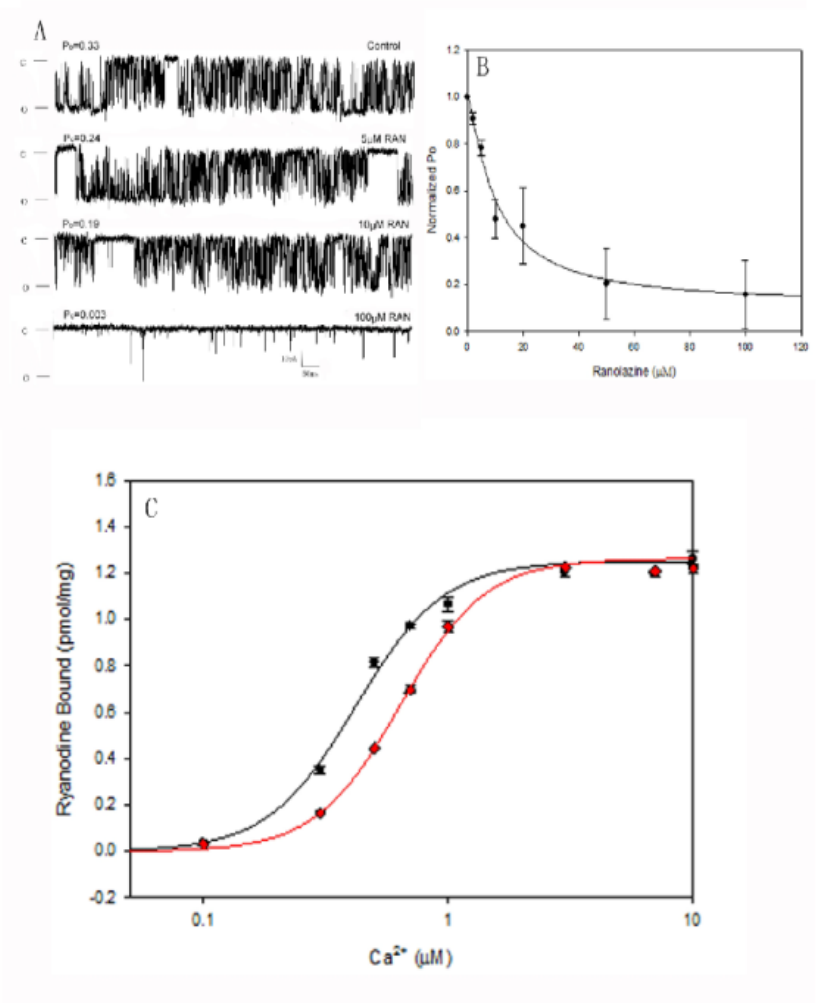

Figure 5: Effects of ranolazine on Po of RyR2 and Ca^{2+}-dependent [3H] ryanodine binding

A: Characteristic single channel fluctuations following fusion of cardiac SR vesicles to a planar bilayer as a function of [Ran]. Po was measured in the presence of 50 μM Ca^{2+} to maintain a highly active channel (i.e. Po ~0.5) and was averaged over 2 min of continuous recordings. c = closed, o = open state.
B: Normalized Po±SE vs. [Ran], n = 7.
C: Ryanodine-binding vs. free [Ca^{2+}] (Ca^{2+}-selective electrode). Ryanodine binding was measured ± 30 μM Ran with SR vesicles (0.5 mg/ml), data are average ± SE (n = 4).

2.4.4 Modeling II

To fully model the effects of Ran, P_o of RyR2 was modified as a function of Ran concentration according to single channel bilayer experiments, in addition to its other targets. The model correctly predicted experimental findings of Ran under normal and LQT2 condition.

In controls (Figure 6), Ran at 5 μM prolonged APD by 8ms and decreased peak-Ca_iT by 17%. While at 10 μM, Ran prolonged APD by 15 ms, increased Ca_iT rise-time by 1.9 fold and decreased peak-Ca_iT by 35%, as previously reported.[54] The simulation also predicted that Ran reduces the AP 'notch' most likely due to its effect of the late Na^+ current, but does not alter the voltage during the AP plateau phase. The effect of Ran on the notch is not detected by optical AP measurements because optical recordings smooth out the notch since they represent the sum of thousands of APs from myocytes under the field-of-view. In LQT2 (Figure 7), Ran (5 μM) decreased Ca_i overload but was not effective at suppressing EADs. At 10 μM, Ran suppressed EADs and reduced Ca_i overload, highlighting a concentration-dependent suppression of EADs. Figure 8 investigates the mechanisms of action of Ran in LQT2 by testing its known effects, except for the inhibition of RyR2, and then including RyR2 inhibition. The stimulation demonstrates that RyR2 inhibition by Ran is required to suppress EADs.

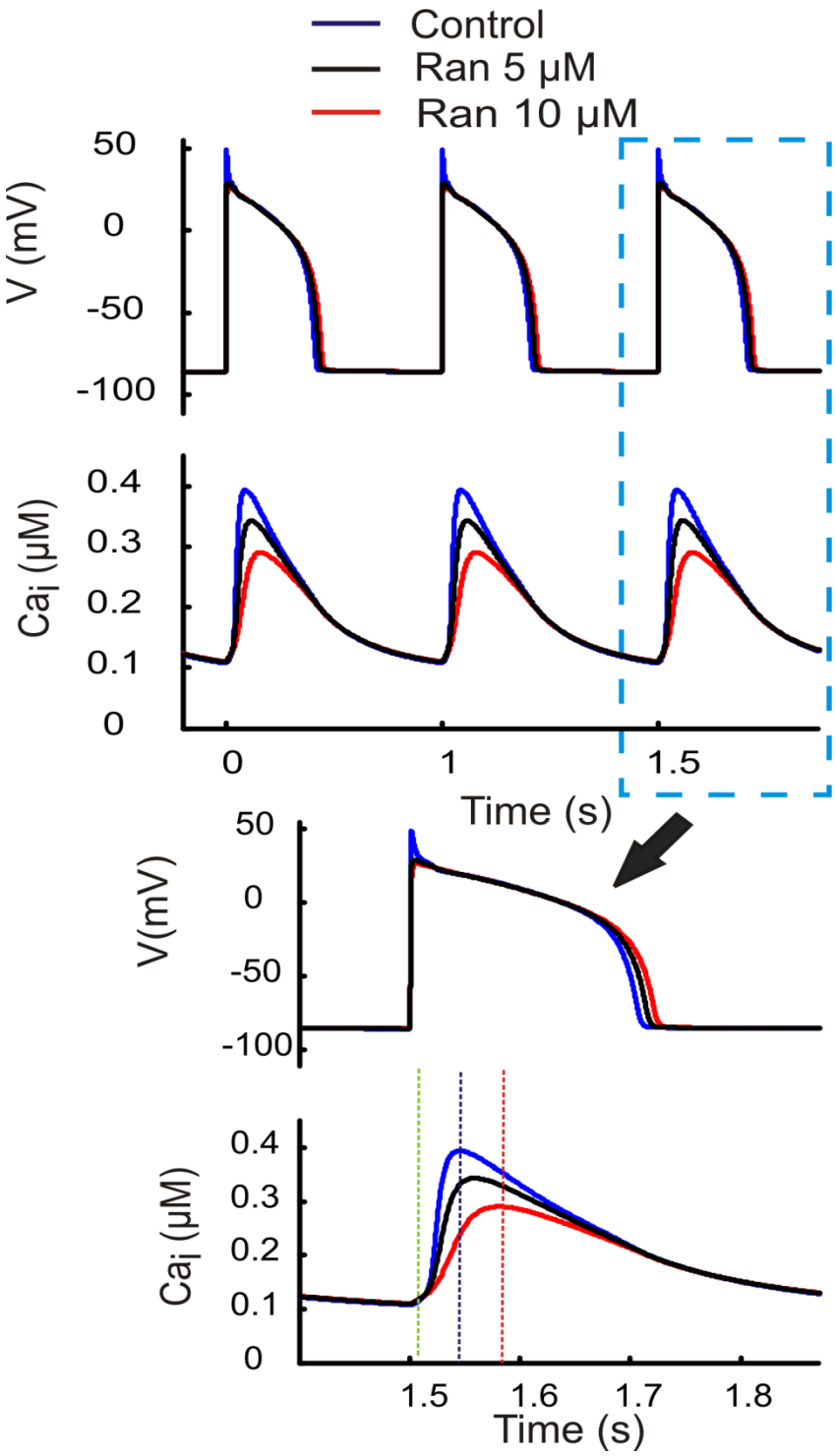

Figure 6: Modeling the effect of ranolazine on APs and Ca_iTs

Top traces: Steady state APs and Ca_iTs at 500 ms CL from the Shannon model at control (blue), 5 μM (black) and 10 μM (red) Ran. Bottom traces: APs and Ca_iTs shown at faster sweep speed.

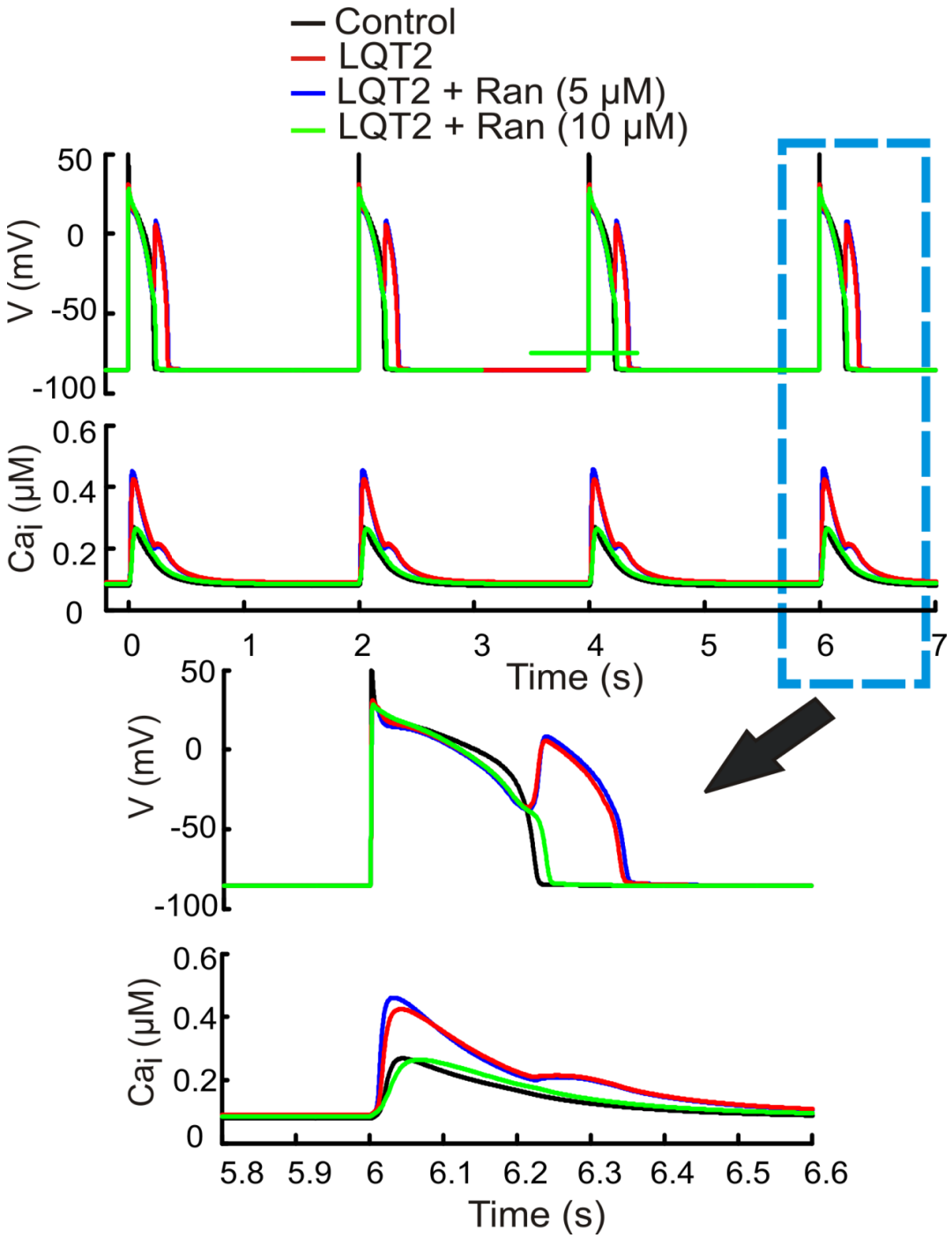

Figure 7: Modeling II - Various [Ran] in LQT2 model

APs and Ca_iTs from the *Shannon* model showing the last four beats from a train of 75 pulses at 2 s CL (black), with LQT2 (red), LQT2 plus 5 μM Ran (blue) and LQT2 with 10 μM Ran (green). EADs persisted with 5 μM but not 10 μM Ran.

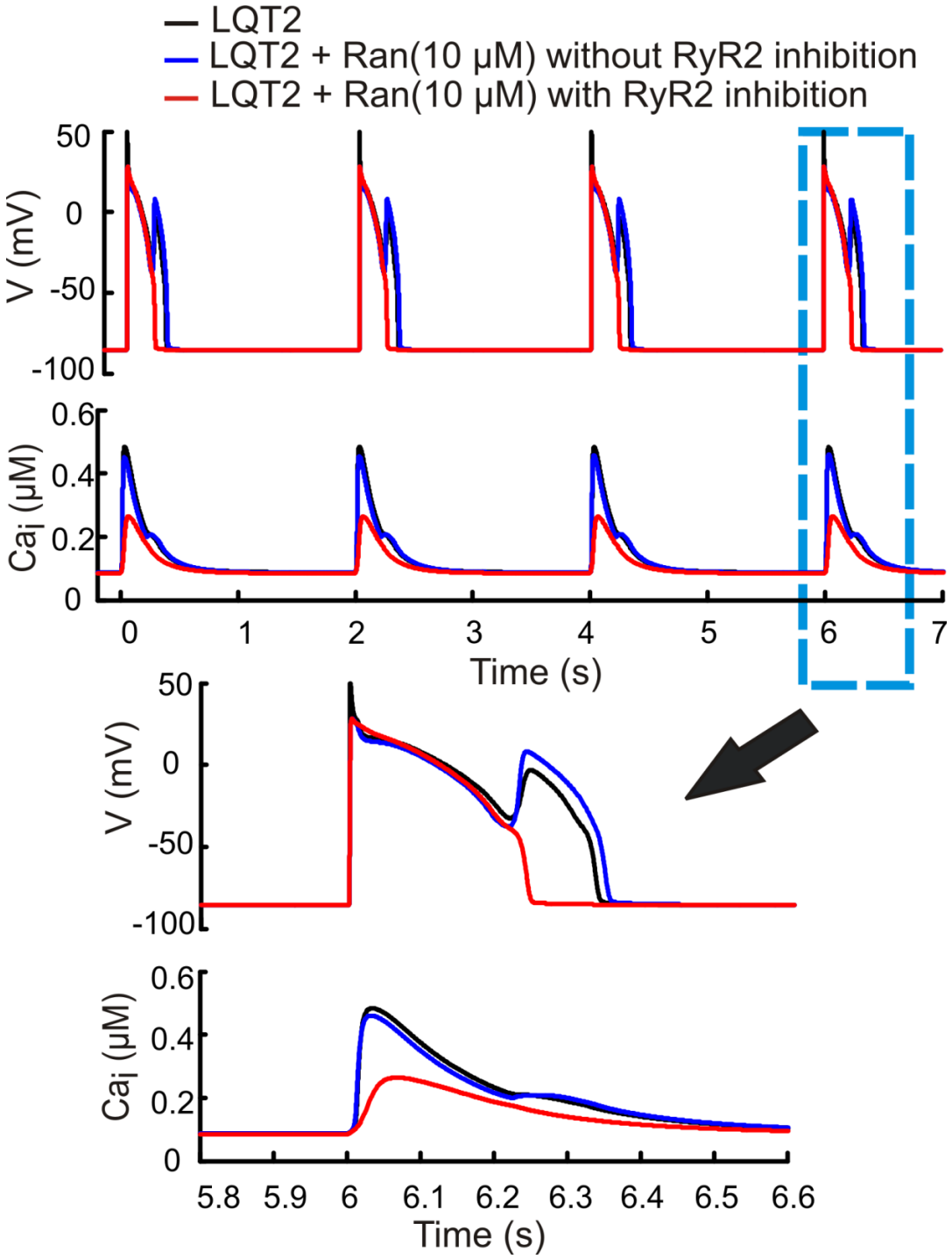

Figure 8: Modeling the antiarrhythmic effect of ranolazine when RyR2 is inhibited

APs and Ca_iTs (Shannon model) showing the last four beats after 75 pulses at 2 s CL with LQT2 (black); with LQT2 and 10 μM Ran but without (blue) and with RyR2 inhibition (red).

2.5 DISCUSSION

The effects of Ran on the normal AP and its suppression of EADs in LQT2 hearts were identified using optical mapping. The main finding was that the *Shannon* model reproduced the experimentally measured AP and Ca_iT at various CLs and the initiation of EADs. However, the model failed to predict the suppression of EADs and TdP after inserting the currently known effects of Ran which contradicted experimental observations. Our experimental data further shows that Ran reduced P_o of RyR2 reconstituted in planar bilayers and desensitized RyR2 to Ca^{2+}-dependent activation. Mathematical simulations that included these changes in the P_o of RyR2 caused by Ran, predicted the suppression of EADs indicating that the antiarrhythmic effects of Ran are dependent on its effect on RyR2. More precisely, the model required a reduction of P_o by 50% (as would be expected by ~10 μM Ran) along with the inhibition of $I_{Na,Late}$ to protect the heart from SR Ca^{2+} overload and to suppress EADs. At 10 μM, Ran acts at multiple targets;[54] by inhibiting I_{Kr}, Ran prolongs APDs and QT intervals, yet paradoxically does not induce but suppresses TdP in experimental LQT1-3 models[45]. Although Ran alone prolonged APDs, when added after E4031, Ran reduced APDs (Figure 2C). Moreover, when hearts were treated with Ran followed by E4031, Ran was considerably more effective at reducing APDs (Figure 2C'). Although the final concentration of the two drugs is the same, the order of their addition produced different results. Electrophysiological studies of *hERG* channels expressed in HEK-293 cells indicated that Ran and E4031 shared the same binding domain to inhibit I_{Kr} but that Ran could not competitively displace E4031.[55] Hence, there are two reasons why the two

conditions differ. a) When E4031 is added first, Ran cannot displace E4031 but E4031 can displace Ran from *hERG*. b) E4031 causes Ca_i overload, oscillation, high plateau Ca_i and spontaneous SR Ca^{2+} release which activates I_{NCX} that prolongs APDs, Ran can the reduce spontaneous SR Ca^{2+} release by stabilizing RyR2 but does not lower plateau Ca_i (Figure 2C) but when added first Ran inhibits the subsequent E4031-induced Ca^{2+} overload (Figure 2C') thereby reducing APD more effectively. In clinical studies, Ran lowered the incidence of arrhythmias in survivors of acute coronary syndrome [56] and studies in patients with atrial fibrillation are promising.[57] Ran has been found to alter Ca^{2+} handling by increasing the latency of Ca^{2+} waves and reducing the severity of SR Ca^{2+} overload in LQT3 induced by ATX-II[58]; an effect that would result in reduced likelihood of Ca^{2+} overload-induced triggered activity.

Mathematical simulation can provide a powerful tool to investigate the mechanisms of drug action, but first it was necessary to select and validate the model based on experimental observation. The *Shannon* model produced APs and Ca_iT, which were close, but not identical, to the optical data; an important difference being the lack of APD prolongation with longer cycle lengths (Figure 3A) which persisted with predictions of APD prolongation caused by Ran. The *Mahajan* model produced unrealistic Ca_iT at slower rates exhibiting a long rise-time to a first peak followed by a gradual rise of Ca_i before recovering to baseline (Figure 3Ab). Also, the peak-Ca_iT collapsed compared at faster rates (Figure 3Bd). In order for the *Mahajan* model to replicate LQT2 conditions, there is a need to formulate a physiologically plausible mechanism for spontaneous SR Ca^{2+} release in Cai-overloaded conditions, which plays a major role in the pathogenesis of delayed afterdepolarizations and triggered activity. Insertion of the effects of Ran in the *Shannon* model of LQT2 failed to predict Ran's antiarrhythmic effect (Figure 4).

There are precedents of drug with established 'modes-of-action' being re-discovered for new properties and/or sites-of-action. For instance, flecainide, a Class IC antiarrhythmic known for its inhibition of $I_{Na,Late,}$ was found to decrease the open-time of RyR2 channels and prevent spontaneous SR Ca^{2+}-release in catecholaminergic polymorphic ventricular tachycardia.[59] Similarly, Ran reduced P_o of RyR2 with an IC_{50} of 10 μM (Figure 5). The Shannon model predicts that RyR2 inhibition by Ran does not alter peak $I_{Ca,L}$ but blunted $I_{Ca,L}$ reactivation through a 27% reduction of I_{NCX} (-1.827 to -1.329 pA/pF) (Figure 9). Hence, Ran inhibition of RyR2 primarily reduced I_{NCX} thereby suppressing EADs (as in Figure 8). Moreover, lower [Ran] (5 μM) did not subdue EADs (Figure 7) in agreement with previous findings.[41] [Ran] subdues arrhythmias at ≥ 10μM but not when [Ran] falls below the concentration required for RyR2 inhibition. In support of this hypothesis, the MERLIN-TIMI 36 trial documented Ran's antiarrhythmic efficacy at 10 μM but not at lower concentrations.[56]

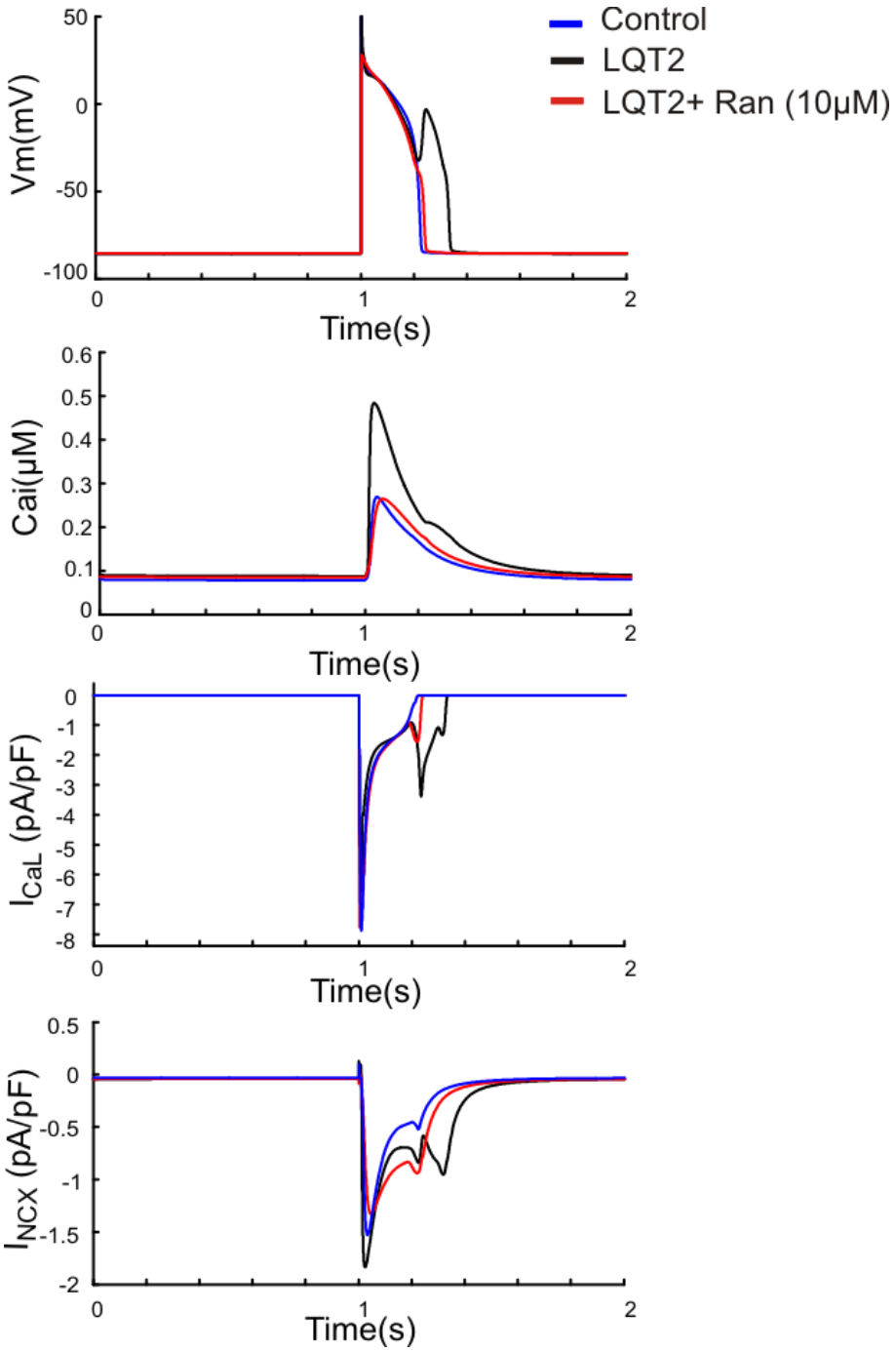

Figure 9: Effect of RyR2 inhibition by ranolazine on AP, Ca_iT, $I_{Ca,L}$ and I_{NCX}

Steady state AP, Ca_iT, $I_{Ca,L}$ and I_{NCX} from the Shannon model showing the last beat following a train of 75 pulses at 2 s cycle length with Control (blue); LQT2 (black) and LQT2 plus 10 μM Ran with RyR2 inhibition (red).

2.6 LIMITATIONS

The *Shannon* model is based on ionic currents measured from rabbit and guinea pig (I_{Ks}) myocytes[60] and the modulation of ionic currents by Ran was measured using guinea pig myocytes.[42, 54] However, species-differences appear to be negligible because Ran has been shown to have similar antiarrhythmic properties in guinea pigs[54], dogs[41] and rabbits[61].

2.7 CONCLUSION

In summary, our study applied computational techniques to discern discrepancies in the pharmaceutical actions of Ran which encouraged us to pursue alternative explanations. It allowed us to experimentally identify a new target and to confirm its validity. The findings show that in LQT2, Ran prevents excessive Ca^{2+} load by stabilizing RyR2 and desensitizing RyR2's activation by Ca_i, resulting in the suppression of EADs and TdP.

3.0 DAURICINE SUPPRESSES EADS IN LONG QT TYPE 2 BY SLOWING DOWN THE KINETICS OF L-TYPE Ca^{2+} CHANNEL

3.1 SPECIFIC AIMS

Dauricine, a bisbenzyl tetrahydrosioquinoline alkaloid derivative, has been shown to produce a variety of pharmacological actions, such as anti-inflammatory,[62] anti-anaphylaxis, and antioxidant and has been widely used for the treatment of various pathologies in China for centuries.[63] It has also been shown to affect various ionic currents in electrophysiological studies. In single isolated cells from guinea pigs, dauricine inhibited the late sodium current, $I_{Na,Late}$,[64] the delayed potassium rectifier current, I_{Kr},[65] and the L-type Ca^{2+} current, $I_{Ca,L}$.[65]

Aim 1: To test the hypothesis that dauricine suppresses arrhythmias in a model of drug-induced LQT2 in a whole heart langendorff preparation using optical mapping

A therapeutic concentration of dauricine was tested in control rabbit hearts to study its effect on APD, Ca_iT and conduction velocity (CV) as a function of cycle length. Dauricine was also tested for its antiarrhythmic properties to suppress EADs in a drug-induced LQT2 in whole langendorff rabbit hearts and assess its effect of predictors of TdP such as dispersion of repolarization (DOR) and incidence of EADs.

Aim 2: To identify the mechanism by which dauricine suppresses arrhythmias in drug-induced LQT2

Drug-induced LQT2 was modelled in the *Shannon* single cell action potential model. The antiarrhythmic property of dauricine was incorporated by modifying the ionic currents based on their IC_{50} values and changing the $I_{Ca,L}$ window current to assess its effect on arrhythmias. The voltage-dependent $I_{Ca,L}$ activation and inactivation was also altered in a step wise manner to assess its effect on arrhythmogenesis.

3.2 INTRODUCTION

In the past few decades, a major effort has been made to investigate and understand the pharmacological effects and the mechanism of actions of compounds used in traditional Chinese herbal medicines. Dauricine, a bisbenzyl tetrahydrosioquinoline alkaloid derivative (Figure 10) has been shown to produce a variety of pharmacological actions, and to exhibit anti-

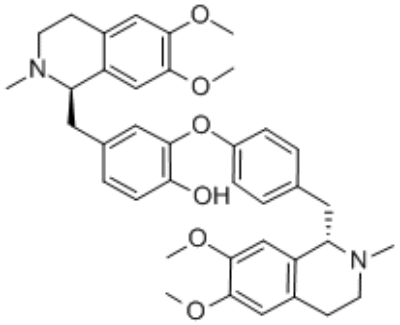

Figure 10: Chemical structure of dauricine

inflammatory,[62] anti-anaphylaxis, and antioxidant effects. Dauricine has been used to treat a wide range of ailments, including inflammation, allergy and arrhythmias.[63] Recently, extensive research has been done to study the effect of dauricine as an antineoplastic agent. Dauricine has been shown to circumvent multidrug resistance cancers[66] and has also been effective in inhibiting human breast cancer angiogenesis, in human breast cancer cell lines (MCF-7).[67]

Dauricine has been shown to act at the L-type Ca^{2+} current, $I_{Ca,L}$ by altering the channel kinetics. $I_{Ca,L}$ plays a fundamental role in the electrophysiology of the heart. $I_{Ca,L}$ sits at a focal point regulating cardiac action potential duration, excitation-contraction coupling, Ca^{2+} homeostasis and in the genesis of EADs leading to TdP.[68] Previous work has shown that reactivation of the $I_{Ca,L}$ during the action potential (AP) plateau plays a major role in EAD formation under LQT conditions.[69] Another hypothesis of EAD formation proposes that APD prolongation promotes cellular Ca^{2+} overload, triggering spontaneous Ca^{2+} release from the sarcoplasmic reticulum (SR),[70] enhancing the turnover rate of I_{NCX},[52] which may reactivate $I_{Ca,L.}$ Both these mechanisms implicate $I_{Ca,L}$ as a trigger of EADs. Most EADs initiate between −40 mV and 0 mV, corresponding to the range of membrane potentials where the steady-state activation and inactivation curves of $I_{Ca,L}$ overlap, often referred to as the 'window current' region.[71] In this 'window', $I_{Ca,L}$ channels which are not inactivated may be available for reactivation which generate the upstroke of the EAD.[72] In dogs with chronic atrioventricular block (cAVB), $I_{Ca,L}$ has a larger 'window' and this increases incidence of EADs under β-adrenergic stimulation.[73] In medicine, $I_{Ca,L}$ is the important therapeutic target in the treatment of hypertension, angina, and cardiac arrhythmias.[74, 75] Theoretical studies have also recently provided an insight into how the shape of $I_{Ca,L}$ influences both excitation-contraction coupling

and repolarization of the cardiac AP, and proposed modification of $I_{Ca,L}$ especially its kinetics as a novel antiarrhythmic strategy.[68, 72]

3.3 MATERIALS AND METHODS

3.3.1 Materials

Dauricine (purity >98%) was a gift from Dr. Fan-Dian Zeng from the laboratory of Department of Pharmacology at the Tongji Medical College, Huazhong University of Science and Technology (Wuhan, China). This agent was dissolved in distilled water and HCL to make a stock solution (25 mM), and it was diluted to the desired final concentrations before the experiment. Dofetilide, a selective I_{Kr} blocker was supplied by Pfizer (NY, USA) and was dissolved in 100 mM sodium hydroxide (250 μg/ml) and was diluted to the final concentration immediately before the experiment.

3.3.2 Isolated perfused hearts

New Zealand White rabbits, (adult females > 60 days old, ~2 kg) were injected with pentobarbital (35 mg kg^{-1}, I.V.) and heparin (200 U kg^{-1}) via an ear vein; the heart was excised and retrogradely perfused through the aorta with Tyrode's solution (in mM): 130 NaCl, 24 $NaHCO_3$, 1.0 $MgCl_2$, 4.0 KCl, 1.2 NaH_2PO_4, 50 dextrose, 1.25 $CaCl_2$, at pH 7.4, gassed with 95% O_2 and 5 % CO_2. Temperature was maintained at 37.0 ± 2 °C and perfusion pressure was adjusted to ~70 mmHg with a peristaltic pump.[46] The atrio-ventricular node was ablated by

cauterization to allow rate control with ventricular pacing (cycle length (CL) 300-1000 ms). The heart was stained with a bolus of a voltage-sensitive dye (PGH1; 50 µl of 1 $mgml^{-1}$ in dimethyl sulfoxide, DMSO) and a Ca^{2+} indicator (Rhod-2/AM, 200 µl of 1 $mgml^{-1}$ in DMSO) delivered through the bubble trap, above the aortic cannula. The hearts were oriented to view the anterior surface, record control APs and Ca_iT. Dofetilide (0.5 µM) and/or Dauricine (5 µM) were directly added to the perfusate.

3.3.3 Optical mapping, data acquisition and analysis

The optical apparatus based on 2 (16x16 pixels) photodiode arrays has been previously described.[46, 47] The anterior surface of the heart was illuminated with a 520 ± 30 nm excitation beam, and the fluorescence was passed through a dichroic mirror (660 nm) to focus the Rhod-2 and PGH 1 fluorescence images on two 16×16 photodiode arrays (C4675–103, Hamamatsu Corp, Hamamatsu City, Japan). Outputs from the arrays were amplified, digitized, and stored in computer memory. Activation and repolarization time points are taken at the maximum first derivative $[(dF/dt)_{max}]$ of the AP upstroke and the maximum second derivative $[(d^2F/dt^2)_{max}]$ of the AP downstroke, respectively. From the activation and repolarization time points recorded in one heartbeat, a computer algorithm generated isochronal maps to visualize activation and repolarization waves.[76] Diodes corresponding to the edges of the heart and/or those detecting pronounced movement artifacts were excluded from the analysis. APDs, Ca_iT were measured at regular intervals. Local conduction velocities vectors were calculated for each diode from the differences in activation time points of that diode (determined from $dF/dt)_{max}$) and its 8 nearest neighbours, as previously described.[77] Measurements of duration are expressed as mean ± SEM; Student's t –Test (unpaired) was applied to determine statistical significance based on $p < 0.05$.

3.3.4 Mathematical modeling

Experimental studies have shown that dauricine inhibits the late sodium current, I_{Na} (IC_{50} = 46 μM),[64] the delayed potassium rectifier current, I_{Kr} (IC_{50} = 14 μM)[65] and the L-type Ca^{2+} current, $I_{Ca,L}$.[65] The effect of dauricine on $I_{Ca,L}$ is complex. In ventricular myocytes, dauricine has been shown to inhibit the peak $I_{Ca,L}$ by 23.2%, 36.3%, and 46.0%, at 1, 3, and 10 μmol/L, respectively.[78] At 10 μM, dauricine shifted the steady state activation curves to the right (by +8 mV) and the inactivation curves to the left (by -10 mV) thereby reducing the 'window' current and prolonging the recovery time from inactivation.[78]

The *Shannon* model [79] was used to study the effect of dauricine based on it's closer fit to experimental data.[80] The whole cell model was compiled in MATLAB and mathematical formulation to study the gating parameters of $I_{Ca,L}$ was compiled in a platform provided by Dr. Jose Luis Puglisi. LQT2 condition was modelled under bradycardia and reduced repolarization reserve by inhibition of I_{Kr} by 50%, elevation of $I_{Ca,L}$ by 32% in addition to decrease in $V_{0.5}Act$ to -24.5 mV as reported earlier.[80] In order to mimic the effect of dauricine (5 μM) on the $I_{Ca,L}$, the $V_{0.5}Act$ and the $V_{0.5}Inact$ potential were shifted by +5 mV (from -24.5 mV to -19.5 mV) and -5 mV (from -35.06 mV to -40.06 mV) respectively, thereby reducing the 'window' current. In order to study the effect of voltage dependent activation/inactivation parameters and reduce the effect of Ca_i-dependent inactivation, the [Ca_i] was fixed at 120 nM and KmCa at 0.6 μM. The steady state parameters of the $I_{Ca,L}$ shown below were modified to assess its effect on antiarrhythmic properties where, d = Voltage-dependent activation gate, f = Voltage-dependent inactivation gate, τd = Time-constant activation gate and τf = Time-constant inactivation gate

$$d_{\infty} = \frac{1}{1 + exp\left(\frac{-(V + V_{0.5}Act)}{6.0}\right)}$$ *Equation 11*

$$\tau d = d_{\infty} \frac{1 - exp(\frac{-(V + V_{0.5}Act)}{6.0})}{0.035(V + V_{0.5}Act)}$$ *Equation 12*

$$f_{\infty} = \frac{1}{1 + exp(\frac{(V + V_{0.5}Inact)}{3.6})} + \frac{0.6}{1 + exp(\frac{(50 - V)}{20})}$$ *Equation 13*

$$\tau f = \frac{1}{(0.0197[exp(-(0.0337((V + V_{0.5}Inact))^2)]) + 0.02}$$ *Equation 14*

3.4 RESULTS

3.4.1 Effect of dauricine on APs and Ca_iT as a function of cycle length

Figure 11A illustrates representative traces of optical APs and Ca_iT from one of the pixels on the photodiode array that measured voltage changes and the corresponding pixel on the photodiode array that measured Ca_i from the same site on the heart (0.9x0.9 mm^2). Figure 11B shows corresponding action potential and calcium transient when the heart was stimulated at a CL of 300 ms and after addition of dauricine (5 µM). Dauricine did not significantly alter APDs and Ca_iT but it had a tendency to prolong them irrespective of the CL. However, it slowed the conduction velocity (CV) significantly ($p < 0.05$) in a rate independent manner.

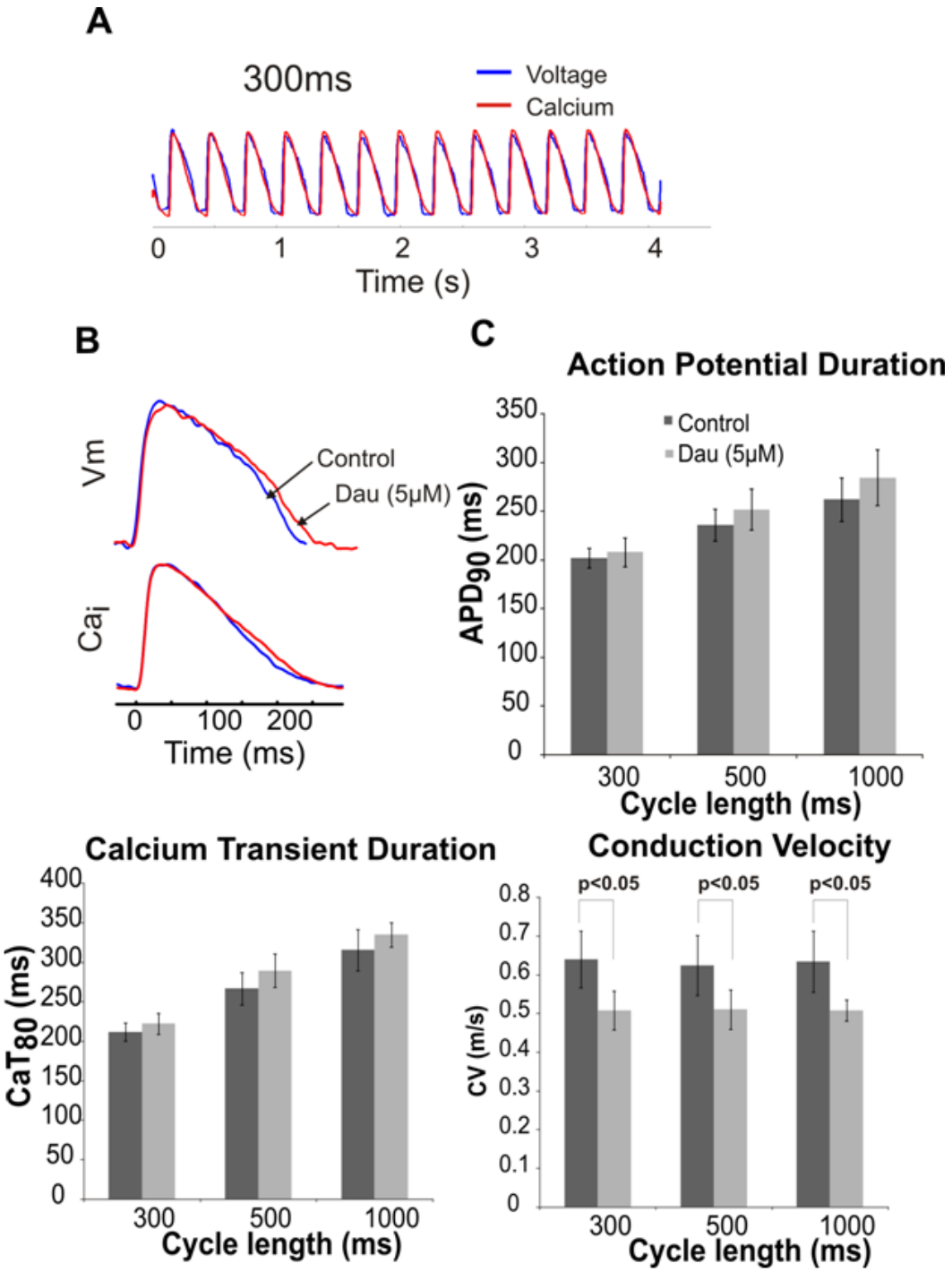

Figure 11: Effect of dauricine in control hearts as a function of rate

(A) Optical mapping traces of action potential (AP) and calcium (Ca_i) transients measured from the same site in the heart paced at 300 ms CL. (B) Comparison between Vm and Ca_iT under control and when treated with dauricine (5 μM). (C) APD_{90}, Ca_iT_{80} and conduction velocity changes in the presence of dauricine (5 μM) at 300, 500 and 1000 ms CL.

3.4.2 Effect of dauricine under drug-induced LQT2

Figure 12A shows a sample AP and Ca_iT trace when the heart was stimulated at a CL of 1000 ms. Dofetilide (0.5 μM) resulted in prolongation of APD from 318 ± 24 ms to 835 ± 32 ms ($p < 0.01$) and Ca_iT from 346 ± 36 ms to 867±48 ms ($p < 0.01$). Prolongation of the APDs was followed by ectopic activity leading to EADs which ultimately developed into TdP (Figure 12B). Addition of dauricine to the perfusate in the presence of dofetilide, reduced the dofetilide induced APD prolongation from 835 ± 32 ms to 542 ± 93 ms ($p < 0.01$) and reversed Ca_iT prolongation from 867 ± 48 ms to 567 ± 103 ms ($p < 0.01$). Dauricine not only reversed prolongation but also suppressed EADs, elicited by dofetilide (n = 5/5 hearts; $p < 0.01$) (Figure 12C). When dauricine was washed out, while the heart was still exposed to dofetilide, in 5 min the prolongation of APD and Ca_iT became more pronounced leading to Ca_i instabilities, EADs and eventually TdP (Figure 12D).

Figure 13 shows a schematic of the heart and the area optically mapped by a 16x16 photodiode array (top panel) and repolarization maps generated using our custom built IDL software.[81, 82] Under control conditions, the repolarization sequence exhibited a standard trend from the apex to the base of the heart. Repolarization started at the apex 240 ms after the first site to activate and the last site repolarized at 366 ms, with the APDs at the base being considerably longer than that at the apex (329 ± 24 ms compared to 304 ± 26 ms). Dofetilide reversed the direction of repolarization pattern from apex to base became base to apex and also increased DOR from 25 ± 6 ms to 55 ± 15 ms ($p < 0.01$ vs Control). The first and last regions to repolarize occurred, respectively, 700 ms and 900 ms after the first site to activate. When dauricine was

added in the presence of dofetilide, it reversed the repolarization pattern back to that measured in the control condition (apex→base) and also reduced the dofetilide-induced dispersion of repolarization from 55 ± 15 ms to 29 ± 15 ms ($p < 0.05$ vs Dofetilide only). Table 3 summarizes the effect of dofetilide and dauricine.

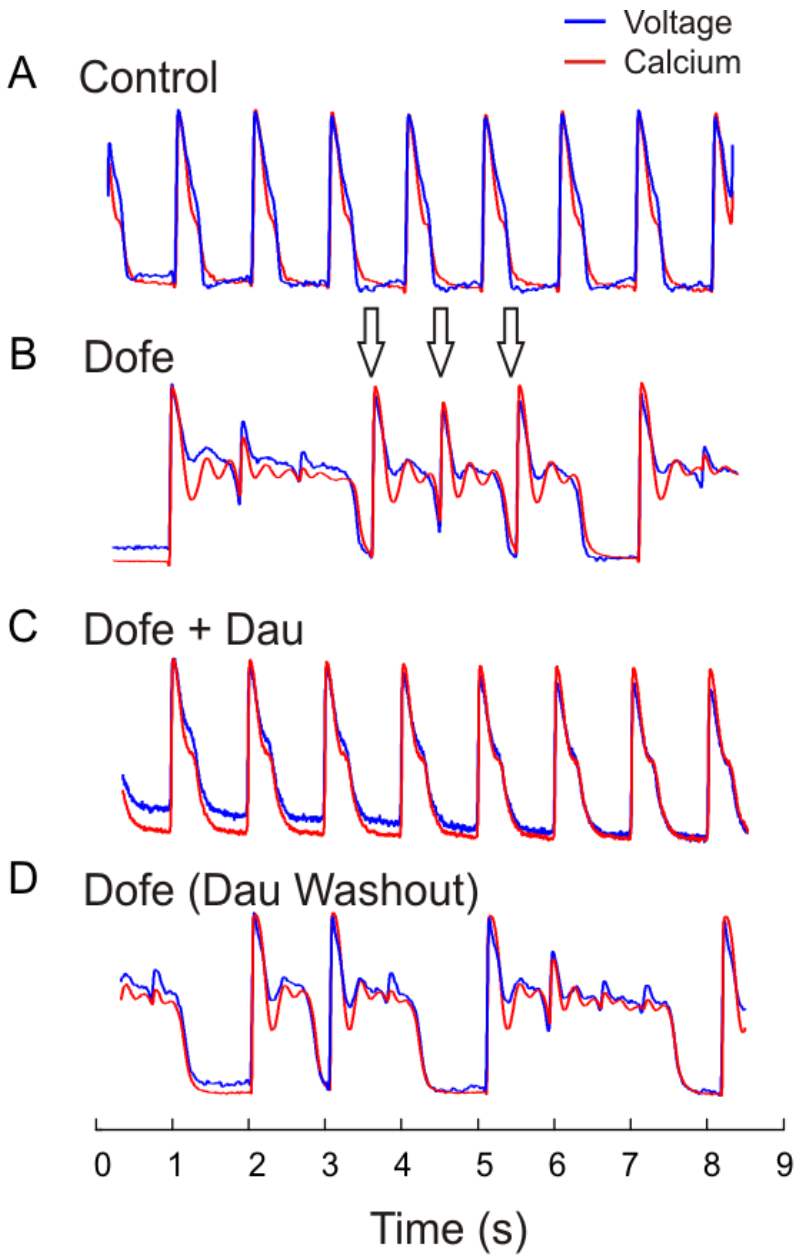

Figure 12: Dauricine suppresses EADs and TdP in drug-induced LQT2

Representative AP and Ca_iT traces under (A) Control at 1000 ms CL; (B) 8 mins after the addition of dofetilide (0.5 µM); (C) 5 mins after the addition of dauricine (5 µM) in the presence of dofetilide (0.5 µM); (D) 7 mins after the washout of dauricine (5 µM).

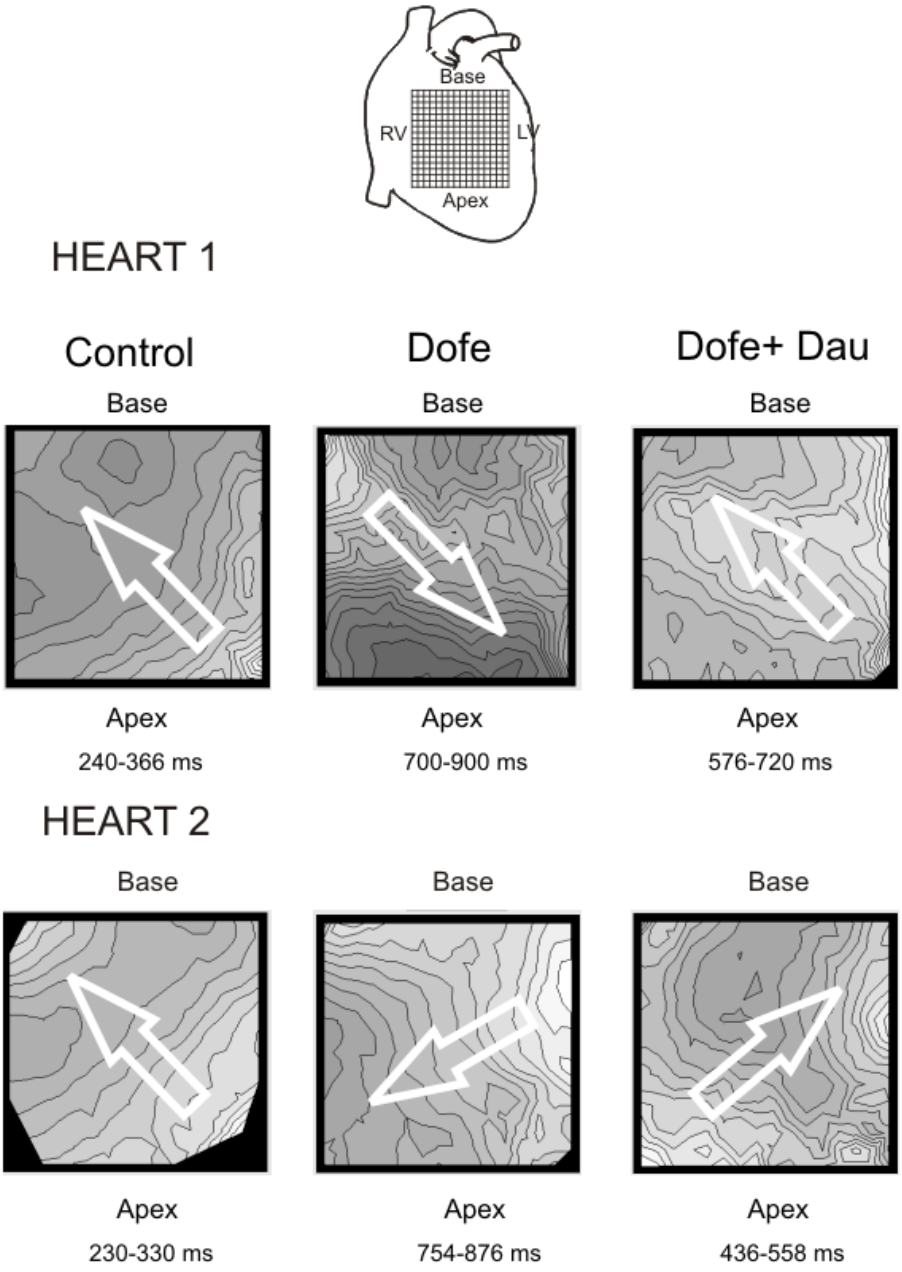

Figure 13: Effects of dofetilide and dauricine on repolarization patterns

A schematic of the heart with the area optically mapped (Top). Under Control, the repolarization sequence exhibited the standard sequence from apex to base (white arrows, left panels). Dofetilide (0.5 μM) reversed the repolarization sequences (white arrows; middle panels) and increase the dispersion of repolarization. Dauricine (5 μM) in the presence of dofetilide reversed the repolarization sequence (white arrows; right panel) and also reduced the dispersion of repolarization.

Table 2: Summary of Parameters - Effect of dofetilide and dauricine

	APD_{90} (ms)	**Ca_iT (ms)**	**DOR (ms)**
Control (n = 5)	318 ± 24	346 ± 36	25 ± 6
Dofetilide (n = 5)	835 ± 32 *	867 ± 48*	55 ± 15*
Dofetilide + Dauricine (n = 5)	542 ± 93 !	567 ± 103 !	29 ± 15 ‡

* versus Control $p < 0.01$; ! versus Dofetilide $p < 0.01$; ‡ versus Dofetilide $p < 0.05$

3.4.3 Modeling: Effect of dauricine under LQT2

LQT2 conditions resulted in Ca^{2+} overload, spontaneous SR Ca^{2+} release and EADs. The APs had single or multiple EADs in each beat (287 EADs in a train of 200 APs). Modeling the effect of dauricine on the $I_{Na,Late}$ and I_{Kr} did not suppress the arrhythmias. Incorporating the effects of dauricine on the $V_{0.5}Act$ and $V_{0.5}Inact$ of $I_{Ca,L}$ resulted in (a) smaller $I_{Ca,L}$ 'window' current (Figure 14A); (b) partially reversed the APD back to control conditions (448 ms to 240 ms compared to 226 ms in Control); (c) reduced Ca^{2+} overload and (d) abolished the EADs (0/287 in 200 beats) (Figure 14B).

3.4.4 Modeling: Half activation/inactivation potential and arrhythmias

Although the overall effect of dauricine on the changes in the activation-inactivation kinetics suppressed EADs, it was still unclear whether changes to either the voltage-dependent activation or inactivation potential would be sufficient to suppress arrhythmias. To elucidate the relative importance of activation and inactivation on the incidence of EADs, the $V_{0.5}Act$ (or $V_{0.5}Inact$) was changed in a stepwise manner by ± 1 mV and then in steps of ± 2.5 mV keeping the other parameter constant.

When the $V_{0.5}Act$ was subjected to a stepwise change, at +1 mV shift from -24.5 mV to -23.5 mV (Eqns 11, 12), the APD shortened from 448 ms to 385 ms and the peak Ca_i amplitude was reduced from 0.75 µM to 0.72 µM. This shift in $V_{0.5}Act$ was not effective at suppressing EADs; there were 172 EADs in 200 beats compared to 287 in 200 beats with normal $V_{0.5}Act$. Stepwise change of +2.5 mV from -24.5 mV to -22 mV shortened the APD further to

252 ms, reduced the peak Ca_i amplitude to 0.42 µM and completely abolished EADs. Additional change of +2.5 mV to -19.5 mV resulted in further shortening of the APD to 241 ms and reduction of peak Ca_i amplitude to 0.40 µM (Figure 15).

When $V_{0.5}Inact$ was subjected to similar stepwise change, a -1 mV shift from -35.06 mV to -36.06 mV (Eqns 13, 14) shortened the APD from 448 ms to 413 ms, reduced peak Ca_i amplitude from 0.75 µM to 0.46 µM but did not completely abolish the EADs (142 EADs in 200 beats compared to 287 in 200 beats). A stepwise change by -2.5 mV to -37.56 mV and -40.06 mV resulted in shortening of APD to 259 ms and 257 ms respectively, reduced peak-Cai amplitude to 0.43 µM and 0.42 µM respectively and completely abolished the EADs (Figure 16).

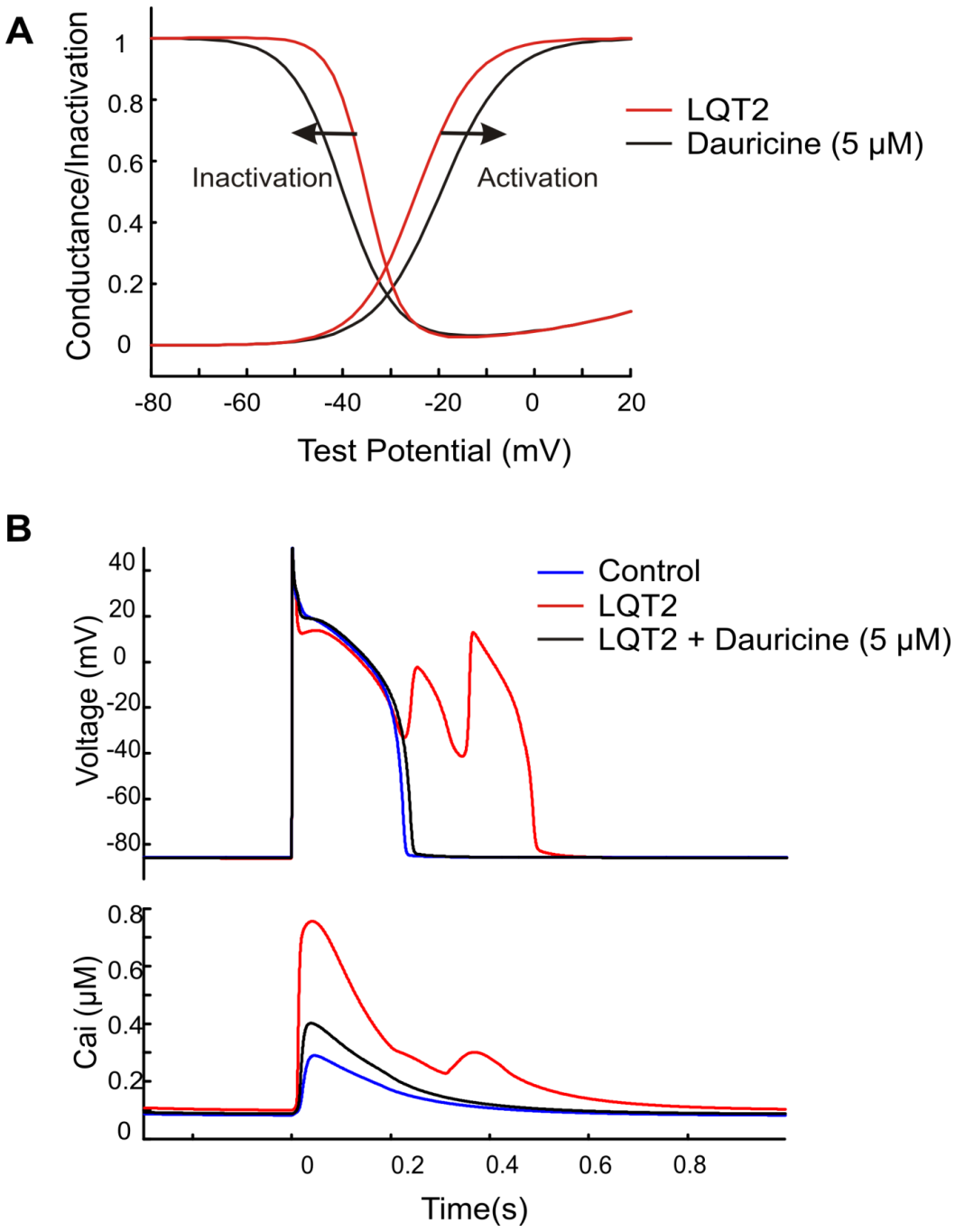

Figure 14: Modeling the antiarrhythmic effects of dauricine under LQT2

(A) Schematic of the steady state activation/inactivation curves under LQT2 and with LQT2 + Dauricine (5 μM). Dauricine shifted the $V_{0.5}Act$ to the right and $V_{0.5}Inact$ to the left and reduces the $I_{Ca,L}$ 'window' current. (B) Shows AP and Ca_iT from the *Shannon* whole cell rabbit ventricular myocyte model under control, LQT2 and LQT2 + dauricine (5 μM). Only the effects of dauricine on the $V_{0.5}Act$ and $V_{0.5}Inact$ were incorporated into the model (Eqns 11-14). Dauricine completely abolished the EADs and reversed back the AP prolongation in agreement with the experimental results.

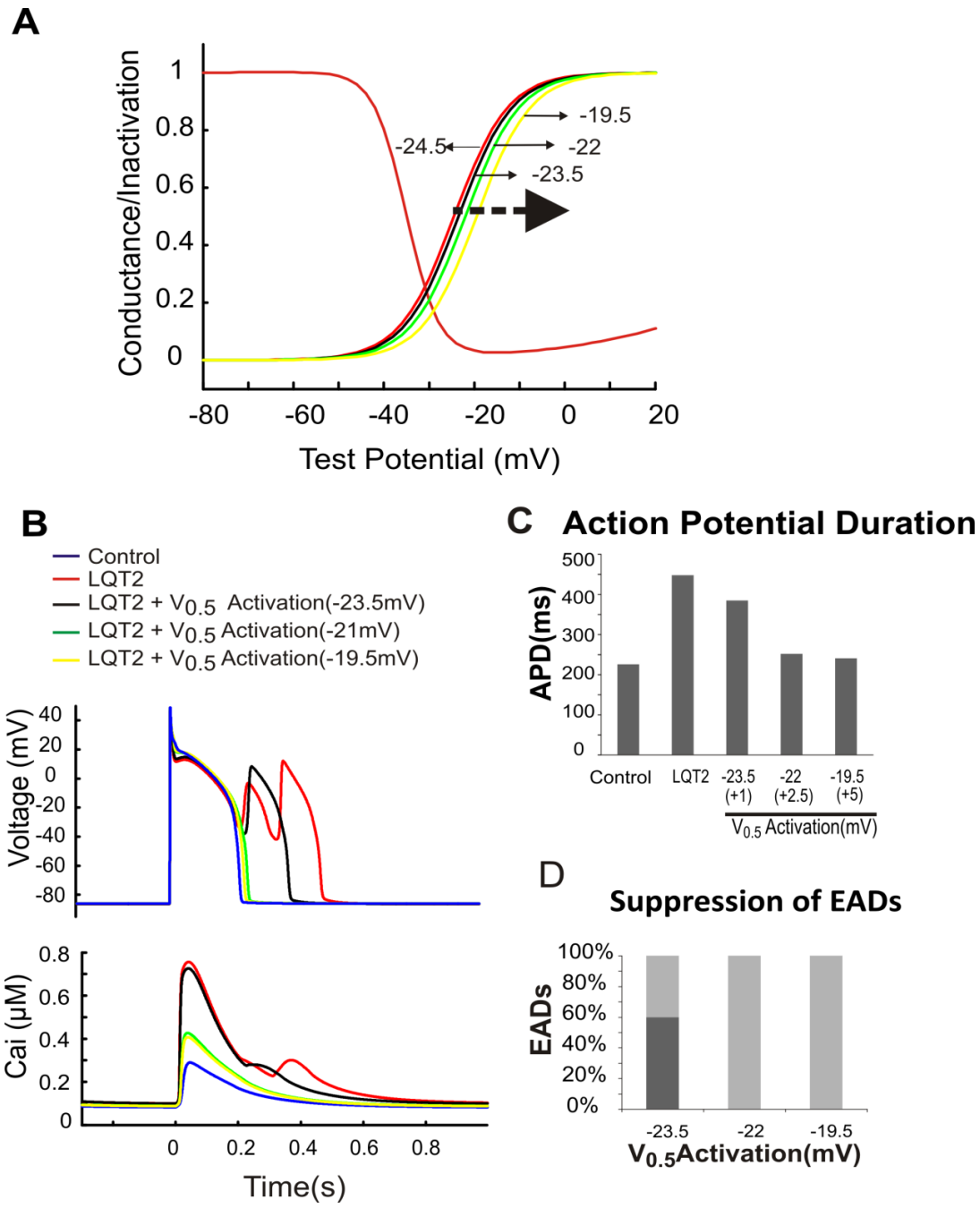

Figure 15: Modeling the effect of *$V_{0.5}Act$* on arrhythmias

(A) Steady state activation/inactivation curves when *$V_{0.5}Act$* was shifted to the right in steps of +1 mV and +2.5 mV while keeping *$V_{0.5}Inact$* constant, resulted in the reduction of the 'window current' (B) Sample action potential and Ca_iT traces incorporating the changes in *$V_{0.5}Act$* in the whole cell model. A +2.5 mV shift effectively suppressed arrhythmias and reduced the Ca^{2+} overload. (C) Action potential duration (APD) as a function of the *$V_{0.5}Act$*. (D) Suppression of EADs as a function of the *$V_{0.5}Act$*.

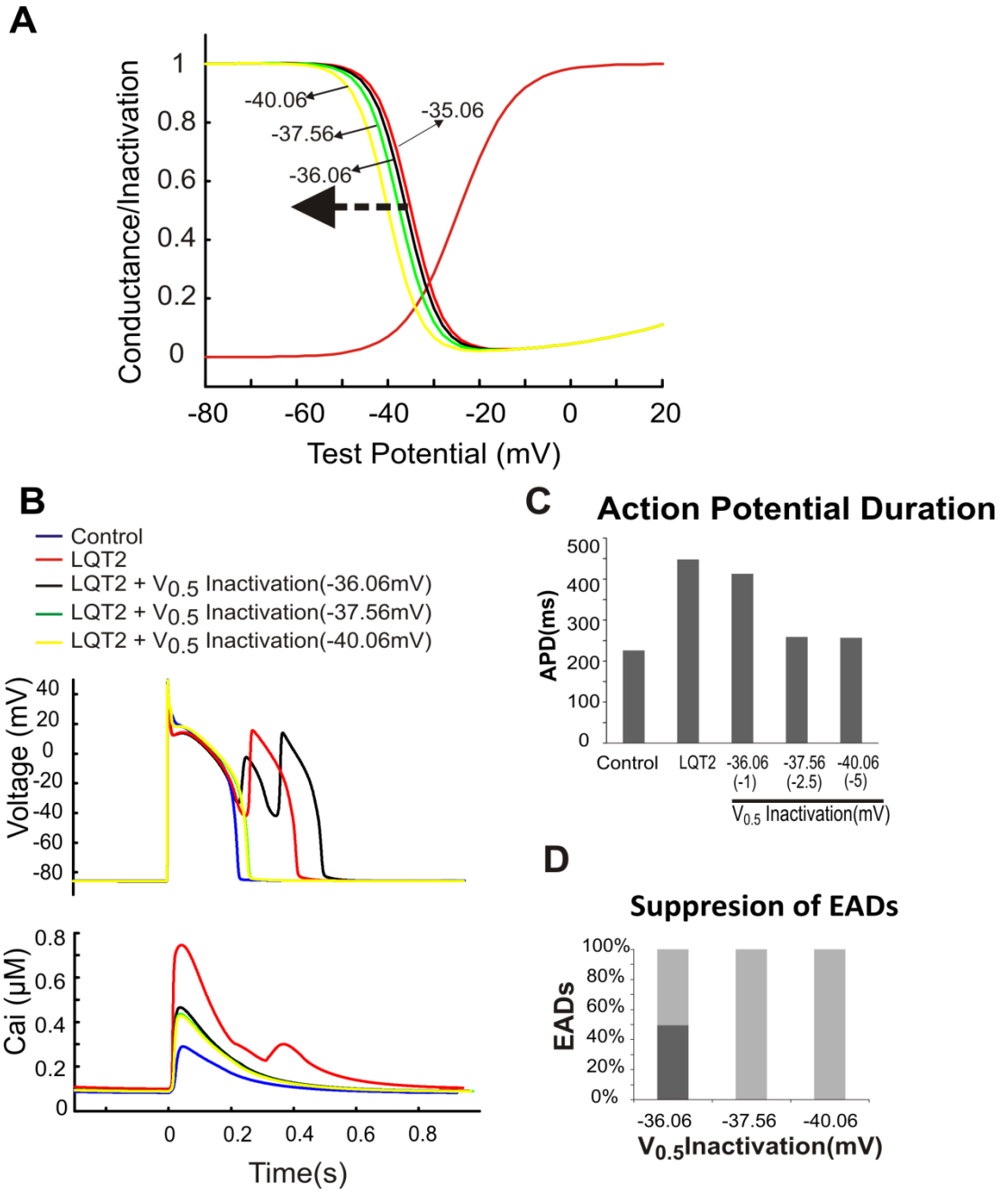

Figure 16: Modeling the effect of $V_{0.5}Inact$ on arrhythmias

(A) Steady state activation/inactivation curves when $V_{0.5}Inact$ was shifted to the left in steps of -1 mV and -2.5 mV while keeping $V_{0.5}Act$ constant, resulted in the reduction of the 'window current' (B) Sample AP and Ca_iT traces with the changes in $V_{0.5}Inact$ in the whole cell model. A -2.5 mV shift effectively suppressed arrhythmias and reduced the Ca^{2+} overload. (C) Action potential duration (APD) as a function of the $V_{0.5}Inact$. (D) Suppression of EADs as a function of the $V_{0.5}Inact$.

3.5 DISCUSSION

The main results are that in control hearts, dauricine (5 μM) slowed CV in a rate independent manner. In drug-induced LQT2, dauricine suppressed EADs and TdP in the presence of an I_{Kr} blocker (dofetilide). Mathematical modeling confirmed that dauricine suppressed the EADs and reversed the AP prolongation primarily by slowing down the kinetics of $I_{Ca,L}$, specifically by decreasing the $V_{0.5}Act$, increasing the $V_{0.5}Inact$ and thereby decreasing the 'window' current. Simulation also revealed that a minor change of ± 2.5 mV in either of the $V_{0.5}Act$ or $V_{0.5}Inact$ is sufficient enough to abolish EADs.

Dauricine has been demonstrated to be a promising anti-angiogenic drug for the treatment of human breast cancer mainly via the suppression of HIF-1α and by blocking the PI-3K/Akt/mTOR signaling pathways.[67] It has also been shown effective in suppressing colon cancer mainly via the down regulation of NF-κB-mediated gene expressions including genes involved with anti-apoptosis and angiogenesis.[83] In recent years with the success of dauricine in suppressing tumours and with the promise of entering clinical trials as a treatment for cancer, tremendous amount of work has been done to assess its effects on the heart.

In our study, dauricine had a tendency to prolong APD and Ca_iT under control conditions at different CL. This can be attributed to the tendency of dauricine to inhibit I_{Kr} and I_{Ks} currents in a rate independent manner.[63, 84] On the other hand, dauricine significantly reversed dofetilide-induced APD and Ca_iT prolongation. Dispersion of repolarization (DOR) has been implicated as an important risk factor in the initiation and maintenance of arrhythmia in the LQTS.[85] Our study

showed that the effect of dofetilide was greater at the apex than the base due to the gradient of I_{Kr} resulting in a reversal of the direction of repolarization and a marked increase in DOR. However, the presence of dauricine with dofetilide reversed this direction of repolarization back to control and also reduced the DOR. Simulations with the effects of dauricine (5 μM) on $V_{0.5}Act$ or $V_{0.5}Inact$ under LQT2 completely suppressed EADs. A ± 1 mV shift in either the $V_{0.5}Act$ or $V_{0.5}Inact$ resulted in suppression of EADs with an efficiency of 40% and 50% respectively. Changes by ± 2.5 mV in either of the parameters resulted in a complete suppression of EADs. Our studies demonstrate the antiarrhythmic properties of dauricine in LQT2 syndrome in whole hearts and simulations. Similar actions of the drug could be responsible for antiarrhythmic properties and efficacy in pathology such as or Timothy syndrome, also known as LQT8 or syndactyly-associated LQTS. Timothy syndrome is associated with missense mutations in the $Ca_v1.2$ gene that lead to a marked loss of voltage-dependent inactivation resulting in a gain of function of $I_{Ca,L}$.[86] Increased activity of L-type Ca^{2+} channels may lead to Ca^{2+} overload in the cell, which has been shown to contribute to the development of EADs and TdP.[87, 88]

The L-type Ca^{2+} channel in the heart ($Ca_v1.2$) is composed of four subunits, including α1, α2δ, β and γ. The α1-subunit forms the pore of the channel. The co-expression of α2δ increases the membrane trafficking along with an increase in current amplitude, faster activation and inactivation kinetics, and a hyperpolarizing shift in the voltage dependence of activation.[89] The β-subunit aids in trafficking of the α1-subunit to the membrane and the α1-β interaction is known to modulate the biophysical properties of the channel such as current density and the properties of activation and inactivation.[75, 89] The γ predominantly modulates the biophysical properties of the channel.[89] Each of the three major types of selective Ca^{2+} channel blockers (benzothiazapine (diltiazem), phenylalkylamine (verapamil) and dihydropyridines (nifedipine)) interacts with a

specific receptor domain located on the α1-subunit that constitutes a substantial portion of the *$Ca_v1.2$* and can modulate other receptor sites.[75, 90]

Based on previous computational and experimental work, researchers have tried to modulate the subunits and studied its effect on arrhythmogenesis and cardiac wave stability.[91] Their results indicate that the recovery kinetics of the $I_{Ca,L}$ current were relatively insensitive to β-subunits but changed dramatically when β-subunits were eliminated and along with the reduction in the amplitude of $I_{Ca,L}$ flattened the restitution.[91] In another study, mutant Ca-insensitive calmodulin CaM_{1234} were over expressed in isolated rabbit ventricular myocytes to alter $I_{Ca,L}$ inactivation kinetics and increase dynamic wave stability, by flattening APD restitution slope and preventing APD and Ca_iT alternans, without decreasing contractility.[68] Although, these studies provide theoretical strategies and genetic modification to suppress arrhythmias, no one has reported on a known natural or formulated therapeutics that modulates the kinetics of the $I_{Ca,L}$ and suppresses arrhythmias.

3.6 LIMITATIONS

Blocking $I_{Ca,L}$, by reducing the channel conductance is a potent means of suppressing arrhythmias, but unfortunately the dose of Ca^{2+} channel blocker required to achieve this effect suppresses contractility. Dauricine at therapeutic doses (5-10 μM) reduces the $I_{Ca,L}$ 'window' current and the influx of Ca^{2+} with each beat, thereby suppressing contractility. No direct measurements have been made in the study to assess contractility changes. In the late 80's, dauricine (~180 mg) was clinically evaluated in treating cases of arrhythmias in humans with an efficiency of 91.3% and the contractility changes seem to be tolerated.[92] Cases of QT

prolongation and complete left bundle branch block have also been reported with regard to a treatment with dauricine but at a higher dose of 900 mg/day.[93]

Another potential drawback of the study is the lack of information regarding the binding site of dauricine to $I_{Ca,L}$. Although, most of the Ca^{2+} blockers bind to α1-subunit and induce a decrease in conductance of $I_{Ca,L}$, the effect of dauricine is more intricate. Dauricine has also been shown to shift the inactivation curve to the right and markedly delayed the half-recovery time of $I_{Ca,L}$ from inactivation.[78] Further studies are needed to assess dauricine's binding site, whether or not it modulates the interaction between the subunits, and to relate its structure-function relationship to its antiarrhythmic effects. Based on binding site information, a relatively large number of derivatives of dauricine can be designed to bind and modulate channel kinetics my by analogy with studies based on the family of dihydropyridine derivatives.[90, 94]

3.7 CONCLUSION

The findings from our experimental and simulation studies provide evidence of dauricine's antiarrhythmic property based on channel kinetic modification which represents a novel strategy to suppress arrhythmias. In summary, our findings support the existing theoretical studies, provide novel insight on the mode of action of dauricine's antiarrhythmic properties, how minor changes in half-activation ($V_{0.5}Act$) and half-inactivation potential ($V_{0.5}Inact$) of L-type Ca^{2+} channel can effectively suppress EADs and a foundation for further studies to design analogues of dauricine that can suppress arrhythmias without affecting contractility.

4.0 RELAXIN MITIGATES INDUCED ATRIAL FIBRILLATION (AF) IN SPONTANEOUSLY HYPERTENSIVE RATS (SHR) BY REVERSAL OF FIBROSIS

4.1 SPECIFIC AIMS

Atrial fibrillation (AF) is the most common form of cardiac arrhythmia and contributes significantly to cardiac morbidity and mortality. AF has been associated with fibrosis, aging, and hypertension. Pharmacological therapy targeted at the underlying fibrotic substrate has claimed to be a new frontier in the management of AF.

Aim 1: To test the hypothesis that atrial fibrosis is a key factor in the genesis of induced AF in spontaneously hypertensive rats (SHR)

The mechanisms of AF were elucidated using SHR hearts as models of hypertension, fibrosis and AF. SHR and normotensive Wistar Kyoto (WKY) were tested for inducible AF with programmed stimulation applied to the right atrium (RA) and optically mapped for APs and CaiT. The nature of AF was determined through measurements of dispersion of repolarization (DOR), Ca_i instabilities, changes in restitution kinetics (RKs: AP durations, CV and rise times of Cai and AP upstrokes). Immuno-histological analysis of atrial tissues correlated fibrosis, connexin (40/43) levels and AF induction between SHR and WKY.

Aim 2: To test the hypothesis that exogenous relaxin (RLX) treatment mitigates AF inducibility

The mechanisms whereby RLX treatment mitigates AF inducibility was elucidated using SHR. SHR rats were treated with RLX or vehicle for 2 weeks and the hearts were tested for inducible AF with programmed stimulation applied to the right atrium (RA). Changes in restitution kinetics were compared between the RLX-treated and vehicle-treated groups (RKs: AP durations, CV and rise times of Ca_i and AP upstrokes). Histological analysis of atrial tissues correlated fibrosis levels, connexin (40/43) levels/phosphorylation and localization and AF induction between untreated, RLX-treated and vehicle-treated SHR.

4.2 INTRODUCTION

Atrial Fibrillation (AF), the most commonly encountered arrhythmia, affects about 2.3 million people in the United States and is a leading cause of stroke and heart failure. [95] The cost of AF and its associated complications equaled $12 billion in 2006. [96]

Among the many risk factors that have been proposed for the development of AF, the most important risk factors are sex (males compared to females), old age (age >60 years), and hypertension.[95] Hypertension leads to both electrical and structural remodeling of the atria. Electrical remodeling shortens atrial refractoriness by reducing the APD. [97, 98] Atrial tachypacing (≥300 beats/min) causes remodeling as demonstrated in dogs, sheep and pigs and has been associated with rate-induced Ca^{2+} overload, transcriptional down regulation of L-type Ca^{2+} channels, shortening of APD, and spontaneous opening of acetylcholine-regulated K^+ channels.[99] Chronic AF (CAF) leads to further remodeling including; increased expression of protein kinase C (PKC) and PKC-dependent protein phosphorylation, Ca^{2+}-calmodulin dependent kinase II (CaMKII) activation, phosphorylation of ryanodine receptors (RyR2), greater spark activity,

spontaneous Ca^{2+} release from the sarcoplasmic reticulum and a greater incidence of early and delayed afterdepolarization.[100] Thus, changes in Ca^{2+} handling contribute to the severity of AF in patients with chronic [101-103] and paroxysmal AF.[104] Long-term rate-dependent remodeling may lead to decrease in CV due to down regulation of *Nav1.5* and I_{Na},[105, 106] and to a reduction and lateralization of gap junctions, mainly connexin 43 even though connexin 40 is also abundant in the atria of some speices.[107]

Connexin act as a low resistance intercellular pathway for impulse propagation by regulating the flow of ions between adjacent cardiac myocytes.[108] The cardiac myocytes are mostly connected via gap junctions located at the narrow ends of the rectangular myocytes. Connexin emerges as a molecule that is involved not only in forming gap junctions for the cell–cell transfer of electrical charge but also as an organization center for the establishment of proper sodium channel function.[109] Fibrosis is the hallmark of arrhythmogenic structural remodeling.[110] Fibrosis can be due to cell death when these cells are replaced by collagen, called reparative fibrosis, or to aging without cell loss or increases in mechanical load, which is called reactive fibrosis.[111, 112] It results in alterations in the connexin expression[113] and creates a barrier to impulse propagation by disrupting inter-myocyte coupling.[110,114] Structural remodeling also results in electrical tissue non-homogeneity, slowed conduction and electrical uncoupling, facilitating AF continuation without inducing changes in atrial action potential properties.[115]

Increased collagen deposition has been well documented in AF patients compared with control subjects in sinus rhythm.[116] The precise signaling processes responsible for the development of fibrosis are unknown. However, multiple factors such as angiotensin converting enzyme (ACE), Transforming Growth Factor β (TGF-β1) and Platelet Derived Growth Factor (PDGF) have been implicated in the pathogenesis of atrial fibrosis. Studies on ACE

overexpression in mice revealed that increased ACE is associated with atrial enlargement, atrial fibrosis, and AF.[117] Conversely, blockade of ACE or angiotensin-receptor blunts atrial fibrosis and AF in animal models and patients with HF.[118] Transforming Growth Factor β (TGF-β1) and Platelet Derived Growth Factor (PDGF) are thought to act on cardiac fibroblasts to increase collagen production without offsetting increases in collagen degradation.[110] Similar to studies with overexpression of ACE, animal studies with overexpression of TGF-β1, have shown that TGF-β1 is associated with increased levels of atrial fibrosis and susceptibility to AF.[119] Studies with injection of PDGF-α in mice have shown that increased levels of PDGF-α are associated with atrial fibrosis and AF in normal hearts. [120]

The current treatment and management options for AF include radiofrequency ablation, antiarrhythmic drugs, and anticoagulation therapy. Even though radiofrequency ablation has been shown to be more effective than antiarrhythmic drugs for treatment of paroxysmal AF, the complications, costs, and difficulties (i.e. recurrence of AF) serve as the driving force for the development of better and safer therapies for the treatment of AF.[121, 122] Existing antiarrhythmic drug approaches have limited effectiveness and are associated with risks of serious complications, particularly ventricular pro-arrhythmia and/or organ toxicity.[123] Accordingly, attenuation and reversal of structural remodeling have increasingly become the focus of attempts at therapeutic innovation, and is of particular clinical interest because it is often not possible to begin treatment in humans before a significant degree of atrial remodeling has already occurred and is irreversible.

Relaxin (RLX), a peptide hormone, is thought to have a wide range of biological actions including anti-inflammatory, anti-apoptotic, cardioprotective, vasodilatory, pro-angiogenic effects, and anti-fibrotic effects.[124] RLX was first identified for its role in reproduction and

pregnancy. It is thought to play a critical role in the hemodynamic adaptive and anti-fibrotic changes that occur during pregnancy.[125] Our hypothesis is that RLX's anti-fibrotic properties may be effective in the suppression of fibrosis AF. Male RLX gene-deficient mice developed age-related cardiac fibrosis, ventricular stiffening, and diastolic dysfunction, suggesting its role as an important intrinsic regulator of collagen turnover.[126] Studies on RLX treated spontaneously hypertensive rats (SHR) have shown its effectiveness in reversing fibrosis in the ventricles. However, the study did not see a difference in atrial fibrosis between RLX treated SHR and saline treated SHR.[127] Therefore, RLX's potential application in the reversal of atrial fibrosis and suppression of AF is not known.

There is no such thing as a 'perfect' animal model of AF, any more than there is a single clinical mechanism of AF. Any animal model reproduces at best a very limited component of the pathophysiologic spectrum of clinical AF.[128] The most widely studied model for the effects of hypertension on the cardiovascular system is the SHR.[129] In SHR, hypertension progresses as a function of age, is more pronounced in males than females, and exhibits most of the hallmarks of the human disease.[130] Previous studies on the SHR model have shown an increased incidence of AF and atrial tachyarrhythmias compared to normotensive Wistar-Kyoto (WKY), attributed to greater fibrosis levels.[131] These findings indicate that fibrosis is a key factor promoting the development of AF making it an important antiarrhythmic target.

4.3 METHODS

4.3.1 Study design

Age (9-12 months) and sex (male) matched rats were divided into four groups WKY, SHR, SHR treated with vehicle (SHR+VEH) and SHR treated with relaxin (SHR+RLX) to test for AF inducibility. Subcutaneous osmotic minipumps (Ducruet Corporation, model 2ML2) were primed and loaded with either recombinant human RLX solution (release rate: 0.4 (mg/kg)/day) or VEH (20 mmol/L sodium acetate buffer, pH 5.0). RLX was obtained from Corthera Inc. This dose of RLX was modified to accommodate the reservoir volume of the mini-pumps and is slightly lower than the 0.5 (mg/kg)/day that have been used previously to treat *in vivo* rodent models of fibrosis.[127, 132-134] Pumps were surgically implanted under sterile technique into the subcutaneous space on the left side of anesthetized animals. Animals were monitored over the 14-days of RLX or VEH delivery to ensure proper healing of the implant pocket.

4.3.2 Blood pressure, heart rate and serum relaxin concentration

Blood pressure (BP) was measured by a noninvasive tail cuff method using Coda 6 (Kent Scientific Corp., Torrington, CT), which measured heart rate (HR) and systolic and diastolic pressures.[135] Signals were recorded and analyzed using Kent Scientific software. The BP and the HR were measured at three different time points during the 14-day treatment period with either RLX or vehicle; pre-treatment, mid-treatment (6-9th day of a 14-day treatment) and post-treatment (14th day). Blood samples were taken immediately after the hearts were excised to measure RLX serum concentration. Quantikine Human Relaxin-2 Immunoassay (DRL200, R&D

Systems Inc., Minneapolis, MN, USA) was used according to the manufacturer's protocol to determine the serum RLX concentration of the samples.

4.3.3 Optical apparatus and analysis

Hearts were excised from animals of either strain and treatment protocol after being anesthetized with pentobarbital (50 mg/kg) and injected with heparin (200 U/kg IV). Coronary arteries were perfused via the aorta in a Langendorff perfusion system with physiological Tyrode solution containing (mM): 122 NaCl, 25 $NaHCO_3$, 4.81 KCl, 2 $CaCl_2$, 2.75 $MgSO_4$, 5 Glucose (pH 7.4) gassed with 95 percent O_2 and 5 percent CO_2 at 37.0±0.2 degrees Celsius.

Hearts were placed in a chamber and initially perfused with 30 µL blebbistatin to arrest contractions and reduced motion artifacts. The hearts were stained with bolus injections of a voltage-sensitive dye (PGH-1; 300 µL of 1mg-ml^{-1} in dimethyl sulfoxide, DMSO) and Ca^{2+} indicator (Rhod-2/AM, 300 µL of 1mg-ml^{-1} in DMSO) or only the voltage-sensitive dye (di-4-ANEPPS 10 µL of 2 mmol/L in DMSO) to optically map action potentials with the anterior surface of the heart.

Light from two 100-W tungsten-halogen lamps was collimated, passed through 520 ± 30 nm interference filters, and illuminated the heart from two sides for uniform illumination. Fluorescence emitted from the stained heart was collected with two camera lenses (50 mm f/1.2 mm Nikon and 50 mm f/0.95 Navitar) on two 100 x 100 pixel CMOS cameras (Ultima, Scimedia, Ltd. Tokyo, Japan) scanned at 2,000 frames per second. Pixel resolution was 150 x 150 µm^2, and the data was recorded and stored in intervals of 4-8 seconds.

The activation and repolarization time points at each site were determined from fluorescence (F) signals by calculating $(dF/dt)_{max}$ and $(d^2F/dt^2)_{max}$, which has been shown to

coincide with ~97% repolarization to baseline and recovery from refractoriness.[76] Local CV vectors were calculated for each pixel from the differences in activation time-points of that pixel (determined from $(dF/dt)_{max}$) and its 7 × 7 nearest neighbors, as previously described.[76] Local conduction velocities were averaged and represented as means ± standard deviation. Local CV can be overestimated when two wave fronts collide, transmural conduction occurs, or near the stimulation site where a small area of tissue was stimulated simultaneously. To correct this error, CVs greater than 1.0 m s^{-1} were removed from mean/standard deviation statistics. [136] In order to minimize the error propogation, the APDs were averaged over 10 beats from each pixel over 7 pixels and the CVs vectors were averaged over 10 individual local vectors.

4.3.4 Programmed stimulation

In order to test the vulnerability of hearts for AF, each of the hearts in the study was paced at the RA using programmed stimulation protocol consisting of 20 S1 pulses at 250 ms followed by a premature S2 pulse with a systematically shorter S1-S2 interval (*250 ms, 200-100 ms (steps of 20 ms), 100-60 ms (steps of 10 ms), 60-35 (steps of 5ms)*) until loss of capture or AF was induced.

4.3.5 Immuno-histology

RA and LA samples from the optically mapped hearts of the different groups were cryostat preserved, sectioned into tissue 5-6 microns thick, and mounted onto gel-coated glass slides. Slides were kept at –20°C until they were studied for immunohistochemistry. Tissue was rehydrated with washes of 1X PBS, 0.5% BSA blocking buffer, incubated with 2% BSA solution, and again washed with 0.5% BSA blocking buffer. They were then incubated with

primary antibody Collagen 1 (Chemicon 1:1000 diluted in BSA). Then tissue sections were washed with 0.5% BSA and then incubated with secondary antibody Cy3 diluted in BSA. After treatment with secondary antibody, slides were sequentially rinsed with 0.5% BSA blocking buffer and PBS before nuclei were labeled with Hoechst 33342 (Sigma). Slides were viewed with an Olympus (Melville, NY) Provis AX70 fluorescent miscroscope at 20X magnification. Images were collected with a cooled charge-coupled device camera (Optronics Magnifier; East Muskogee, OK) at a 12-bit gray depth and assembled (Adobe Photoshop; San Jose, CA). Fractional area of collagen 1 was analyzed using Metamorph software (Molecular Devices; Sunnyvale, CA).

4.3.6 Statistics

AF vulnerability between the different groups was compared using Fisher's exact test. Data are presented as mean ± standard deviation and parameters recorded under different S1-S2 were compared by ANCOVA. The results were considered significant for $p < 0.05$.

4.4 RESULTS

4.4.1 Atrial fibrillation inducibility

The vulnerability of the hearts to AF was tested in the different groups using programmed stimulation. In WKY hearts, a premature S1-S2 did not induce sustained AF (n = 0/4) (Figure 17

a, b), whereas in SHR hearts a premature S1-S2 = 55-75 ms induced transient AF that progressed to sustained AF (n = 5/5, $p < 0.01$ vs WKY) (Figure 17 c, d, e, f).

4.4.2 Optical mapping of atrial fibrillation

Figure 18 illustrates AP and Ca_iT from an SHR heart before and during S1-S2 induced AF. In all cases, Ca_i followed Vm, and Ca_i abnormalities did not precede AF (n = 3/3 hearts), unlike our previous reports regarding the initiation of EADs in Long QT syndrome 2 (LQT2).[4, 5] Activation maps exhibited a single reentrant circuit (Figure 19A) during the initiation of AF. Multiple daughter wavelets were created and annihilated during sustained AF (Figure 19B). Furthermore, during sustained AF, the right atrial (RA) dominant frequency (13.7 ± 1.4 Hz) was not significantly different from the left atrial (LA) dominant frequency (14.2 ± 0.8 Hz) (Figure 18D).

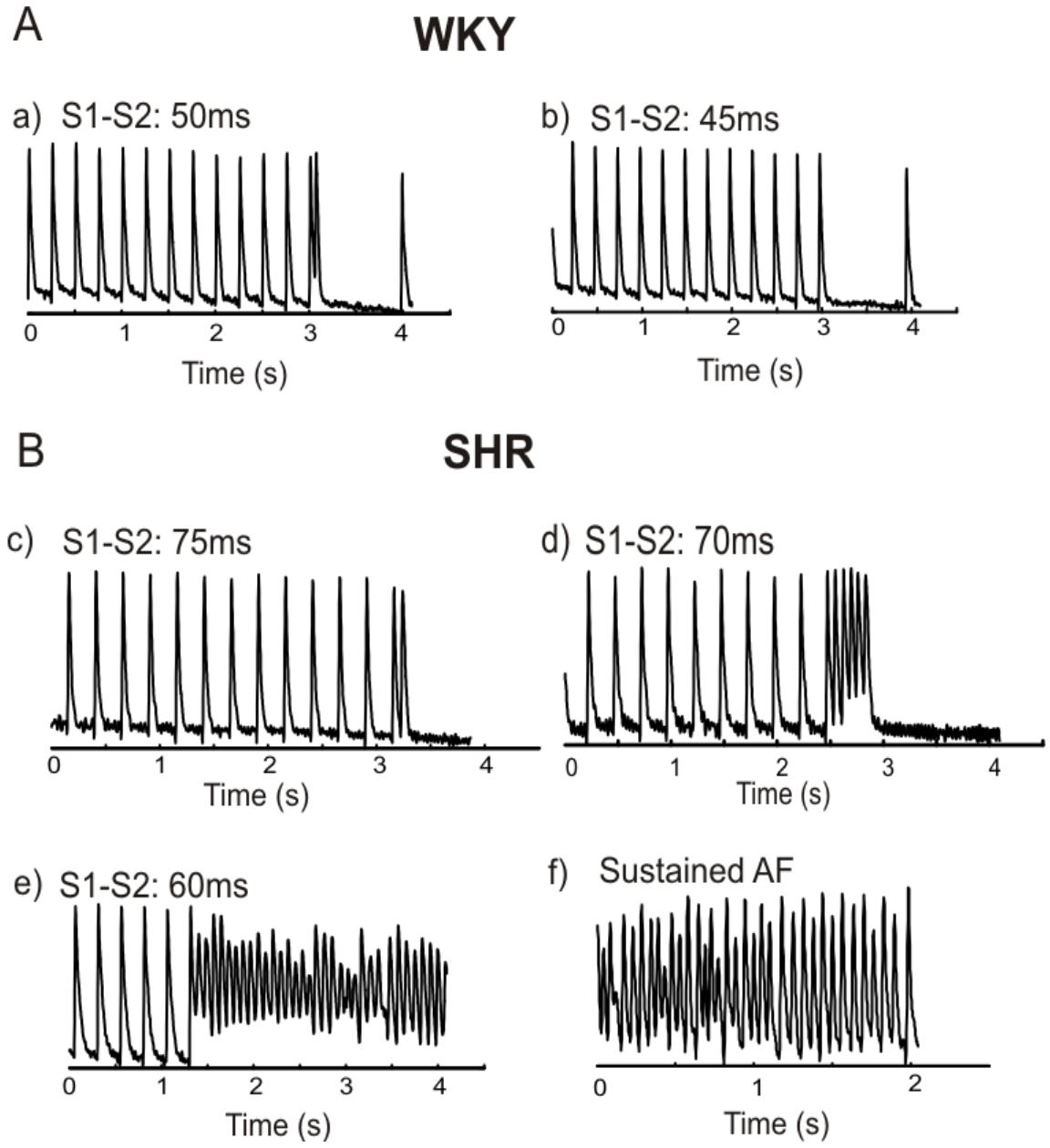

Figure 17: Inducibility of AF in normotensive and hypertensive rats

Representative action potential traces from the LA in normotensive WKY rats at (A) S1-S2 interval of 50 ms; (B) Application of earlier premature impulse at S1-S2 = 45 ms, results in loss of capture of S2. Representative action potential traces from LA of SHR rats (C) S1-S2 = 75 ms; (D) Initiation of non-sustained AF after earlier application of premature impulse at S1-S2 = 70 ms; (E) Induction of sustained AF at S1-S2 = 60 ms; (F) Zoomed in AP trace during sustained AF.

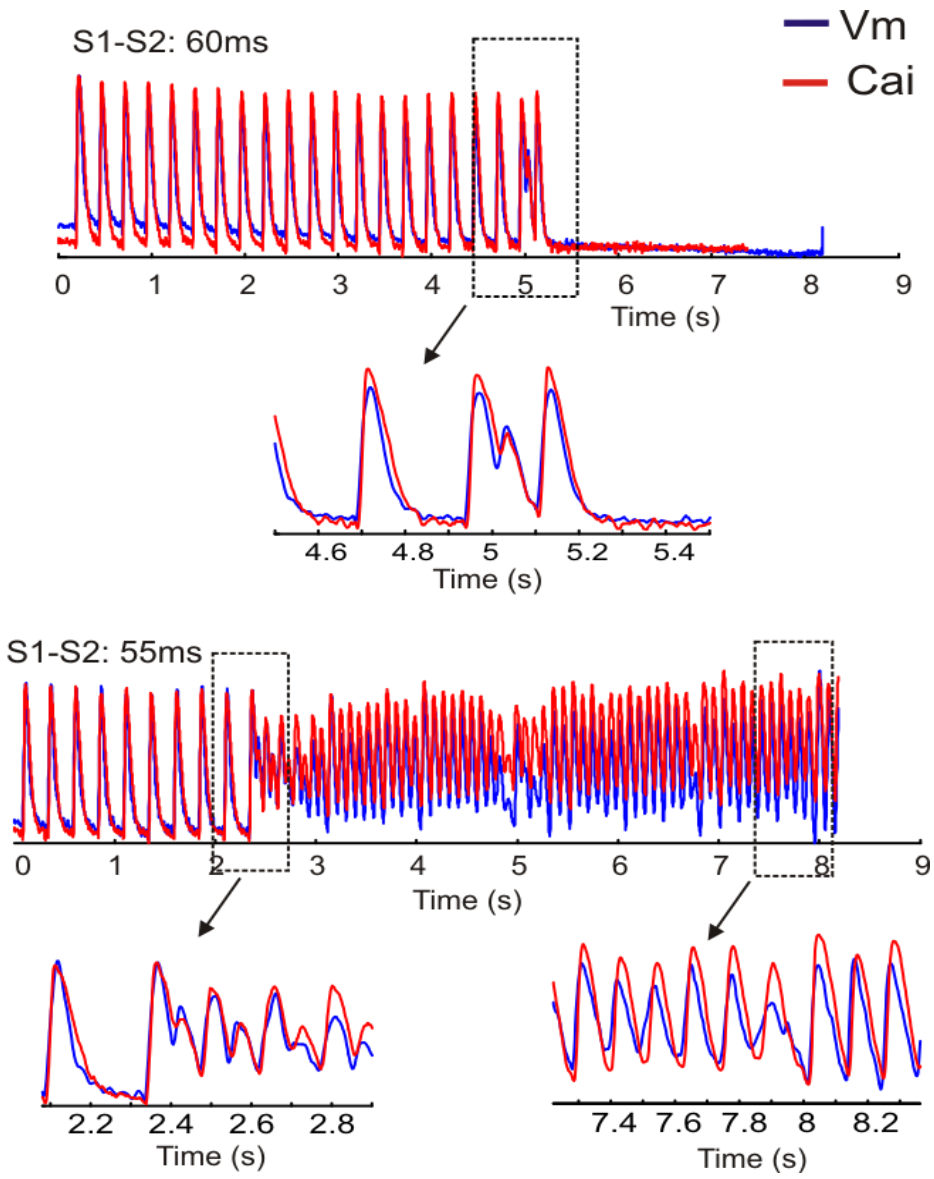

Figure 18: Role of Ca_i in AF inducibility

Superposition of AP and Ca_iT from LA of SHR. Blue lines indicate a change in the Vm signal while red lines indicate a change in Ca_i signals during (A) S1-S2 = 60 ms; (B) during the initiation of sustained AF at S1-S2 = 55 ms.

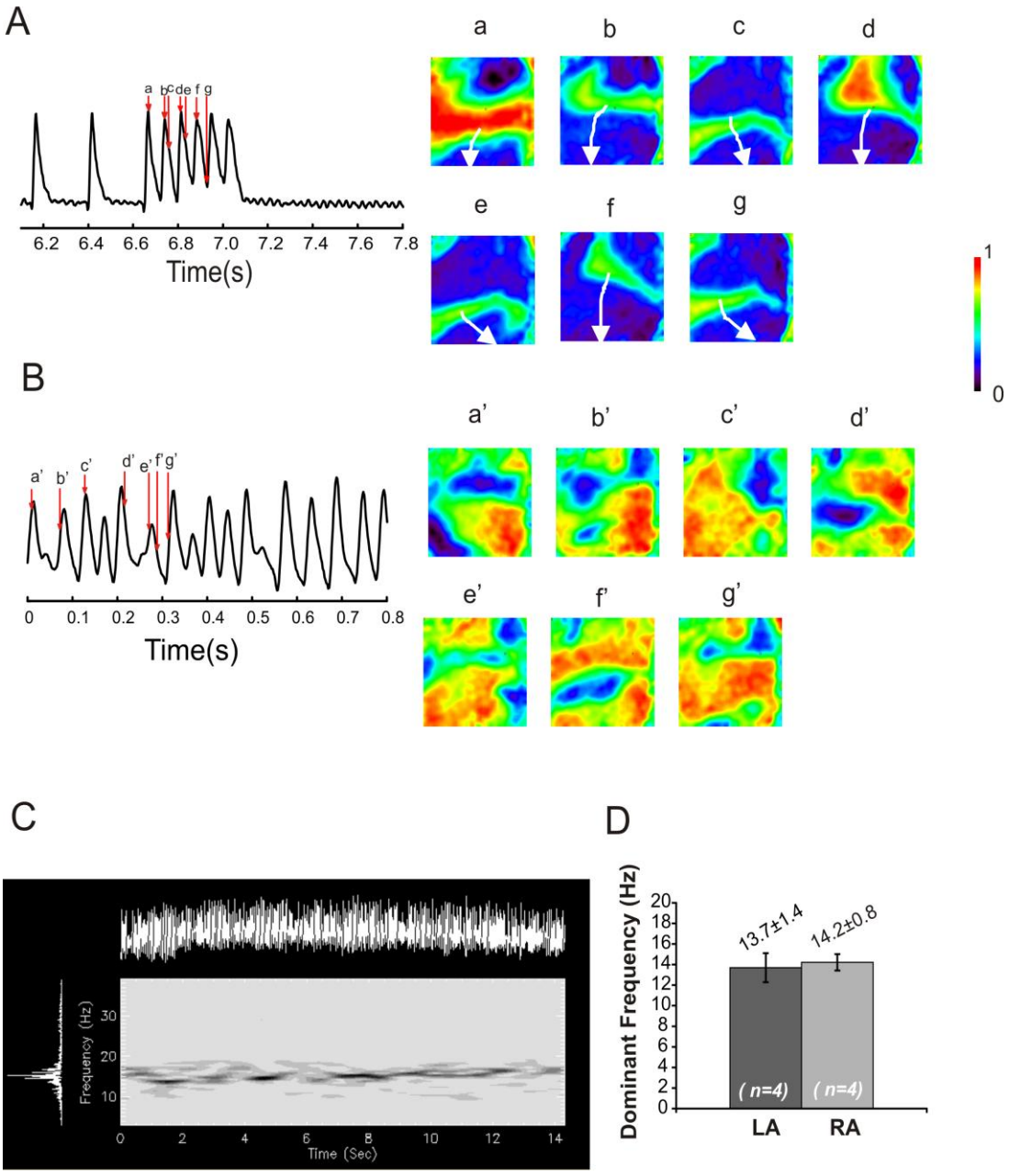

Figure 19: Analysis of the AF

(A) Activation pattern on a 100x100 pixel CMOS with spatial resolution of 150x150 μm^2 exhibiting a single reentrant circuit during non-sustained AF. (B) Activation pattern illustrating the creation and annihilation of multiple daughter waves (wavebreaks) during sustained AF. (C) Time-frequency analysis of AF. The spectrogram was calculated by sliding a 1.5-second Gaussian window over normalized optical traces. Top, Optical trace. Left, Overall FFT spectra. Contour map, spectrogram with isolines drawn every 12.5% of maximum. Spectrogram plots frequency (ordinate) versus time (abscissa) and is shown for 14 seconds of AF; the darker the color, the higher the energy density at that frequency. (D) Histogram represents the dominant frequencies during sustained AF in SHR rats in the LA and the RA.

4.4.3 In-vivo relaxin concentration and its effect on hemodynamic parameters

After 2 weeks of treatment, serum RLX concentration was significantly greater in SHR+RLX ($p < 0.001$) (Figure 19) compared to SHR+VEH. There were no significant differences in pre-treatment, mid-treatment (1 week), and post-treatment (2 weeks) tail blood pressure (BP) measurements (Table 4) between SHR+RLX and SHR+VEH (pretreatment: 154.3 mmHg for SHR+RLX vs. 164.5 mmHg for SHR+VEH, p = NS; mid-treatment: 156.3 mmHg for SHR+RLX vs. 164.6 for SHR+VEH, p = NS; post-treatment: 172.8 mmHg for SHR+RLX vs. 163.9 mmHg for SHR+VEH, p = NS).

Furthermore, there were no significant differences in heart rate at pre-treatment, mid-treatment, and post-treatment between SHR+RLX and SHR+VEH (pretreatment: 426.9 for SHR+RLX vs. 398.7 for SHR+VEH, p = NS; mid-treatment: 464.7 for SHR+RLX vs. 399.9 for SHR+VEH, p = NS; post-treatment: 483.1 for SHR+RLX vs. 429.6 for SHR+VEH, p = NS). There was a significant increase in HR following treatment with relaxin in the SHR+RLX group (pretreatment: pretreatment: 426.9 vs. post-treatment: 483.1, $p < 0.05$).

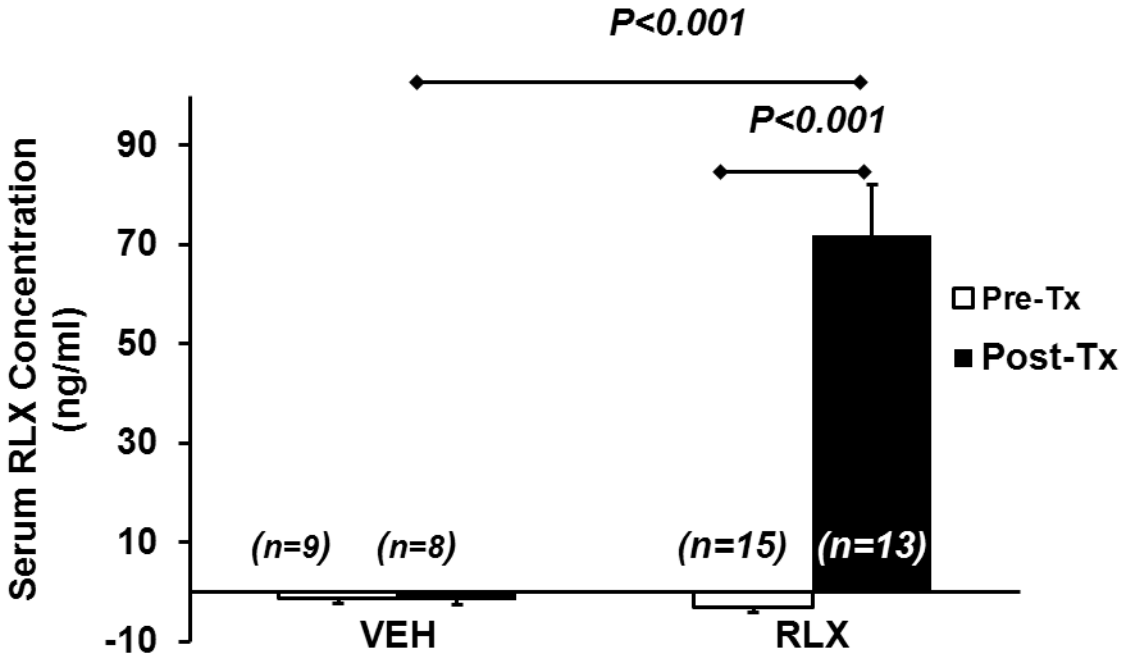

Figure 20: Blood Serum Relaxin Concentration

Blood Serum RLX concentration pre and post treatment in SHR implanted with mini-pumps containing either RLX or VEH.

Table 3: Effect of relaxin on hemodynamic parameters

	Pre-Tx		**Mid-Tx**		**Post-Tx**	
	SHR+RLX	**SHR+VEH**	**SHR+RLX**	**SHR+VEH**	**SHR+RLX**	**SHR+VEH**
Tail BP (mmHg)	154.3 ± 6.9 (10)	164.5 ± 16.4 (4)	156.3 ± 10.4 (6)	164.6 ± 1.2 (3)	172.8 ± 6.9 (5)*****	163.9 ± 19.4 (2)
HR (BPM)	426.9 ± 18.3 (10)	398.7 ± 26.9 (4)	464.7 ± 19.1 (4)	399.9 ± 45.1 (3)	483.1 ± 11.8 (5)	429.6 ± 44.6 (2)

* versus Pre-TX (SHR+RLX) $p < 0.05$

4.4.4 Effect of relaxin on AF inducibility

Treatment with RLX for 2 weeks suppressed AF inducibility in SHR (n = 1/6) (Figure 20 a, b), while VEH treatment in SHR failed to suppress AF inducibility (n = 4/4; $p < 0.01$ vs. SHR+RLX) (Figure 20 c, d).

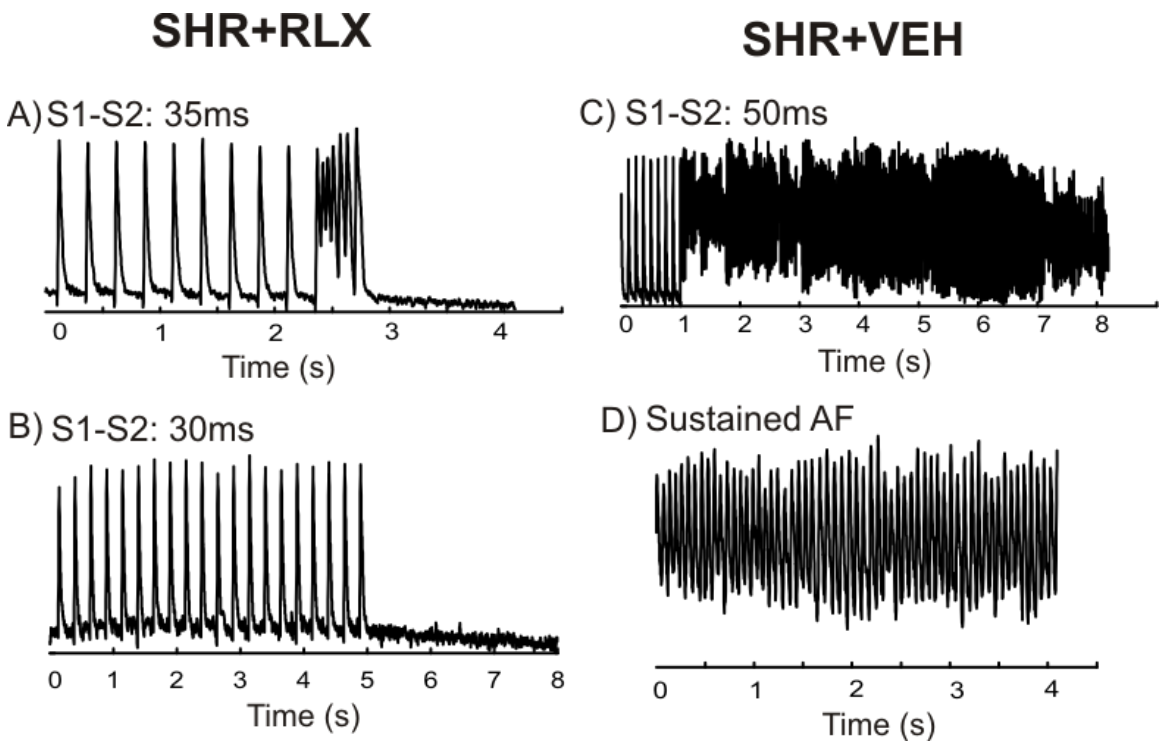

Figure 21: Effect of relaxin on AF inducibility in SHR

Exemplary voltage (Vm) trace of LA of SHR+RLX treated heart (A) Non-sustained AF initiation at S1-S2 = 35 ms. (B) Earlier application of the premature impulse at S1-S2 = 30 ms results in loss of capture of S2. (C) Representative Vm trace of LA of SHR+VEH treated heart at S1-S2 = 50 ms, which initiated sustained AF (D) Vm trace during sustained AF.

4.4.5 Action Potential Duration (APD) and Conduction Velocity (CV) restitution

Atrial differences in APDs and CVs between WKY, SHR, SHR+VEH and SHR+RLX are shown in Figure 21. APD in the SHR were significantly shorter then APDs in WKY at the RA ($p < 0.05$) and the LA ($p < 0.05$). There was no statistical significant between APDs at the RA and LA between RLX treated and untreated or vehicle treated SHR.

CV measurements revealed a significantly slower CV in the LA of SHR compared to WKY ($p < 0.01$). RLX-treatment increased the LA-CV compared to SHR ($p < 0.05$). RA-CV measurements were not significantly different for SHR vs. WKY. RLX-treated SHR showed no significant CV compared to SHR and SHR+VEH.

4.4.6 Histological findings

Differences in LA and RA fibrosis levels between the different groups are shown in Figure 22. SHR had a significantly greater collagen to tissue ratio in both the RA and LA compared to WKY ($p < 0.05$). There was no significant difference in collagen to tissue ratio in both the RA and LA between SHR and SHR+VEH. RLX treatment attenuated the fibrosis within 2 weeks in SHR as SHR+RLX had a significantly lower collagen per fractional area compared to SHR and SHR+VEH ($p < 0.05$).

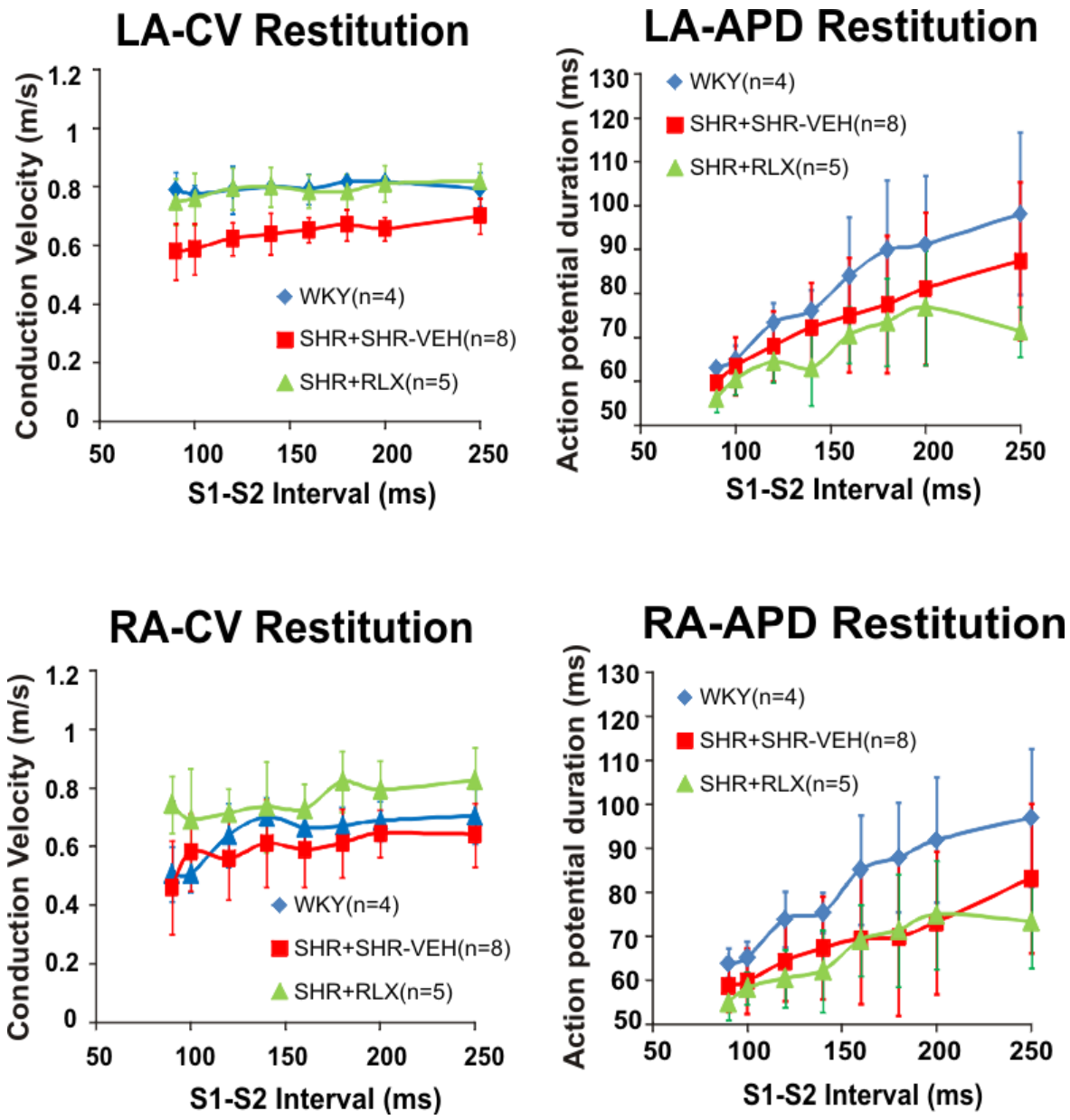

Figure 22: Action Potential Duration (APD) and Conduction Velocity (CV) Restitution kinetics

(A) Left Atrium (LA) mean APD and Conduction Velocity (CV) measurements as a function of S1-S2 interval. All values are reported as mean ± SD. APD-SHR vs. WKY: $p < 0.05$; APD-SHR+RLX vs. SHR p = NS. CV-SHR vs. WKY: $p < 0.01$; CV-SHR vs. SHR+RLX: $p < 0.05$ (B) Right Atrium (RA) mean APD and CV measurements as a function of S1-S2 interval. All values are reported as mean ± SD. APD-SHR vs. WKY: $p < 0.05$; APD-SHR+RLX vs. SHR+VEH p = NS. CV-SHR vs. WKY: p = NS; CV-SHR vs. SHR+RLX: p = NS.

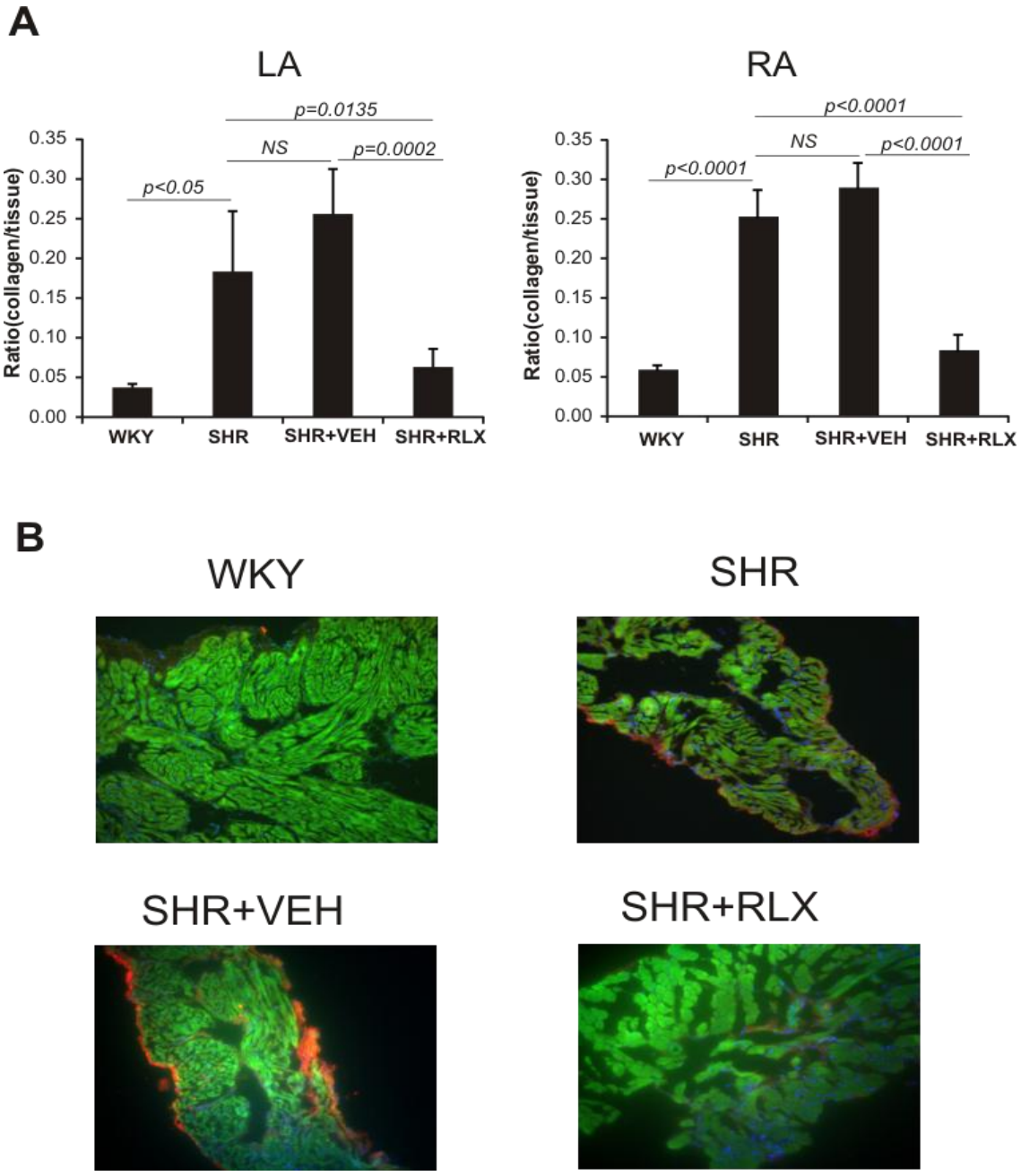

Figure 23: Fibrotic remodeling of atria and its reversal with relaxin

(A) LA and RA collagen I expression as percent of fractional area for WKY, SHR, SHR+VEH, and SHR+RLX. All values are reported as mean ± SD. (B) Representative immuno-histological sections at 20X magnification of age-matched male LA of WKY, SHR, SHR+RLX, SHR+VEH. Phalloidin is represented in green; Collagen I is shown in red.

4.5 DISCUSSION

4.5.1 Main findings

In this study, we showed that SHR have higher susceptibility to AF triggered by a premature impulse. SHR atria had a slower CV and higher levels of collagen deposition and fibrosis. RLX-treatment for 2 weeks significantly reversed fibrosis, increased atrial CV, and suppressed the AF phenotype in SHR.

4.5.2 Atrial fibrosis and AF

Atrial fibrosis has been implicated in the pathogenesis of AF. Fibrosis was the most common finding from histological studies done on the hearts of patients with primary AF.[137] Our histological studies support the notion that hypertension leads to fibrosis mediated structural remodeling and an increase in collagen I/III levels. In addition, SHR atria are characterized by conduction abnormalities that provide a basis for lines of conductional block and re-entry as seen in optical mapping studies. AF can be maintained by either sustained rapid ectopic activity or by re-entry. Re-entry depends on the fine balance between the cellular refractoriness and conduction velocity. The chances of potential re-entry is increased with a short refractoriness or/and slow conduction. Re-entry terminates if refractoriness is prolonged (prolonging APD) or if conduction is accelerated, as it encounters tissue that is still refractory and dies out.[138]

The major pathways that have been proposed for the initiation and maintenance of AF are the multiple wavelet theory[139], focal activity hypothesis[140] and single circuit reentrant theory.[141] Our optical mapping studies were consistent with an AF generated by the continuous annihilation and creation of daughter wavelets that lead to sustained AF which supported the multiple wavelet theory as the dominant mechanism of AF in SHR.

4.5.3 Anti-fibrotic and antiarrhythmic properties of relaxin and its clinical relevance

Relaxin mediates effects on the cardiovascular system via multiple different pathways. It activates a wide range of signaling pathways mostly by interacting with the relaxin family peptide receptor 1 (RXFP1), a G protein coupled receptor that leads to an acute elevation of cyclic AMP (cAMP) and nitric oxide (NO).[142] In other studies, RLX has been shown to inhibit fibroblast proliferation, differentiation, collagen synthesis, collagen deposition and an increase in MMP-2 expression, which most likely contributed to an increase in collagen degradation and a decrease in collagen deposition.[143]

Targeting fibrosis has been done before using ACE inhibitors, ARBs, and a novel compound Pirfenidone. However, most of these studies have examined models of heart failure, which is less commonly associated with AF than hypertension. Pirfenidone has been shown to reverse fibrosis and attenuate AF in a CHF canine model.[144] With treatment with Pirfenidone, they showed reversal of atrial fibrosis and reduced vulnerability of AF after burst pacing but did not see a significantly greater increase in atrial CV. In contrast our data shows that low dosage treatment with RLX reduces AF inducibility, increases atrial CV and decreases atrial fibrosis levels.

4.5.4 Efficacy and safety

RLX has been under clinical trials for acute heart failure with a completed 234-patient phase 2 and an ongoing 160-patient phase 3.[145] Clinical use of RLX has not been associated with serious adverse effects and toxicity. Reports have confirmed the safety of RLX infusion in humans (upto 960 (µg/kg)/day) and have noted a vasodilatory effect in patients with HF, but RLX therapy did not always improve renal functions.[146] The clinical trials to date have sensibly addressed potential benefits of short-term treatment in vasodilation, but have not examined whether other pathways mediated by RLX can be exploited to provide therapeutic benefits.

4.6 LIMITATIONS

Our studies were done on SHR, which have found to have hypertension similar to humans.[147] However, the structural remodeling of hypertension and mechanisms of AF may be different in hypertensive humans compared to SHR. We do not know the amount of time required for atrial fibrosis and susceptibility for AF to return following treatment of SHR with 2 weeks of RLX. We are using a very high dose of RLX in these studies, but we do not know the minimum dosage required to reliably prevent AF susceptibility.

Phase III clinical study using RLX for the treatment of sclerosis revealed abrupt appearance of severe hypertension and renal impairment in a number of the patients who had to interrupt active RLX therapy.[148] These adverse effects of RLX were reported only among patients with systemic sclerosis, only a small number of individuals without scleroderma have

received treatment with RLX and there needs to be more studies looking at the effect of RLX on healthy individuals.

4.7 CONCLUSION

SHR had increased levels of atrial fibrosis leading to slower CV and greater AF inducibility compared to WKY rats. 2 week treatment of RLX significantly reduced fibrosis, improved CV, and attenuated AF inducibility in SHR. In RLX-treated SHR, collagen deposition reversed to control levels found in WKY hearts along with an increase in metallo-proteinase 6 and 9 levels and an increase in CV ($p < 0.01$, SHR, SHR+V). This study implicates the relationship between fibrosis as the underlying abnormality of myocardial substrate that leads to AF and provides compelling evidence that reversal of fibrosis, by drugs such as RLX may provide a novel therapy in the management of AF.

APPENDIX A

SYMPATHETIC NERVE STIMULATION GENERATES REGIONAL HETEROGENEITIES OF Ca^{2+} TRANSIENTS IN RABBIT VENTRICLES

Authors: Rajkumar Mantravadi[1, 2], Ashish Parikh[2], Bethan Gabris[2] and Guy Salama[2].

[1] University of Leicester, UK, [2] University of Pittsburgh, Pittsburgh, PA. *Heart Rhythm, Vol 7, No. 5, May Supplement 2010, S9.*

Introduction: Higher sympathetic innervation at the base compared to the apex has been recognized from anatomical and functional studies using optical mapping of cardiac action potentials (AP) during sympathetic nerve stimulation (SNS). SNS increases heart rate and reduces AP durations more at the base than the apex resulting in a reversal of repolarization gradients and apex-base differences in restitution kinetics. However, the effects of SNS on intracellular Ca^{2+} transients (Ca_iT) across the surface of the intact heart are unknown.

Methods: Langendorff rabbit hearts were isolated with autonomic nerves, stained with voltage sensitive (RH237) and Ca^{2+} indicator (Rhod-2/AM) dyes and were optically mapped at normal sinus rate (SR) and during SNS (15V; 15Hz) using an electrode inserted in the spinal canal to control sympathetic outflow. Ca_i dynamics were compared for SR vs. SNS and apex vs. base by measuring: CaiT durations (90% recovery to baseline), V_m-Ca_i delay (cross correlation

analysis), Risetime (time-to-peak) and peak Cai (ΔCai: % change). Data were expressed as mean ± SEM and paired t-test with $p < 0.05$ considered significant.

Results: The figure summarizes the findings and shows that SNS produced significantly shorter Vm-Ca delay, shorter CaiT durations, shorter rise-time but higher peak Ca_i at the base compared to the apex.

Conclusions: The data provides new insights on the regional effects of SNS on Ca^{2+} handling and highlights large regional heterogeneities of local Ca_i properties of the myocardium caused by heterogeneities of sympathetic innervation.

APPENDIX B

DAURICINE SUPPRESSES EARLY AFTERDEPOLARIZATIONS AND TORSADE DE POINTES IN RABBIT HEARTS WITH LONG QT 2 SYNDROME

Authors: Ashish A Parikh[1]; Xiao-Yan Yang[2]; Fan-Dian Zeng[2]; Guy Salama[1]

[1] Cardiovascular Institute, Univ of Pittsburgh, Pittsburgh, PA, [2] Pharmacology, Tongji Med College, Wuhan, China. *Circulation.2011; 124: A8917*

Background: Dauricine (Dau) is a bisbenzylisoquinoline alkaloid derivative isolated from rhizome of Mensipermum dauricium DC, a Chinese herb. Dau has been shown to lower blood pressure, platelet aggregation, inflammatory response and arrhythmia. Dau has also been shown to inhibit the late Na^+ current, $I_{Na,Late}$, I_{Kr} and L-type Ca^{2+} current, $I_{Ca,L}$ by shifting the steady state inactivation and activation curves and prolonging the τ value of recovery.

Objectives: The multiple targets of Dau make it challenging to explain the suppression of early afterdepolarizations (EADs) and Torsade de Pointes (TdP) in drug-induced Long QT 2 (LQT2) model in rabbit hearts by mapping Action Potential (AP) and Ca^{2+} transients (Ca_iT) and to mathematically model the effect of Dau and explain its possible mode of action.

Methods: Experimental (Langendorff rabbit hearts labelled with Rhod-2/AM and PGH1 to simultaneously map Action Potential (AP) and Ca^{2+} transients (Ca_iT)) and simulations

(*Shannon et al*. model) of rabbit AP and CaiT were used to investigate the effects of Dau (5μM) before and after LQT2 induced with Dofetilide (Dofe=0.5 μM) to block I_{Kr}.

Results: In controls, Dau tended to prolong AP durations (APDs), CaiT durations (CTD) ($p>0.5$) but significantly reduced conduction velocity (CV) ($p < 0.05$; $n = 5$) in a rate independent manner. In LQT2, Dofe prolonged APDs (318 ± 24 ms to 835 ± 32 ms; $p < 0.01$), CTDs (346 ± 36 ms to 867 ± 48 ms; $p < 0.01$) elicited EADs and TdP that were suppressed by Dau ($p < 0.01$; $n = 5/5$ hearts). Dau (5 μM) reduced the Dofe-prolongation of APDs (835 ± 32 ms to 542 ± 93 ms; $p < 0.01$) and CTD (867 ±4 8 ms to 567 ± 103 ms; $p < 0.01$) and reversed the Dofe-prolongation of Dispersion of Repolarization (DOR) (25 ± 6 to 55 ± 15 ms; $p < 0.01$; reversed 55 ± 15 ms to 29 ± 15 ms; $p < 0.05$). Simulations of the effects of Dofe, Dau and Dofe + Dau indicate that Dau's suppression of EADs is primarily mediated by reducing the Ca_i overload by modifying the kinetics of I_{CaL}.

Conclusions: Dau (5 μM) markedly reduced CV and in LQT2 significantly shortening APDs, CTDs, reduced DOR and suppressed EADs and TdP. Simulations implicate the slowing down of activation and inactivation kinetics of $I_{Ca,L}$ as the dominant antiarrhythmic mechanism.

APPENDIX C

RANOLAZINE STABILIZES CARDIAC RYANODINE RECEPTORS: A NOVEL MECHANISM FOR THE SUPPRESSION OF EARLY AFTERDEPOLARIZATION AND TORSADES DE POINTES IN LONG QT TYPE 2

Authors: Ashish Parikh, MEng, Rajkumar Mantravadi, MD, PhD, Dmitry Kozhevnikov, MD, Michael A. Roche, BS, Yanping Ye, BS, Laura J. Owen, BS, Jose Luis Puglisi, PhD, Jonathan J. Abramson, PhD, Guy Salama, PhD, FHRS. *Heart Rhythm, Volume 9, Issue 6, Pages 953-960, June 2012*

Background: Ranolazine (Ran) is known to inhibit multiple targets, including the late Na^+current, the rapid delayed rectifying K^+current, the L-type Ca^{2+}current, and fatty acid metabolism. Functionally, Ran suppresses early afterdepolarization (EADs) and torsades de pointes (TdP) in drug-induced long QT type 2 (LQT2) presumably by decreasing intracellular $[Na^+]_i$ and Ca^{2+}overload. However, simulations of EADs in LQT2 failed to predict their suppression by Ran.

Objective: To elucidate the mechanism(s) whereby Ran alters cardiac action potentials (APs) and cytosolic Ca^{2+}transients and suppresses EADs and TdP in LQT2.

Methods: The known effects of Ran were included in simulations (Shannon and Mahajan models) of rabbit ventricular APs and Ca^{2+}transients in control and LQT2 models and compared

with experimental optical mapping data from Langendorff rabbit hearts treated with E4031 (0.5 μM) to block the rapid delayed rectifying K^+current. Direct effects of Ran on cardiac ryanodine receptors (RyR2) were investigated in single channels and changes in Ca^{2+}-dependent high-affinity ryanodine binding.

Results: Ran (10 μM) alone prolonged action potential durations (206 ± 4.6 to 240 ± 7.8 ms; *P* <0.05); E4031 prolonged action potential durations (204 ± 6 to 546 ± 35 ms; *P* <0.05) and elicited EADs and TdP that were suppressed by Ran (10 μM; n = 7 of 7 hearts). Simulations (Shannon but not Mahajan model) closely reproduced experimental data except for EAD suppression by Ran. Ran reduced open probability (P_o) of RyR2 (half maximal inhibitory concentration = 10 ± 3 μM; n = 7) in bilayers and shifted half maximal effective concentration for Ca^{2+}-dependent ryanodine binding from 0.42 ± 0.02 to 0.64 ± 0.02 μM with 30 μM Ran.

Conclusions: Ran reduces P_o of RyR2, desensitizes Ca^{2+}-dependent RyR2 activation, and inhibits Ca_i oscillations, which represents a novel mechanism for its suppression of EADs and TdP.

APPENDIX D

MATLAB CODE FOR SHANNON MODEL

```
function rabbit
%%Modified from Pepe's code
clear all
%% Initial conditions
mo=1.405627e-3;
ho= 9.867005e-1;
jo=9.915620e-1;
do=7.175662e-6;
fo=1.000681;
fcaBjo=2.421991e-2;
fcaBslo=1.452605e-2;
xtoso=4.051574e-3;
ytoso=9.945511e-1;
xtofo=4.051574e-3;
ytofo= 9.945511e-1;
xkro=8.641386e-3;
xkso= 5.412034e-3;
RyRro=8.884332e-1;
RyRoo=8.156628e-7;
RyRio=1.024274e-7;
NaBjo=3.539892;
NaBslo=7.720854e-1;
TnCLo=8.773191e-3;
TnCHco=1.078283e-1;
TnCHmo=1.524002e-2;
CaMo=2.911916e-4;
Myoco=1.298754e-3;
Myomo=1.381982e-1;
SRBo=2.143165e-3;
SLLjo=9.566355e-3;
SLLslo=1.110363e-1;
SLHjo=7.347888e-3;
SLHslo=7.297378e-2;
Csqnbo= 1.242988;
```

```
Ca_sro=0.7*5.545201e-1;
Najo=8.80329;
Naslo=8.80733;
Naio=8.80853;
Kio=135;
Cajo=1.737475e-4;
Caslo= 1.031812e-4;
Caio=8.597401e-5;
Vmo=-8.556885e+1;
rtoso=0.9946;
% Gating variables
%  1      2      3      4      5      6      7      8      9      10     11     12     13
%% m      h      j      d      f      fcaBj  fcaBsl xtos   ytos   xtof   ytof   xkr    xks
%y10=[1.2e-3;0.99;  0.99;  0.0;   1.0;   0.0141; 0.0141;   0;     1;     0.0;   1.0;   0.0;   6e-3;];
y10=[mo; ho; jo; do; fo; fcaBjo; fcaBslo; xtoso; ytoso; xtofo; ytofo; xkro; xkso;];
% RyR and Buffering variables
%  14     15     16     17     18     19     20     21     22     23     24
%% RyRr   RyRo   RyRi   NaBj   NaBsl  TnCL   TnCHc  TnCHm  CaM    Myoc   Myom
y20=[RyRro; RyRoo; RyRio; NaBjo; NaBslo; TnCLo; TnCHco; TnCHmo; CaMo; Myoco; Myomo;];
%y20=[1;    0;     0;     1.8;   0.8;   0.012;  0.112;  0.01;   0.4e-3; 1.9e-3; 0.135;];
% More buffering variables
%  25     26     27     28     29     30
%% SRB    SLLj   SLLsl  SLHj   SLHsl  Csqnb
y30=[SRBo; SLLjo; SLLslo; SLHjo; SLHslo; Csqnbo];
%y30=[3.3e-3; 0.012; 0.012; 0.13;  0.13;  1.5;];
%  Intracellular concentrations/ Membrane voltage
%  31     32     33     34     35     36     37     38     39    40
%% Ca_sr  Naj    Nasl   Nai    Ki     Caj    Casl   Cai    Vm    rtos
y40=[Ca_sro; Najo; Naslo; Naio; Kio; Cajo; Caslo; Caio; Vmo; rtoso; ];
% y50=[TSao; TSpo; TSwo; TSro; Lo; Lmo; Xpo; Xwo; Fmo];
%y40=[0.9;   8.8;   8.8;   8.8;   135;   0.1e-3; 0.1e-3; 0.1e-3; -88;  0.89; 0;       0;];
% y50=[UIC3o; UIC2o; UIFo; UIM1o; UC3o; UC2o; UC1o; UOo; UIM2o; LC3o; LC2o; LC1o; LOo ];
% Put everything together
y0  = [y10;y20;y30;y40] %;y50];
%% Single Run Simulation
tspan = [0;200e3];
options = odeset('RelTol',1e-5,'MaxStep',1,'Stats','on');
[t,y] = ode15s(@f,tspan,y0,options);
subplot(2,1,1)
plot(t,y(:,39))
subplot(2,1,2)
plot(t,y(:,38),'r')

d=y(:,4);
f=y(:,5);
fcaBj=y(:,6);
fcaBsl=y(:,7);
Caj=y(:,36);
Casl=y(:,37);
Vm = y(:,39);
Cai = y(:,38);
Naj=y(:,32);
Nasl=y(:,33);

fid=fopen('C:/Documents and Settings/Ashish Parikh/Desktop/2000.txt','w')
fprintf(fid,' t   vm    cai    d    f    fcaBj   fcaBsl   Caj   Casl   Naj  Nasl\n');
```

```
	for i=1:length(t)
		fprintf(fid,'%10.4f %10.4f %10.7f %10.7f %10.7f %10.7f %10.7f %10.7f %10.7f %10.7f %10.7f \n', t(i), Vm(i),Cai(i),d(i),f(i),fcaBj(i),fcaBsl(i),Caj(i),Casl(i),Naj(i),Nasl(i));
	end
	fclose(fid)
	end

	%%

	function ydot = f(t,y)

	ydot = zeros(size(y));

	%% Model Parameters
	% Constants
	R = 8314;       % [J/kmol*K]
	Frdy = 96485;   % [C/mol]
	Temp = 310;     % [K]
	FoRT = Frdy/R/Temp;
	Cmem = 1.3810e-10;   % [F] membrane capacitance
	Qpow = (Temp-310)/10;

	% Cell geometry
	cellLength = 100;     % cell length [um]
	cellRadius = 10.25;   % cell radius [um]
	junctionLength = 160e-3;  % junc length [um]
	junctionRadius = 15e-3;   % junc radius [um]
	distSLcyto = 0.45;    % dist. SL to cytosol [um]
	distJuncSL = 0.5;  % dist. junc to SL [um]
	DcaJuncSL = 1.64e-6;  % Dca junc to SL [cm^2/sec]
	DcaSLcyto = 1.22e-6; % Dca SL to cyto [cm^2/sec]
	DnaJuncSL = 1.09e-5;  % Dna junc to SL [cm^2/sec]
	DnaSLcyto = 1.79e-5;  % Dna SL to cyto [cm^2/sec]
	Vcell = pi*cellRadius^2*cellLength*1e-15;    % [L]
	Vmyo = 0.65*Vcell; Vsr = 0.035*Vcell; Vsl = 0.02*Vcell; Vjunc = 0.0539*.01*Vcell;
	SAjunc = 20150*pi*2*junctionLength*junctionRadius;  % [um^2]
	SAsl = pi*2*cellRadius*cellLength;          % [um^2]

	J_ca_juncsl = 1/1.2134e12; % [L/msec] = 8.2413e-13
	J_ca_slmyo = 1/2.68510e11; % [L/msec] = 3.2743e-12
	J_na_juncsl = 1/(1.6382e12/3*100); % [L/msec] = 6.1043e-13
	J_na_slmyo = 1/(1.8308e10/3*100);  % [L/msec] = 5.4621e-11

	% Fractional currents in compartments
	Fjunc = 0.11;   Fsl = 1-Fjunc;
	Fjunc_CaL = 0.9; Fsl_CaL = 1-Fjunc_CaL;

	% Fixed ion concentrations
	Cli = 15;   % Intracellular Cl  [mM]
	Clo = 150;  % Extracellular Cl  [mM]
	Ko = 5.4;   % Extracellular K   [mM]
	Nao = 140;  % Extracellular Na  [mM]
	Cao = 1.8;  % Extracellular Ca  [mM]
	Mgi = 1;    % Intracellular Mg  [mM]

	% Nernst Potentials
```

```
ena_junc = (1/FoRT)*log(Nao/y(32));     % [mV]
ena_sl = (1/FoRT)*log(Nao/y(33));       % [mV]
ek = (1/FoRT)*log(Ko/y(35));              % [mV]
eca_junc = (1/FoRT/2)*log(Cao/y(36));   % [mV]
eca_sl = (1/FoRT/2)*log(Cao/y(37));     % [mV]
ecl = (1/FoRT)*log(Cli/Clo);            % [mV]

% Na transport parameters

GNa=16;
GNaB = 0.297e-3;    % [mS/uF]
IbarNaK = 1.90719;     % [uA/uF]
KmNaip = 11;         % [mM]
KmKo = 1.5;         % [mM]
Q10NaK = 1.63;
Q10KmNai = 1.39;

%% K current parameters
pNaK = 0.01833;
GtoSlow = 0.06*1;     % [mS/uF] %0.09 CaMKII
GtoFast = 0.02*1;     % [mS/uF]
gkp = 0.001;

% Cl current parameters
GClCa = 0.109625;   % [mS/uF]
GClB = 9e-3;        % [mS/uF]
KdClCa = 100e-3;    % [mM]

% I_Ca parameters
pNa = 1.5e-8;       % [cm/sec]
pCa = 5.4e-4;       % [cm/sec]
pK = 2.7e-7;        % [cm/sec]
Q10CaL = 1.8;

% Ca transport parameters
IbarNCX = 9.0;      % [uA/uF]IbarNCX
KmCai = 3.59e-3;    % [mM]
KmCao = 1.3;        % [mM]
KmNai = 12.29;      % [mM]
KmNao = 87.5;       % [mM]
ksat = 0.27;        % [none]
nu = 0.35;          % [none]
Kdact = 0.256e-3;   % [mM]
Q10NCX = 1.57;      % [none]
IbarSLCaP = 0.0673; % [uA/uF](2.2 umol/L cytosol/sec)
KmPCa = 0.5e-3;     % [mM]
GCaB = 2.513e-4;    % [uA/uF]
Q10SLCaP = 2.35;    % [none]

% SR flux parameters
Q10SRCaP = 2.6;          % [none]
Vmax_SRCaP = 5.3114e-3;  % [mM/msec] (286 umol/L cytosol/sec)
Kmf = 0.246e-3;          % [mM] default
%Kmf = 0.175e-3;          % [mM]
Kmr = 1.7;               % [mM]L cytosol
hillSRCaP = 1.787;       % [mM]
```

```
ks = 25;                % [1/ms]
koCa = 10;              % [mM^-2 1/ms]   %default 10   modified 20
kom = 0.06;             % [1/ms]
kiCa = 0.5;             % [1/mM/ms]
kim = 0.005;            % [1/ms]
ec50SR = 0.45;          % [mM]

% Buffering parameters
% Note: we are using [1/ms] and [1/mM/ms], which differs from that in the paper
% koff: [1/s] = 1e-3*[1/ms];  kon: [1/uM/s] = [1/mM/ms]
Bmax_Naj = 7.561;       % [mM]  % Na buffering
Bmax_Nasl = 1.65;       % [mM]
koff_na = 1e-3;         % [1/ms]
kon_na = 0.1e-3;        % [1/mM/ms]
Bmax_TnClow = 70e-3;    % [mM]                  % TnC low affinity
koff_tncl = 19.6e-3;    % [1/ms]
kon_tncl = 32.7;        % [1/mM/ms]
Bmax_TnChigh = 140e-3;  % [mM]                  % TnC high affinity
koff_tnchca = 0.032e-3; % [1/ms]
kon_tnchca = 2.37;      % [1/mM/ms]
koff_tnchmg = 3.33e-3;  % [1/ms]
kon_tnchmg = 3e-3;      % [1/mM/ms]
Bmax_CaM = 24e-3;       % [mM]  % CaM buffering
koff_cam = 238e-3;      % [1/ms]
kon_cam = 34;           % [1/mM/ms]
Bmax_myosin = 140e-3;   % [mM]                  % Myosin buffering
koff_myoca = 0.46e-3;   % [1/ms]
kon_myoca = 13.8;       % [1/mM/ms]
koff_myomg = 0.057e-3;  % [1/ms]
kon_myomg = 0.0157;     % [1/mM/ms]
Bmax_SR = 19*.9e-3;     % [mM] (Bers text says 47e-3) 19e-3
koff_sr = 60e-3;        % [1/ms]
kon_sr = 100;           % [1/mM/ms]
Bmax_SLlowsl = 37.4e-3*Vmyo/Vsl;        % [mM]    % SL buffering
Bmax_SLlowj = 4.6e-3*Vmyo/Vjunc*0.1;    % [mM]
koff_sll = 1300e-3;     % [1/ms]
kon_sll = 100;          % [1/mM/ms]
Bmax_SLhighsl = 13.4e-3*Vmyo/Vsl;       % [mM]
Bmax_SLhighj = 1.65e-3*Vmyo/Vjunc*0.1;  % [mM]
koff_slh = 30e-3;       % [1/ms]
kon_slh = 100;          % [1/mM/ms]
Bmax_Csqn = 140e-3*Vmyo/Vsr;            % [mM] % Bmax_Csqn = 2.6;      % Csqn buffering
koff_csqn = 65;         % [1/ms]
kon_csqn = 100;         % [1/mM/ms]


%% Membrane Currents
% I_Na: Fast Na Current
am = 0.32*(y(39)+47.13)/(1-exp(-0.1*(y(39)+47.13)));
bm = 0.08*exp(-y(39)/11);
if y(39) >= -40
   ah = 0; aj = 0;
   bh = 1/(0.13*(1+exp(-(y(39)+10.66)/11.1)));
   bj = 0.3*exp(-2.535e-7*y(39))/(1+exp(-0.1*(y(39)+32)));
else
   ah = 0.135*exp((80+y(39))/-6.8);
```

```
        bh = 3.56*exp(0.079*y(39))+3.1e5*exp(0.35*y(39));
        aj = (-1.2714e5*exp(0.2444*y(39))-3.474e-5*exp(-0.04391*y(39)))*(y(39)+37.78)/(1+exp(0.311*(y(39)+79.23)));
        bj = 0.1212*exp(-0.01052*y(39))/(1+exp(-0.1378*(y(39)+40.14)));
    end
    ydot(1) = am*(1-y(1))-bm*y(1);
    ydot(2) = ah*(1-y(2))-bh*y(2);
    ydot(3) = aj*(1-y(3))-bj*y(3);


    I_Na_junc = Fjunc*GNa*y(1)^3*y(2)*y(3)*(y(39)-ena_junc);
    I_Na_sl = Fsl*GNa*y(1)^3*y(2)*y(3)*(y(39)-ena_sl);

    % I_Na_junc= I_Na_junc1*(1-flag)+I_Na_junc2*flag;
    % I_Na_sl= I_Na_sl1*(1-flag)+I_Na_sl2*flag;
    I_Na = I_Na_junc+I_Na_sl;



    % I_nabk: Na Background Current
    I_nabk_junc = Fjunc*GNaB*(y(39)-ena_junc);
    I_nabk_sl = Fsl*GNaB*(y(39)-ena_sl);
    I_nabk = I_nabk_junc+I_nabk_sl;

    % I_nak: Na/K Pump Current
    sigma = (exp(Nao/67.3)-1)/7;
    fnak = 1/(1+0.1245*exp(-0.1*y(39)*FoRT)+0.0365*sigma*exp(-y(39)*FoRT));
    I_nak_junc = Fjunc*IbarNaK*fnak*Ko /(1+(KmNaip/y(32))^4) /(Ko+KmKo);
    I_nak_sl = Fsl*IbarNaK*Q10NaK*fnak*Ko /(1+(KmNaip/y(33))^4) /(Ko+KmKo);
    I_nak = I_nak_junc+I_nak_sl;

    % I_kr: Rapidly Activating K Current
    gkr = 0.03*sqrt(Ko/5.4);
    xrss = 1/(1+exp(-(y(39)+50)/7.5));
    tauxr = 1/(1.38e-3*(y(39)+7)/(1-exp(-0.123*(y(39)+7)))+6.1e-4*(y(39)+10)/(exp(0.145*(y(39)+10))-1));
    ydot(12) = (xrss-y(12))/tauxr;
    rkr = 1/(1+exp((y(39)+33)/22.4));
    I_kr = gkr*y(12)*rkr*(y(39)-ek);

    % I_ks: Slowly Activating K Current
    pcaks_junc = -log10(y(36))+3.0;
    pcaks_sl = -log10(y(37))+3.0;
    gks_junc = 0.4*(0.057 +0.19/(1+ exp((-7.2+pcaks_junc)/0.6)));
    gks_sl = 0.4*(0.057 +0.19/(1+ exp((-7.2+pcaks_sl)/0.6)));
    % gks_junc = 0.07*(0.057 +0.19/(1+ exp((-7.2+pcaks_junc)/0.6)));
    % gks_sl = 0.07*(0.057 +0.19/(1+ exp((-7.2+pcaks_sl)/0.6)));
    eks = (1/FoRT)*log((Ko+pNaK*Nao)/(y(35)+pNaK*y(34)));
    xsss = 1/(1+exp(-(y(39)+40)/16.7));
    tauxs = 1/(7.19e-5*(y(39)+30)/(1-exp(-0.148*(y(39)+30)))+1.31e-4*(y(39)+30)/(exp(0.0687*(y(39)+30))-1));
    ydot(13) = (xsss-y(13))/tauxs;
    I_ks_junc = Fjunc*gks_junc*y(13)^2*(y(39)-eks);
    I_ks_sl = Fsl*gks_sl*y(13)^2*(y(39)-eks);
    I_ks = I_ks_junc+I_ks_sl;

    %I_kp: Plateau K current
```

```
kp_kp = 1/(1+exp((7.488-y(39))/5.98)); %%%%///??
I_kp_junc = Fjunc*gkp*kp_kp*(y(39)-ek);
I_kp_sl = Fsl*gkp*kp_kp*(y(39)-ek);
I_kp = I_kp_junc+I_kp_sl;

%% I_to: Transient Outward K Current (slow and fast components)
xtoss = 1/(1+exp(-(y(39)+3.0)/15));
ytoss = 1/(1+exp((y(39)+33.5)/10));
rtoss = 1/(1+exp((y(39)+33.5)/10));
tauxtos = 9/(1+exp((y(39)+3.0)/15))+0.5;
tauytos = 3e3/(1+exp((y(39)+60.0)/10))+30;
%tauytos = 182/(1+exp((y(39)+33.5)/10))+1;
taurtos = 2.8e3/(1+exp((y(39)+60.0)/10))+220; %Fei changed here!! time-dependent gating variable
%taurtos =8085/(1+exp((y(39)+33.5)/10))+313;
ydot(8) = (xtoss-y(8))/tauxtos;
ydot(9) = (ytoss-y(9))/tauytos;
ydot(40)= (rtoss-y(40))/taurtos; %Fei changed here!! time-dependent gating variable
I_tos = GtoSlow*y(8)*(y(9)+0.5*y(40))*(y(39)-ek);    % [uA/uF]

tauxtof = 3.5*exp(-y(39)*y(39)/30/30)+1.5;
%tauxtof = 3.5*exp(-((y(39)+3)/30)^2)+1.5;
tauytof = 20.0/(1+exp((y(39)+33.5)/10))+20.0;
%tauytof = 20.0/(1+exp((y(39)+33.5)/10))+20.0;
ydot(10) = (xtoss-y(10))/tauxtof;
ydot(11) = (ytoss-y(11))/tauytof;
I_tof = GtoFast*y(10)*y(11)*(y(39)-ek);
I_to = I_tos + I_tof;

% I_ki: Time-Independent K Current
aki = 1.02/(1+exp(0.2385*(y(39)-ek-59.215)));
bki =(0.49124*exp(0.08032*(y(39)+5.476-ek)) + exp(0.06175*(y(39)-ek-594.31))) /(1 + exp(-
0.5143*(y(39)-ek+4.753)));
kiss = aki/(aki+bki);
I_ki = 0.9*sqrt(Ko/5.4)*kiss*(y(39)-ek);

% I_ClCa: Ca-activated Cl Current, I_Clbk: background Cl Current
I_ClCa_junc = Fjunc*GClCa/(1+KdClCa/y(36))*(y(39)-ecl);
I_ClCa_sl = Fsl*GClCa/(1+KdClCa/y(37))*(y(39)-ecl);
I_ClCa = I_ClCa_junc+I_ClCa_sl;
I_Clbk = GClB*(y(39)-ecl);

%% I_Ca: L-type Calcium Current
dss = 1/(1+exp(-(y(39)+23.5)/6.0));
taud = dss*(1-exp(-(y(39)+22.5)/6.0))/(0.035*(y(39)+22.5));
fss = 1/(1+exp((y(39)+35.06)/3.6))+0.6/(1+exp((50-y(39))/20));
tauf = 1/(0.0197*exp( -(0.0337*(y(39)+14.5))^2 )+0.02);
ydot(4) = (dss-y(4))/taud;
ydot(5) = (fss-y(5))/tauf;
ydot(6) = 1.7*y(36)*(1-y(6))-11.9e-3*y(6); % fCa_junc   koff!!!!!!!!
ydot(7) = 1.7*y(37)*(1-y(7))-11.9e-3*y(7); % fCa_sl
fcaCaMSL= 0.1/(1+(0.01/y(37)));
fcaCaj= 0.1/(1+(0.01/y(36)));
fcaCaMSL=0;
fcaCaj= 0;
%y(6)=0;
%y(7)=0;
```

```
        ibarca_j = pCa*4*(y(39)*Frdy*FoRT) * (0.341*y(36)*exp(2*y(39)*FoRT)-0.341*Cao)
/(exp(2*y(39)*FoRT)-1);
        ibarca_sl = pCa*4*(y(39)*Frdy*FoRT) * (0.341*y(37)*exp(2*y(39)*FoRT)-0.341*Cao)
/(exp(2*y(39)*FoRT)-1);
        ibark = pK*(y(39)*Frdy*FoRT)*(0.75*y(35)*exp(y(39)*FoRT)-0.75*Ko) /(exp(y(39)*FoRT)-1);
        ibarna_j = pNa*(y(39)*Frdy*FoRT) *(0.75*y(32)*exp(y(39)*FoRT)-0.75*Nao) /(exp(y(39)*FoRT)-1);
        ibarna_sl = pNa*(y(39)*Frdy*FoRT) *(0.75*y(33)*exp(y(39)*FoRT)-0.75*Nao) /(exp(y(39)*FoRT)-1);
        I_Ca_junc = (Fjunc_CaL*ibarca_j*y(4)*y(5)*((1-y(6))+fcaCaj)*Q10CaL^Qpow)*0.45*1;
        I_Ca_sl = (Fsl_CaL*ibarca_sl*y(4)*y(5)*((1-y(7))+fcaCaMSL)*Q10CaL^Qpow)*0.45*1;
        I_Ca = I_Ca_junc+I_Ca_sl;
        I_CaK = (ibark*y(4)*y(5)*(Fjunc_CaL*(fcaCaj+(1-y(6)))+Fsl_CaL*(fcaCaMSL+(1-
y(7))))*Q10CaL^Qpow)*0.45*1;
        I_CaNa_junc = (Fjunc_CaL*ibarna_j*y(4)*y(5)*((1-y(6))+fcaCaj)*Q10CaL^Qpow)*0.45*1;
        I_CaNa_sl = (Fsl_CaL*ibarna_sl*y(4)*y(5)*((1-y(7))+fcaCaMSL)*Q10CaL^Qpow)*.45*1;
        I_CaNa = I_CaNa_junc+I_CaNa_sl;
        I_Catot = I_Ca+I_CaK+I_CaNa;

        % I_ncx: Na/Ca Exchanger flux
        Ka_junc = 1/(1+(Kdact/y(36))^3);
        Ka_sl = 1/(1+(Kdact/y(37))^3);
        s1_junc = exp(nu*y(39)*FoRT)*y(32)^3*Cao;
        s1_sl = exp(nu*y(39)*FoRT)*y(33)^3*Cao;
        s2_junc = exp((nu-1)*y(39)*FoRT)*Nao^3*y(36);
        s3_junc = KmCai*Nao^3*(1+(y(32)/KmNai)^3) +
KmNao^3*y(36)*(1+y(36)/KmCai)+KmCao*y(32)^3+y(32)^3*Cao+Nao^3*y(36);
        s2_sl = exp((nu-1)*y(39)*FoRT)*Nao^3*y(37);
        s3_sl = KmCai*Nao^3*(1+(y(33)/KmNai)^3) +
KmNao^3*y(37)*(1+y(37)/KmCai)+KmCao*y(33)^3+y(33)^3*Cao+Nao^3*y(37);
        I_ncx_junc = Fjunc*IbarNCX*Q10NCX^Qpow*Ka_junc*(s1_junc-s2_junc)/s3_junc/(1+ksat*exp((nu-
1)*y(39)*FoRT));
        I_ncx_sl = Fsl*IbarNCX*Q10NCX^Qpow*Ka_sl*(s1_sl-s2_sl)/s3_sl/(1+ksat*exp((nu-1)*y(39)*FoRT));
        I_ncx = I_ncx_junc+I_ncx_sl;

        % I_pca: Sarcolemmal Ca Pump Current
        I_pca_junc = Fjunc*Q10SLCaP^Qpow*IbarSLCaP*y(36)^1.6/(KmPCa^1.6+y(36)^1.6);
        I_pca_sl = Fsl*Q10SLCaP^Qpow*IbarSLCaP*y(37)^1.6/(KmPCa^1.6+y(37)^1.6);
        I_pca = I_pca_junc+I_pca_sl;

        % I_cabk: Ca Background Current
        I_cabk_junc = Fjunc*GCaB*(y(39)-eca_junc);
        I_cabk_sl = Fsl*GCaB*(y(39)-eca_sl);
        I_cabk = I_cabk_junc+I_cabk_sl;

        %% SR fluxes: Calcium Release, SR Ca pump, SR Ca leak
        MaxSR = 15; MinSR = 1;
        kCaSR = MaxSR - (MaxSR-MinSR)/(1+(ec50SR/y(31))^2.5);
        koSRCa = koCa/kCaSR;
        kiSRCa = kiCa*kCaSR;
        RI = 1-y(14)-y(15)-y(16);
        ydot(14) = (kim*RI-kiSRCa*y(36)*y(14))-(koSRCa*y(36)^2*y(14)-kom*y(15));   % R
        ydot(15) = (koSRCa*y(36)^2*y(14)-kom*y(15))-(kiSRCa*y(36)*y(15)-kim*y(16));% O
        ydot(16) = (kiSRCa*y(36)*y(15)-kim*y(16))-(kom*y(16)-koSRCa*y(36)^2*RI);   % I
        J_SRCarel = ks*y(15)*(y(31)-y(36));          % [mM/ms]

        J_serca = Q10SRCaP^Qpow*Vmax_SRCaP*((y(38)/Kmf)^hillSRCaP-(y(31)/Kmr)^hillSRCaP)...
           /(1+(y(38)/Kmf)^hillSRCaP+(y(31)/Kmr)^hillSRCaP);
```

```
J_SRleak = 5.348e-6*(y(31)-y(36));          %   [mM/ms]

%% Sodium and Calcium Buffering
ydot(17) = kon_na*y(32)*(Bmax_Naj-y(17))-koff_na*y(17);        % NaBj      [mM/ms]
ydot(18) = kon_na*y(33)*(Bmax_Nasl-y(18))-koff_na*y(18);       % NaBsl     [mM/ms]

% Cytosolic Ca Buffers
% ydot(19) = nc*(ydot(41)+ydot(42)+ydot(43));
ydot(19) = kon_tncl*y(38)*(Bmax_TnClow-y(19))-koff_tncl*y(19);           % TnCL      [mM/ms]
ydot(20) = kon_tnchca*y(38)*(Bmax_TnChigh-y(20)-y(21))-koff_tnchca*y(20); % TnCHc     [mM/ms]
ydot(21) = kon_tnchmg*Mgi*(Bmax_TnChigh-y(20)-y(21))-koff_tnchmg*y(21);   % TnCHm     [mM/ms]
ydot(22) = kon_cam*y(38)*(Bmax_CaM-y(22))-koff_cam*y(22);                 % CaM       [mM/ms]
ydot(23) = kon_myoca*y(38)*(Bmax_myosin-y(23)-y(24))-koff_myoca*y(23);    % Myosin_ca [mM/ms]
ydot(24)  =  kon_myomg*Mgi*(Bmax_myosin-y(23)-y(24))-koff_myomg*y(24);            %  Myosin_mg
[mM/ms]
ydot(25) = kon_sr*y(38)*(Bmax_SR-y(25))-koff_sr*y(25);                    % SRB       [mM/ms]
J_CaB_cytosol = sum(ydot(19:25));

% Junctional and SL Ca Buffers
ydot(26) = kon_sll*y(36)*(Bmax_SLlowj-y(26))-koff_sll*y(26);       % SLLj      [mM/ms]
ydot(27) = kon_sll*y(37)*(Bmax_SLlowsl-y(27))-koff_sll*y(27);      % SLLsl     [mM/ms]
ydot(28) = kon_slh*y(36)*(Bmax_SLhighj-y(28))-koff_slh*y(28);      % SLHj      [mM/ms]
ydot(29) = kon_slh*y(37)*(Bmax_SLhighsl-y(29))-koff_slh*y(29);     % SLHsl     [mM/ms]
J_CaB_junction = ydot(26)+ydot(28);
J_CaB_sl = ydot(27)+ydot(29);

%% Ion concentrations
% SR Ca Concentrations
ydot(30) = kon_csqn*y(31)*(Bmax_Csqn-y(30))-koff_csqn*y(30);       % Csqn      [mM/ms]
ydot(31) = J_serca-(J_SRleak*Vmyo/Vsr+J_SRCarel)-ydot(30);         % Ca_sr     [mM/ms] %Ratio 3 leak
current

% Sodium Concentrations
I_Na_tot_junc = I_Na_junc+I_nabk_junc+3*I_ncx_junc+3*I_nak_junc+I_CaNa_junc;   % [uA/uF]
I_Na_tot_sl = I_Na_sl+I_nabk_sl+3*I_ncx_sl+3*I_nak_sl+I_CaNa_sl;   % [uA/uF]

ydot(32) = -I_Na_tot_junc*Cmem/(Vjunc*Frdy)+J_na_juncsl/Vjunc*(y(33)-y(32))-ydot(17);
ydot(33) = -I_Na_tot_sl*Cmem/(Vsl*Frdy)+J_na_juncsl/Vsl*(y(32)-y(33))...
   +J_na_slmyo/Vsl*(y(34)-y(33))-ydot(18);
%ydot(32) = 0;
%ydot(33) = 0;
ydot(34) = J_na_slmyo/Vmyo*(y(33)-y(34));            % [mM/msec]
%ydot(34)=0;

% Potassium Concentration
I_K_tot = I_to+I_kr+I_ks+I_ki-2*I_nak+I_CaK+I_kp;     % [uA/uF]
% ydot(35) = 0; %-I_K_tot*Cmem/(Vmyo*Frdy);          % [mM/msec]
ydot(35) =0; % -I_K_tot*Cmem/(Vmyo*Frdy);

% Calcium Concentrations
I_Ca_tot_junc = I_Ca_junc+I_cabk_junc+I_pca_junc-2*I_ncx_junc;                 % [uA/uF]
I_Ca_tot_sl = I_Ca_sl+I_cabk_sl+I_pca_sl-2*I_ncx_sl;           % [uA/uF]
ydot(36) = -I_Ca_tot_junc*Cmem/(Vjunc*2*Frdy)+J_ca_juncsl/Vjunc*(y(37)-y(36))...
   -J_CaB_junction+(J_SRCarel)*Vsr/Vjunc+J_SRleak*Vmyo/Vjunc;  % Ca_j
ydot(37) = -I_Ca_tot_sl*Cmem/(Vsl*2*Frdy)+J_ca_juncsl/Vsl*(y(36)-y(37))...
   + J_ca_slmyo/Vsl*(y(38)-y(37))-J_CaB_sl;   % Ca_sl
```

```
% ydot(38) = -J_serca*Vsr/Vmyo-J_CaB_cytosol;%+J_ca_slmyo/Vmyo*(y(37)-y(38));    % [mM/msec]
ydot(38) = -J_serca*Vsr/Vmyo-J_CaB_cytosol +J_ca_slmyo/Vmyo*(y(37)-y(38));
%% Membrane Potential
I_Na_tot = I_Na_tot_junc + I_Na_tot_sl;          % [uA/uF]
I_Cl_tot = I_ClCa+I_Clbk;                        % [uA/uF]
I_Ca_tot = I_Ca_tot_junc+I_Ca_tot_sl;
I_tot = I_Na_tot+I_Cl_tot+I_Ca_tot+I_K_tot;
if(mod(t,2000)<1)
   I_app =-40;
else
   I_app =0;
end
ydot(39) = -(I_tot+I_app);
vmax = ydot(39);
end
```

APPENDIX E

C++ CODE FOR MAHAJAN MODEL

CELL.CPP

```
#ifndef ___CELL
#define ___CELL
#include "cell.h"


CCell::CCell(void) : y(new double[N]),
        xm(y[0]), xh(y[1]), xj(y[2]), xr(y[3]),
        xs1(y[4]), xs2(y[5]), xtos(y[6]), ytos(y[7]),
        v(y[8]), cp(y[9]), cs(y[10]), ci(y[11]),
        cj(y[12]), cjp(y[13]), xir(y[14]), c1(y[15]),
        c2(y[16]), xi1ca(y[17]), xi1ba(y[18]), xi2ca(y[19]),
        xi2ba(y[20]), xnai(y[21]), xtof(y[22]), ytof(y[23]),
        tropi(y[24]), trops(y[25])
{
// initial conditions
        xm=0.001145222753;// sodium m-gate
        xh=0.9898351676;// sodium h-gate
        xj=0.9930817518;// soiumj-gate

        xr=0.008709989976;// ikr gate variable
        xs1=0.08433669901;// iks gate variable
        xs2=0.1412866149;// iks gate varaible

        xtos=0.003757746357;// ito slow activation
        ytos=0.1553336368;// ito slow inactivation

        v=-86.79545769; // voltage
```

```
        cp=1.682601371;// averaged dyadic space con.
        cs=0.3205609256;// averaged submembrane conc.
        ci=0.3863687451;// myoplasm conc.

        cj=107.0388739;// NSR load
        cjp=95.76256179;// average JSR load

        xir=0.006462569526;// SR current flux

        // Markov gate variables

        c1=1.925580885e-05;// C1
        c2=0.9535940241;// C2
        xi1ca=0.007052299702;// I1_Ca
        xi1ba=3.629261123e-05;// I1_Ba
        xi2ca=0.02316349806;// I2_Ca
        xi2ba=0.01613268649;// I2_Ba

        xnai=14.01807252;// internal Na conc.

        xtof=0.003737842131;// ito fast activation
        ytof=0.9823715315;// ito slow inactivation

        tropi=29.64807803;// time dependent buffers in myplasm (troponin)
        trops=26.37726416;// time dependent buffers in submembrane (troponin)

        hpde=0.1;
        vold = v;
        jparam=1;

#ifdef ___USE_VAR_FOR_CONST
        xnao=136.0;//mM              external Na
        xki=140.0;// mM  internal K
        xko=5.40;//mM    external K
        cao=1.8;// mM     external Ca

        gca=182;// ica conductance
        gtos=0.04;// ito slow conductance
        gtof=0.11;// ito fast conductance
        gnaca=0.84;// exchanger strength
        gkr=0.0125;// Ikr conductance
        gks=0.32;
        gkix=0.3;// Ik1 conductance
        gnak=1.5;
        vup=0.4;//0.3;// uptake strength
        taus=4.0;// diffusional delay (ms)
        gna=12.0;// sodium conductance (mS/micro F)
        taur=30.0;// spark lifetime (ms)
        taua=100.0;// NSR-JSR diffusional delay (ms)
```

```
	av=11.3;
	cstar=90.0;
#endif
}
CCell::~CCell()
{
	delete[] y;
}
void CCell::Prepare(double BCL, int Iter)
{
	if (Iter==0)
	{
		double dciold=0;
		double dciold2=0;
		bool first=false;
		int Tn=BCL*10000/hpde, BCLn=BCL/hpde, Durn=stimduration/hpde;
		for (int tn=0;tn<Tn;tn++)
		{
			double t=tn*hpde;
			if (tn%BCLn < Durn)
			{
				if (first)
				{
					if (fabs(ci-dciold2)<0.00001 && t>BCL*300)
					{
						break;
					}
					dciold2=dciold;
					dciold=ci;
					first=false;
				}
				Pace(stim);
			}
			else
			{
				first=true;
				Pace();
			}
		}
	}
	else
	{
		int Tn=BCL*Iter/hpde, BCLn=BCL/hpde, Durn=stimduration/hpde;
		for (int tn=0;tn<Tn;tn++)
		{
			if (tn%BCLn < Durn)
				Pace(stim);
			else
				Pace();
```

```
		}
	}
}
CCell& CCell::operator=(const CCell& cell)
{
	if (&cell!=this)
	{
		for (int i=0;i<N;i++)
		{
			y[i]=cell.y[i];
		}
		jparam=cell.jparam;
		vold=cell.vold;
		hpde=cell.hpde;
	#ifdef ___USE_VAR_FOR_CONST
		xnao=cell.xnao;
		xki=cell.xki;
		xko=cell.xko;
		cao=cell.cao;

		gca=cell.gca;
		gtos=cell.gtos;
		gtof=cell.gtof;
		gnaca=cell.gnaca;
		gkr=cell.gkr;
		gks=cell.gks;
		gkix=cell.gkix;
		gnak=cell.gnak;
		vup=cell.vup;
		taus=cell.taus;
		gna=cell.gna;
		taur=cell.taur;
		taua=cell.taua;
		av=cell.av;
		cstar=cell.cstar;
	#endif
	}
	return(*this);
}
void CCell::ClampAP(double t, double T, double APD)
{
	const double Vmin=-80;//-80mV
	const double Vmax=30;//30mV
	double clampv;
	if (APD==0)
	{
		const double a=2.0/3.0*1000;
		double x=a/(a+T);
		int m=(int)(t/T);
```

```
                if (m*T+x*T>t)
                {
                        clampv=Vmin+(Vmax-Vmin)*sqrt(1-((t-m*T)/x/T)*((t-m*T)/x/T));
                }
                else
                {
                        clampv=Vmin;
                }
        }
        else
        {
                double x=APD/T;
                int m=(int)(t/T);
                if (m*T+x*T>t)
                {
                        clampv=Vmin+(Vmax-Vmin)*sqrt(1-((t-m*T)/x/T)*((t-m*T)/x/T));
                }
                else
                {
                        clampv=Vmin;
                }
        }

        double dv=(vold-v)/hpde;
        vold=v;
        double Itotal;
        if(fabs(dv)>25.0)// then finer time step when dv/dt large
        {
                hode=hpde/10;
                for (int iii=0;iii<10;iii++)
                {
                        v=clampv;
                        Itotal=PaceX(0);
                }
        }
        else
        {
                hode=hpde;
                v=clampv;
                Itotal=PaceX(0);
        }
}
double CCell::Pace(double Istim)
{
// -------------time step adjustment -----------------------
        double dv=(vold-v)/hpde;
        vold=v;
        double Itotal;
        if(fabs(dv)>25.0)// then finer time step when dv/dt large
```

```
	{
		hode=hpde/10;
		for (int iii=0;iii<10;iii++)
		{
			Itotal=PaceX(Istim);
		}
	}
	else
	{
		hode=hpde;
		Itotal=PaceX(Istim);
	}
	return Itotal;
}
double CCell::PaceVClamp(double clampv)
{
// -------------time step adjustment ------------------------
	double dv=(vold-v)/hpde;
	vold=v;
	double Itotal;
	if(fabs(dv)>25.0)// then finer time step when dv/dt large
	{
		hode=hpde/10;
		for (int iii=0;iii<10;iii++)
		{
			v=clampv;
			Itotal=PaceX(0);
		}
	}
	else
	{
		hode=hpde;
		v=clampv;
		Itotal=PaceX(0);
	}
	return Itotal;
}

double CCell::PaceX(double Istim)
{
	double xik1=comp_ik1();
	double xito=comp_ito();//itos and itof
	double xinak=comp_inak();
	double csm=cs/1000.0;// convert micro M to mM
	double xinacaq=comp_inaca(csm);
//----------- Equations for Ca cycling -------------------------
	double xdif=(cs-ci)/taus;//diffusion from submembrane to myoplasm
	// Troponin kinetics
	const double xkon=0.0327;
```

```
        const double xkoff=0.0196;
        const double btrop=70.0;
        double xbi=xkon*ci*(btrop-tropi)-xkoff*tropi;
        double xbs=xkon*cs*(btrop-trops)-xkoff*trops;

        double xiup=comp_iup();
        double xileak=comp_ileak();

        double po=comp_icalpo();
        double rxa=comp_rxa(csm);
        double xicaq=gca*po*rxa;// Ca current in micro M/ms

        double dcs=comp_inst_buffer(cs)*(50.0*(xir-xdif-xicaq+xinacaq)-xbs);
        double dci=comp_inst_buffer(ci)*(xdif-xiup+xileak-xbi);
        double dcj=-xir+xiup-xileak;// SR load dynamics
        double dcjp=(cj-cjp)/taua;// NSR-JSR relaxation dynamics
        double Qr=comp_Q();
        double dir=comp_dir(po, Qr, rxa, dcj);
        double dcp=comp_dcp(po, Qr, rxa);

        double xina=comp_ina();
        double xikr=comp_ikr();
        double xiks=comp_iks();

        cp+=dcp*hode;
        cs+=dcs*hode;
        ci+=dci*hode;
        cj+=dcj*hode;
        xir+=dir*hode;
        cjp+=dcjp*hode;

        tropi+=xbi*hode;
        trops+=xbs*hode;

//-------convert ion flow to current---------
        const double wca=8.0;//conversion factor between micro molar/ms to micro amps/ micro farads
        double xinaca=wca*xinacaq;
        double xica=2.0*wca*xicaq;
//--------sodium dynamics -------------------------
        const double xrr=(1.0/wca)/1000.0;// note: sodium is in m molar so need to divide by 1000
        xnai+=(-xrr*(xina+3.0*xinak+3.0*xinaca))*hode;
// -------- dV/dt -----------------------------------
        double Itotal=(-(xina+xik1+xikr+xiks+xito+xinaca+xica+xinak)+ Istim);
        v+=Itotal*hode;
        #ifdef ___REC_CURRENTS
        _inaca=xinaca;_ica=xica;_iks=xiks;_ikr=xikr;_ik1=xik1;_ina=xina;_inak=xinak;_iup=xiup;
        #endif
        return Itotal;
}
```

```
//-----------          sodium current following Hund-Rudy --------------------
double CCell::comp_ina(void)
{
        double ena = (1.0/frt)*log(xnao/xnai);
        double am;
        if (fabs(v+47.13)<0.001/0.1)
                am=3.2;
        else
                am = 0.32*(v+47.13)/(1.0-exp(-0.1*(v+47.13)));
        double bm = 0.08*exp(-v/11.0);
        double ah,bh,aj,bj;
        if(v<(-40.0))
        {
                 ah=0.135*exp((80.0+v)/(-6.8));
                 bh=3.56*exp(0.079*v)+310000.0*exp(0.35*v);
                 aj=((-127140.0*exp(0.2444*v)-0.00003474*exp(-
0.04391*v))*(v+37.78))/(1.0+exp(0.311*(v+79.23)));
                 bj=(0.1212*exp(-0.01052*v))/(1.0+exp(-0.1378*(v+40.14)));
        }
        else
        {
                 ah=0.0;
                 bh=1.0/(0.13*(1.0+exp((v+10.66)/(-11.1))));
                 aj=0.0;
                 bj=(0.3*exp(-0.0000002535*v))/(1.0+exp(-0.1*(v+32.0)));
        }

        double tauh=1.0/(ah+bh);
        double tauj=1.0/(aj+bj)*jparam;
        double taum=1.0/(am+bm);
        double xina= gna*xh*xj*xm*xm*xm*(v-ena);

        xh = ah/(ah+bh)-((ah/(ah+bh))-xh)*exp(-hode/tauh);
        xj = aj/(aj+bj)-((aj/(aj+bj))-xj)*exp(-hode/tauj);
        xm = am/(am+bm)-((am/(am+bm))-xm)*exp(-hode/taum);
        return xina;
}
//---------- Ikr following Shannon------------------
double CCell::comp_ikr(void)
{
        #ifdef ___USE_VAR_FOR_CONST
        double ek = (1.0/frt)*log(xko/xki);// K reversal potential
        #endif
        const double gss=sqrt(xko/5.4);
        double xkrv1;
        if (fabs(v+7.0)<0.001/0.123)
                xkrv1=0.00138/0.123;
        else
                xkrv1=0.00138*(v+7.0)/( 1.-exp(-0.123*(v+7.0)));
```

```
	double xkrv2;
	if (fabs(v+10.0)<0.001/0.145)
		xkrv2=0.00061/0.145;
	else
		xkrv2=0.00061*(v+10.0)/(exp( 0.145*(v+10.0))-1.0);
	double taukr=1.0/(xkrv1+xkrv2);
	double xkrinf=1.0/(1.0+exp(-(v+50.0)/7.5));
	double rg=1.0/(1.0+exp((v+33.0)/22.4));
	double xikr=gkr*gss*xr*rg*(v-ek);
	xr=xkrinf-(xkrinf-xr)*exp(-hode/taukr);
	return xikr;
}
// ----- Iks modified from Shannon, with new Ca dependence------------
double CCell::comp_iks(void)
{
	const double prnak=0.018330;
	double eks=(1.0/frt)*log((xko+prnak*xnao)/(xki+prnak*xnai));
	double xs1ss=1.0/(1.0+exp(-(v-1.50)/16.70));
	double xs2ss=xs1ss;
	double tauxs1;
	if (fabs(v+30.0)<0.001/0.0687)
		tauxs1=1/(0.0000719/0.148+0.000131/0.0687);
	else
		tauxs1=1.0/(0.0000719*(v+30.0)/(1.0-exp(-
0.148*(v+30.0)))+0.000131*(v+30.0)/(exp(0.0687*(v+30.0))-1.0));
	double tauxs2=4*tauxs1;
	double gksx=0.433*(1+0.8/(1+pow((0.5/ci),3)));
	double xiks=gks*gksx*xs1*xs2*(v-eks);
	xs1=xs1ss-(xs1ss-xs1)*exp(double(-hode/tauxs1));
	xs2=xs2ss-(xs2ss-xs2)*exp(double(-hode/tauxs2));
	return xiks;
}
//------Ik1 following Luo-Rudy formulation (from Shannon model) ------
double CCell::comp_ik1(void)
{
	#ifdef ___USE_VAR_FOR_CONST
	double ek = (1.0/frt)*log(xko/xki);// K reversal potential
	#endif
	const double gki=(sqrt(xko/5.4));
	double aki=1.02/(1.0+exp(0.2385*(v-ek-59.215)));
	double bki=(0.49124*exp(0.08032*(v-ek+5.476))+exp(0.061750*(v-ek-594.31)))/(1.0+exp(-0.5143*(v-
ek+4.753)));
	double xkin=aki/(aki+bki);
	double xik1=gkix*gki*xkin*(v-ek);
	return xik1;
}
//------- Ito slow following Shannon et. al. 2005 -----------
//------- Ito fast following Shannon et. al. 2005 -----------
double CCell::comp_ito(void)
```

```
{
	#ifdef ___USE_VAR_FOR_CONST
	double ek = (1.0/frt)*log(xko/xki);// K reversal potential
	#endif
	double rt1=-(v+3.0)/15.0;
	double rt2=(v+33.5)/10.0;
	double rt3=(v+60.0)/10.0;
	double xtos_inf=1.0/(1.0+exp(rt1));
	double ytos_inf=1.0/(1.0+exp(rt2));
	double rs_inf=1.0/(1.0+exp(rt2));
	double txs=9.0/(1.0+exp(-rt1)) + 0.5;
	double tys=3000.0/(1.0+exp(rt3)) + 30.0;
	double xitos=gtos*xtos*(ytos+0.5*rs_inf)*(v-ek);// ito slow
	xtos = xtos_inf-(xtos_inf-xtos)*exp(-hode/txs);
	ytos = ytos_inf-(ytos_inf-ytos)*exp(-hode/tys);

	double xtof_inf=xtos_inf;
	double ytof_inf=ytos_inf;
	double rt4=-(v/30.0)*(v/30.0);
	double rt5=(v+33.5)/10.0;
	double txf=3.5*exp(rt4)+1.5;
	double tyf=20.0/(1.0+exp(rt5))+20.0;
	double xitof=gtof*xtof*ytof*(v-ek);// ito fast
	xtof = xtof_inf-(xtof_inf-xtof)*exp(-hode/txf);
	ytof = ytof_inf-(ytof_inf-ytof)*exp(-hode/tyf);
	#ifdef ___REC_CURRENTS
	_itof=xitof;_itos=xitos;
	#endif
	return xitos+xitof;
}
// -------Inak (sodium-potassium exchanger) following Shannon ----------
double CCell::comp_inak(void)
{
	const double xkmko=1.5;  //these are Inak constants adjusted to fit
                                                        //the experimentally measured dynamic restitution
curve
	const double xkmnai=12.0;
	const double sigma = (exp(xnao/67.3)-1.0)/7.0;
	double fnak = 1.0/(1+0.1245*exp(-0.1*v*frt)+0.0365*sigma*exp(-v*frt));
	double xinak = gnak*fnak*(1./(1.+(xkmnai/xnai)))*xko/(xko+xkmko);
	return xinak;
}
// --- Inaca (sodium-calcium exchange) following Shannon and Hund-Rudy------
//	Note: all concentrations are in mM
double CCell::comp_inaca(double csm)
{
	double zw3=pow(xnai,3)*cao*exp(v*0.35*frt)-pow(xnao,3)*csm*exp(v*(0.35-1.)*frt);
	double zw4=1.0+0.2*exp(v*(0.35-1.0)*frt);
	const double xkdna=0.3;// micro M
```

```
	double aloss=1.0/(1.0+pow((xkdna/cs),3));
	const double xmcao=1.3;
	const double xmnao=87.5;
	const double xmnai=12.3;
	const double xmcai=0.0036;
	double yz1=xmcao*pow(xnai,3)+pow(xmnao,3)*csm;
	double yz2=pow(xmnai,3)*cao*(1.0+csm/xmcai);
	double yz3=xmcai*pow(xnao,3)*(1.0+pow((xnai/xmnai),3));
	double yz4=pow(xnai,3)*cao+pow(xnao,3)*csm;
	double zw8=yz1+yz2+yz3+yz4;
	double xinacaq=gnaca*aloss*zw3/(zw4*zw8);
	return xinacaq;
}
//	compute driving force
double CCell::comp_rxa(double csm)
{
	const double pca=0.00054;
	double za=v*2.0*frt;
	double factor1=4.0*pca*xf*xf/(xxr*temp);
	double factor=v*factor1;
	double rxa;
	if(fabs(za)<0.001)
	{
		rxa=factor1*(csm*exp(za)-0.341*(cao))/(2.0*frt);
	}
	else
	{
		rxa=factor*(csm*exp(za)-0.341*(cao))/(exp(za)-1.0);
	}
	return rxa;
}
// ------ Markovian Ca current --------------------------------
//	Markov model:All parameters have been fitted directly to
//	experimental current traces using a multidimensional current fitting
//	routine.
double CCell::comp_icalpo(void)
{
	const double vth=0.0;
	const double s6=8.0;

	const double taupo=1.0;
	double poinf=1.0/(1.0+exp(-(v-vth)/s6));

	double alpha=poinf/taupo;
	double beta=(1.0-poinf)/taupo;

	const double r1=0.30;
	const double r2=3.0;
```

```
        const double cat=3.0;
        double fca=1.0/(1.0+pow(double(cat/cp),3));

        double s1=0.0182688*fca;

        const double s1t=0.00195;

        double xk1=0.024168*fca;
        const double xk2=1.03615e-4;

        const double xk1t=0.00413;
        const double xk2t=0.00224;

        double s2=s1*(r1/r2)*(xk2/xk1);
        const double s2t=s1t*(r1/r2)*(xk2t/xk1t);

        const double vx=-40;
        const double sx=3.0;
        double poi=1.0/(1.0+exp(-(v-vx)/sx));
        const double tau3=3.0;

        double xk3=(1.0-poi)/tau3;
        double xk3t=xk3;

        const double vy=-40.0;
        const double sy=4.0;
        double prv=1.0-1.0/(1.0+exp(-(v-vy)/sy));

        double recov=10.0+4954.0*exp(v/15.6);

        const double tca=78.0329;
        const double cpt=6.09365;
        double tau_ca=tca/(1.0+pow((cp/cpt),4));

#ifdef ___FORTHREED
        double tauca=(recov-tau_ca)*prv+tau_ca+1;
#else
        double tauca=(recov-tau_ca)*prv+tau_ca;
#endif
        double tauba=(recov-450.0)*prv+450.0;

        const double vyr=-40.0;
        const double syr=11.32;
        double poix=1.0/(1.0+exp(-(v-vyr)/syr));

        double xk6=fca*poix/tauca;
        double xk5=(1.0-poix)/tauca;

        double xk6t=poix/tauba;
```

```
	double xk5t=(1.0-poix)/tauba;

	double xk4=xk3*(alpha/beta)*(xk1/xk2)*(xk5/xk6);
	double xk4t=xk3t*(alpha/beta)*(xk1t/xk2t)*(xk5t/xk6t);

	double po=1.0-xi1ca-xi2ca-xi1ba-xi2ba-c1-c2;

	double dc2= beta*c1+xk5*xi2ca+xk5t*xi2ba-(xk6+xk6t+alpha)*c2;
	double dc1=alpha*c2+xk2*xi1ca+xk2t*xi1ba+r2*po-(beta+r1+xk1t+xk1)*c1;

	double dxi1ca=xk1*c1+xk4*xi2ca+s1*po-(xk3+xk2+s2)*xi1ca;
	double dxi2ca=xk3*xi1ca+xk6*c2-(xk5+xk4)*xi2ca;

	double dxi1ba=xk1t*c1+xk4t*xi2ba+s1t*po-(xk3t+xk2t+s2t)*xi1ba;
	double dxi2ba=xk3t*xi1ba+xk6t*c2-(xk5t+xk4t)*xi2ba;

	c1+=dc1*hode;
	c2+=dc2*hode;
	xi1ca+=dxi1ca*hode;
	xi1ba+=dxi1ba*hode;
	xi2ca+=dxi2ca*hode;
	xi2ba+=dxi2ba*hode;
	return po;
}
//----- SERCA2a uptake current ------------------------------------
double CCell::comp_iup(void)
{
	const double xup=0.5;// uptake threshold
	double xiup=vup*ci*ci/(ci*ci + xup*xup);
	return xiup;
}
// ---------leak from the SR--------------------------
double CCell::comp_ileak(void)
{
	const double gleak=0.00002069;
	return gleak*(cj*cj/(cj*cj+50.0*50.0))*(cj*16.667-ci);//vsr/vcell=0.06
}
// ---------- buffer dynamics in the myoplasm -----------------------
//buffering to calmodulin and SR are instantaneous, while buffering to
//Troponin C is time dependent.These are important to have reasonable
//Ca transient.Note: we have buffering in the submembrane space and
//the myoplasm.
double CCell::comp_inst_buffer(double c)
{
	const double bcal=24.0;
	const double xkcal=7.0;
	const double srmax=47.0;
	const double srkd=0.6;
	const double bmem=15.0;
```

```
	const double kmem=0.3;
	const double bsar=42.0;
	const double ksar=13.0;
	double bpx=bcal*xkcal/((xkcal+c)*(xkcal+c));
	double spx=srmax*srkd/((srkd+c)*(srkd+c));
	double mempx=bmem*kmem/((kmem+c)*(kmem+c));
	double sarpx=bsar*ksar/((ksar+c)*(ksar+c));
	return 1.0/(1.0+bpx+spx+mempx+sarpx);
}
// --------- release-load functional dependence ----------------
double CCell::comp_Q(void)
{
	double bv=(cstar-50.)-av*cstar;
	double Qr;
	if (cjp<50)
	{
		Qr=0.0;
	}
	else if (cjp>50.0 && cjp<cstar)
	{
		Qr=cjp-50.0;
	}
	else
	{
		Qr=av*cjp+bv;
	}
	return cj*Qr/cstar;
}
double CCell::comp_dir(double po, double Qr, double rxa, double dcj)
{
	const double ay=0.05;
	double sparkV=exp(-ay*(v+30))/(1.+exp(-ay*(v+30)));
	const double g=2.58079;
	double spark_rate=g*po*fabs(rxa)*sparkV;
	return spark_rate*Qr-xir*(1-taur*dcj/cj)/taur;
}
// ----------- dyadic junction dynamics ------------------------
double CCell::comp_dcp(double po, double Qr, double rxa)
{
	const double grel=26841.8;// m mol/(cm C)
	const double ax=0.3576;
	const double gdyad=9000.0;// m mol/(cm C)
	double ssr=exp(-ax*(v+30))/(1.0+exp(-ax*(v+30)));
	double gain=po*Qr*fabs(rxa)*ssr;
	double xirp=grel*gain;

	double xicap=po*gdyad*fabs(rxa);
	const double taups=0.5;
	return xirp+xicap-(cp-cs)/taups;
```

```
}
#endif /* ___CELL */
```

CELL.H

```
#ifndef ___CELL_H
#define ___CELL_H

/* ---------------- UCLA Model ver 1.00 ---------------- **
*
* Contact Information
*
* Departments of Medicine (Cardiology)
* David Geffen School of Medicine at UCLA
*
* Daisuke Sato                  dasato (at) mednet.ucla.edu
* Yohannes Shiferaw  yshiferaw (at) csun.edu
* James N Weiss  JWeiss (at) mednet.ucla.edu
*
** ---------------- ------------------- ---------------- */


// #define ___REC_CURRENTS //record currents (more memory)
// #define ___USE_VAR_FOR_CONST //use variables for Gto Gks Gkr etc. instead of constants (more memory)

#include <iostream>
using namespace std;
#define _USE_MATH_DEFINES
#include <cmath>

class CCell{
private:
        double jparam;//tauj*jparam
        double PaceX(double stim=0);
        static const int N=26;
        static const double Vc;
        static const double stim;
        static const double stimduration;
        static const double temp;// temperature (K)
        static const double xxr;//
        static const double xf;// Faraday's constant
        static const double frt;

        #ifndef ___USE_VAR_FOR_CONST
        static const double xnao;//mM         external Na
        static const double xki;// mM         internal K
        static const double xko;// mM         external K
```

```
        static const double cao;// mM          external Ca
        static const double ek;

        static const double gca;// ica conductance
        static const double gtos;// ito slow conductance
        static const double gtof;//ito fast conductance
        static const double gnaca;// exchanger strength
        static const double gks;
        static const double gkr;
        static const double vup;// uptake strength
        static const double gna;// sodium conductance (mS/micro F)
        static const double gkix;// Ik1 conductance
        static const double gnak;

        static const double taur;// spark lifetime (ms)
        static const double taus;// diffusional delay (ms)
        static const double taua;// NSR-JSR diffusional delay (ms)
        static const double av;
        static const double cstar;
        #endif

        double comp_ina (void);
        double comp_ikr(void);
        double comp_iks(void);
        double comp_ik1(void);
        double comp_ito(void);
        double comp_inak(void);
        double comp_inaca(double csm);
        double comp_icalpo(void);
        double comp_iup(void);
        double comp_ileak(void);
        double comp_inst_buffer(double c);

        double comp_rxa(double csm);
        double comp_Q(void);
        double comp_dir(double po, double Qr, double rxa, double dcj);
        double comp_dcp(double po, double Qr, double rxa);
        double vold;
        double hode,hpde;

public:
        double Pace(double stim=0);
        double PaceVClamp(double clampv);
        double setJparam(double newjp){jparam=newjp;return newjp;}
        double setdt(double dtt){hpde=dtt;return hpde;}
        double getdt(void){return hpde;}
        int getDim(void){return N;}
        double getVc(void){return Vc;}
        double getstim(void){return stim;}
```

```
        double getstimduration(void){return stimduration;}
        void ClampAP(double t, double BCL, double APD=0);//BCL ms
        CCell(void);
        virtual ~CCell();
        CCell& operator=(const CCell& cell);
        void Prepare(double BCL=300, int Iter=0);
        double *y;
        double &xm,&xh,&xj,&xr,&xs1,&xs2,&xtos,&ytos,&v,&ci,&cs,&cj,&cjp,&cp;
        double &xir,&c1,&c2,&xi1ca,&xi1ba,&xi2ca,&xi2ba,&xnai,&xtof,&ytof,&tropi,&trops;

        #ifdef ___USE_VAR_FOR_CONST
        double gca;//ica conductance
        double gtos;// ito slow conductance
        double gtof;// ito fast conductance
        double gnaca;// exchanger strength
        double gks;
        double gkr;
        double vup;
        double gna;// sodium conductance (mS/micro F)
        double gkix;// Ik1 conductance
        double gnak;

        double xnao;//mM external Na
        double xki;//mM internal K
        double xko;//mM external K
        double cao;//mM external Ca

        double taus;//       diffusional delay (ms)
        double taur;// spark lifetime (ms)
        double taua;// NSR-JSR diffusional delay (ms)
        double av;
        double cstar;
        #endif

        #ifdef ___REC_CURRENTS
        double _inaca,_ica,_iks,_ikr,_itof,_itos,_ik1,_ina,_inak,_iup;
        #endif
};

const double CCell::Vc=-80;
const double CCell::stim=80;
const double CCell::stimduration=2;


// ---------------constant parameters ------------------------------
const double CCell::temp=308.0;// temperature (K)
const double CCell::xxr=8.314;//
const double CCell::xf=96.485;// Faraday's constant
const double CCell::frt=xf/(xxr*temp);
```

```
#ifndef ___USE_VAR_FOR_CONST
const double CCell::xnao=136.0;//mM            external Na
const double CCell::xki=140.0;// mM            internal K
const double CCell::xko=5.40;//mM              external K
const double CCell::cao=1.8;// mM  external Ca
const double CCell::ek = (1.0/frt)*log(xko/xki);// K reversal potential

const double CCell::gca=182;// ica conductance
const double CCell::gtos=0.04;// ito slow conductance
const double CCell::gtof=0.11;// ito fast conductance
const double CCell::gnaca=0.84;// exchanger strength
const double CCell::gkr=0.0125;// Ikr conductance
const double CCell::gks=0.32;
const double CCell::gkix=0.3;// Ik1 conductance
const double CCell::gnak=1.5;
const double CCell::vup=0.4;//0.3;// uptake strength
const double CCell::taus=4.0;// diffusional delay (ms)
const double CCell::gna=12.0;// sodium conductance (mS/micro F)
const double CCell::taur=30.0;// spark lifetime (ms)
const double CCell::taua=100.0;// NSR-JSR diffusional delay (ms)
const double CCell::av=11.3;
const double CCell::cstar=90.0;
#endif

#endif /* ___CELL_H */
```

UC.CPP

```
#define ___REC_CURRENTS
#define ___USE_VAR_FOR_CONST

#include <iostream>
using namespace std;
#include "cell.h"
#include "cell.cpp"

int main(void)
{
        CCell cell;
        const double bcl=400.0;

        int Tn=bcl*200/cell.getdt(), bcln=bcl/cell.getdt(), durn=1/cell.getdt();
        for (int tn=0;tn<Tn;tn++)
        {
                double t=tn*cell.getdt();
                if (tn%10==0 && t>=bcl*190)cout<<t-bcl*190<<"\t"<<cell.v<<"\t"<<cell.ci<<"\n";
```

```
                if (tn%bcln < durn)
                        cell.Pace(50.0);
                else
                        cell.Pace();
        }
        return 0;
}
```

BIBLIOGRAPHY

1. Redfern WS, Carlsson L, Davis AS, Lynch WG, MacKenzie I, Palethorpe S, Siegl PKS, Strang I, Sullivan AT, Wallis R, Camm AJ, Hammond TG. Relationships between preclinical cardiac electrophysiology, clinical qt interval prolongation and torsade de pointes for a broad range of drugs: Evidence for a provisional safety margin in drug development. *Cardiovascular Research*. 2003;58:32-45

2. Milberg P, Ramtin S, Monnig G, Osada N, Wasmer K, Breithardt G, Haverkamp W, Eckardt L. Comparison of the in vitro electrophysiologic and proarrhythmic effects of amiodarone and sotalol in a rabbit model of acute atrioventricular block. *J Cardiovasc Pharm*. 2004;44:278-286

3. Abriel H, Schlapfer J, Keller DI, Gavillet B, Buclin T, Biollaz J, Stoller R, Kappenberger L. Molecular and clinical determinants of drug-induced long qt syndrome: An iatrogenic channelopathy. *Swiss Med Wkly*. 2004;134:685-694

4. Choi BR, Burton F, Salama G. Cytosolic ca2+ triggers early afterdepolarizations and torsade de pointes in rabbit hearts with type 2 long qt syndrome. *J Physiol-London*. 2002;543:615-631

5. Nemec J, Kim JJ, Gabris B, Salama G. Calcium oscillations and t-wave lability precede ventricular arrhythmias in acquired long qt type 2. *Heart Rhythm*. 2010;7:1686-1694

6. Roden DM. Mechanisms and management of proarrhythmia. *Am J Cardiol*. 1998;82:49i-57i

7. Lawrence CL, Pollard CE, Hammond TG, Valentin JP. In vitro models of proarrhythmia. *Brit J Pharmacol*. 2008;154:1516-1522

8. Belardinelli L, Antzelevitch C, Vos MA. Assessing predictors of drug-induced torsade de pointes. *Trends Pharmacol Sci*. 2003;24:619-625

9. Mantravadi R, Gabris B, Liu T, Choi BR, de Groat WC, Ng GA, Salama G. Autonomic nerve stimulation reverses ventricular repolarization sequence in rabbit hearts. *Circulation Research*. 2007;100:E72-E80

10. Shah RR, Hondeghem LM. Refining detection of drug-induced proarrhythmia: Qt interval and triad. *Heart Rhythm*. 2005;2:758-772

11. Suzuki S, Murakami S, Tsujimae K, Findlay I, Kurachi Y. In silico risk assessment for drug-induction of cardiac arrhythmia. *Prog Biophys Mol Bio*. 2008;98:52-60

12. Yap YG, Camm AJ. Drug induced qt prolongation and torsades de pointes. *Heart*. 2003;89:1363-1372

13. International conference on harmonisation; guidance on s7b nonclinical evaluation of the potential for delayed ventricular repolarization (qt interval prolongation) by human pharmaceuticals; availability. Notice. *Fed Regist*. 2005;70:61133-61134

14. Rodriguez B, Li L, Eason JC, Efimov IR, Trayanova NA. Differences between left and right ventricular chamber geometry affect cardiac vulnerability to electric shocks. *Circulation Research*. 2005;97:168-175

15. Clayton RH, Bernus O, Cherry EM, Dierckx H, Fenton FH, Mirabella L, Panfilov AV, Sachse FB, Seemann G, Zhang H. Models of cardiac tissue electrophysiology: Progress, challenges and open questions. *Prog Biophys Mol Bio*. 2011;104:22-48

16. Cavalli A, Poluzzi E, De Ponti F, Recanatini M. Toward a pharmacophore for drugs inducing the long qt syndrome: Insights from a comfa study of herg k+ channel blockers. *J Med Chem*. 2002;45:3844-3853

17. Shannon TR, Wang F, Puglisi J, Weber C, Bers DM. A mathematical treatment of integrated ca dynamics within the ventricular myocyte. *Biophys J*. 2004;87:3351-3371

18. Puglisi JL, Bers DM. Labheart: An interactive computer model of rabbit ventricular myocyte ion channels and ca transport. *Am J Physiol-Cell Ph*. 2001;281:C2049-C2060

19. Mahajan A, Shiferaw Y, Sato D, Baher A, Olcese R, Xie LH, Yang MJ, Chen PS, Restrepo JG, Karma A, Garfinkel A, Qu Z, Weiss JN. A rabbit ventricular action potential model replicating cardiac dynamics at rapid heart rates. *Biophysical Journal*. 2008;94:392-410

20. Fox JJ, McHarg JL, Gilmour RF. Ionic mechanism of electrical alternans. *Am J Physiol-Heart C*. 2002;282:H516-H530

21. ten Tusscher KHWJ, Noble D, Noble PJ, Panfilov AV. A model for human ventricular tissue. *Am J Physiol-Heart C*. 2004;286:H1573-H1589

22. O'Hara T, Virag L, Varro A, Rudy Y. Simulation of the undiseased human cardiac ventricular action potential: Model formulation and experimental validation. *Plos Computational Biology*. 2011;7

23. Rice JJ, Jafri MS, Winslow RL. Modeling gain and gradedness of ca2+ release in the functional unit of the cardiac diadic space. *Biophysical Journal*. 1999;77:1871-1884

24. Crampin EJ, Halstead M, Hunter P, Nielsen P, Noble D, Smith N, Tawhai M. Computational physiology and the physiome project. *Experimental Physiology*. 2004;89:1-26

25. Hodgkin AL, Huxley AF. A quantitative description of membrane current and its application to conduction and excitation in nerve. *J Physiol*. 1952;117:500-544

26. Luo CH, Rudy Y. A model of the ventricular cardiac action potential. Depolarization, repolarization, and their interaction. *Circ Res*. 1991;68:1501-1526

27. Winslow RL, Rice J, Jafri S, Marban E, O'Rourke B. Mechanisms of altered excitation-contraction coupling in canine tachycardia-induced heart failure, ii: Model studies. *Circ Res*. 1999;84:571-586

28. Cheng H, Lederer WJ, Cannell MB. Calcium sparks: Elementary events underlying excitation-contraction coupling in heart muscle. *Science*. 1993;262:740-744

29. Wang SQ, Song LS, Lakatta EG, Cheng H. Ca2+ signalling between single l-type ca2+ channels and ryanodine receptors in heart cells. *Nature*. 2001;410:592-596

30. Bers D. *Excitation-contraction coupling and cardiac contractile force*. Dordrecht:Kluwer Academic Publishers; 2001.

31. Eisner DA, Kashimura T, Venetucci LA, Trafford AW. From the ryanodine receptor to cardiac arrhythmias. *Circ J*. 2009;73:1561-1567

32. Bassani JW, Yuan W, Bers DM. Fractional sr ca release is regulated by trigger ca and sr ca content in cardiac myocytes. *Am J Physiol*. 1995;268:C1313-1319

33. Lukyanenko V, Subramanian S, Gyorke I, Wiesner TF, Gyorke S. The role of luminal ca2+ in the generation of ca2+ waves in rat ventricular myocytes. *J Physiol*. 1999;518 (Pt 1):173-186

34. Sitsapesan R, Williams AJ. Regulation of current flow through ryanodine receptors by luminal ca2+. *J Membr Biol*. 1997;159:179-185

35. Piacentino V, 3rd, Weber CR, Chen X, Weisser-Thomas J, Margulies KB, Bers DM, Houser SR. Cellular basis of abnormal calcium transients of failing human ventricular myocytes. *Circ Res*. 2003;92:651-658

36. Diaz ME, Graham HK, Trafford AW. Enhanced sarcolemmal ca2+ efflux reduces sarcoplasmic reticulum ca2+ content and systolic ca2+ in cardiac hypertrophy. *Cardiovasc Res*. 2004;62:538-547

37. Clarke B, Wyatt KM, McCormack JG. Ranolazine increases active pyruvate dehydrogenase in perfused normoxic rat hearts: Evidence for an indirect mechanism. *Journal of Molecular and Cellular Cardiology*. 1996;28:341-350

38. McCormack JG, Barr RL, Wolff AA, Lopaschuk GD. Ranolazine stimulates glucose oxidation in normoxic, ischemic, and reperfused ischemic rat hearts. *Circulation*. 1996;93:135-142

39. Sabbah HN, Chandler MP, Mishima T, Suzuki G, Chaudhry P, Nass O, Biesiadecki BJ, Blackburn B, Wolff A, Stanley WC. Ranolazine, a partial fatty acid oxidation (pfox) inhibitor, improves left ventricular function in dogs with chronic heart failure. *Journal of Cardiac Failure*. 2002;8:416-422

40. Wu L, Shryock JC, Song Y, Li Y, Antzelevitch C, Belardinelli L. Antiarrhythmic effects of ranolazine in a guinea pig in vitro model of long-qt syndrome. *Journal of Pharmacology and Experimental Therapeutics*. 2004;310:599-605

41. Antoons G, Oros A, Beekman JD, Engelen MA, Houtman MJ, Belardinelli L, Stengl M, Vos MA. Late na(+) current inhibition by ranolazine reduces torsades de pointes in the chronic atrioventricular block dog model. *Journal of the American College of Cardiology*. 2010;55:801-809

42. Antzelevitch C, Belardinelli L, Zygmunt AC, Burashnikov A, Di Diego JM, Fish JM, Cordeiro JM, Thomas G. Electrophysiological effects of ranolazine, a novel antianginal agent with antiarrhythmic properties. *Circulation*. 2004;110:904-910

43. Abrams J, Jones CA, Kirkpatrick P. Ranolazine. *Nature Reviews Drug Discovery*. 2006;5:453-454

44. Belardinelli L, Shryock JC, Fraser H. Inhibition of the late sodium current as a potential cardioprotective principle: Effects of the late sodium current inhibitor ranolazine. *Heart*. 2006;92 Suppl 4:iv6-iv14

45. Antzelevitch C, Burashnikov A, Sicouri S, Belardinelli L. Electrophysiologic basis for the antiarrhythmic actions of ranolazine. *Heart Rhythm*. 2011;8:1281-1290

46. Choi BR, Salama G. Simultaneous maps of optical action potentials and calcium transients in guinea-pig hearts: Mechanisms underlying concordant alternans. *J Physiol*. 2000;529 Pt 1:171-188

47. Salama G, Hwang SM. Simultaneous optical mapping of intracellular free calcium and action potentials from langendorff perfused hearts. *Curr Protoc Cytom*. 2009;Chapter 12:Unit 12 17

48. Meissner G, Henderson JS. Rapid calcium release from cardiac sarcoplasmic reticulum vesicles is dependent on ca2+ and is modulated by mg2+, adenine nucleotide, and calmodulin. *J Biol Chem*. 1987;262:3065-3073

49. Ye Y, Yaeger D, Owen LJ, Escobedo JO, Wang J, Singer JD, Strongin RM, Abramson JJ. Designing calcium release channel inhibitors with enhanced electron donor properties: Stabilizing the closed state of ryr1. *Mol Pharmacol*. 2011

50. Pessah IN, Stambuk RA, Casida JE. Ca2+-activated ryanodine binding: Mechanisms of sensitivity and intensity modulation by mg2+, caffeine, and adenine nucleotides. *Mol Pharmacol*. 1987;31:232-238

51. Mahajan A, Shiferaw Y, Sato D, Baher A, Olcese R, Xie LH, Yang MJ, Chen PS, Restrepo JG, Karma A, Garfinkel A, Qu Z, Weiss JN. A rabbit ventricular action potential model replicating cardiac dynamics at rapid heart rates. *Biophys J*. 2008;94:392-410

52. Sims C, Reisenweber S, Viswanathan PC, Choi BR, Walker WH, Salama G. Sex, age, and regional differences in l-type calcium current are important determinants of arrhythmia phenotype in rabbit hearts with drug-induced long qt type 2. *Circulation Research*. 2008;102:E86-E100

53. Bers DM, Puglisi JL. Labheart: An interactive computer model of rabbit ventricular myocyte ion channels and ca transport. *Am J Physiol-Cell Ph*. 2001;281:C2049-C2060

54. Antzelevitch C, Belardinelli L, Wu L, Fraser H, Zygmunt AC, Burashnikov A, Di Diego JM, Fish JM, Cordeiro JM, Goodrow RJ, Jr., Scornik F, Perez G. Electrophysiologic properties and antiarrhythmic actions of a novel antianginal agent. *J Cardiovasc Pharmacol Ther*. 2004;9 Suppl 1:S65-83

55. Rajamani S, Shryock JC, Belardinelli L. Rapid kinetic interactions of ranolazine with herg k+ current. *J Cardiovasc Pharmacol*. 2008;51:581-589

56. Morrow DA, Scirica BM, Karwatowska-Prokopczuk E, Skene A, McCabe CH, Braunwald E. Evaluation of a novel anti-ischemic agent in acute coronary syndromes: Design and rationale for the metabolic efficiency with ranolazine for less ischemia in non-st-elevation acute coronary syndromes (merlin)-timi 36 trial. *Am Heart J*. 2006;152:400-406

57. Murdock DK, Overton N, Kersten M, Kaliebe J, Devecchi F. The effect of ranolazine on maintaining sinus rhythm in patients with resistant atrial fibrillation. *Indian Pacing Electrophysiol J*. 2008;8:175-181

58. Wasserstrom JA, Sharma R, O'Toole MJ, Zheng J, Kelly JE, Shryock J, Belardinelli L, Aistrup GL. Ranolazine antagonizes the effects of increased late sodium current on intracellular calcium cycling in rat isolated intact heart. *J Pharmacol Exp Ther*. 2009;331:382-391

59. Hilliard FA, Steele DS, Laver D, Yang Z, Le Marchand SJ, Chopra N, Piston DW, Huke S, Knollmann BC. Flecainide inhibits arrhythmogenic ca2+ waves by open state block of ryanodine receptor ca2+ release channels and reduction of ca2+ spark mass. *Journal of Molecular and Cellular Cardiology*. 2010;48:293-301

60. Viswanathan PC, Shaw RM, Rudy Y. Effects of ikr and iks heterogeneity on action potential duration and its rate dependence : A simulation study. *Circulation*. 1999;99:2466-2474

61. Wang W-Q, Robertson C, Dhalla AK, Belardinelli L. Antitorsadogenic effects of (±)-n-(2,6-dimethyl-phenyl)-(4[2-hydroxy-3-(2-methoxyphenoxy)propyl]-1-piperazine (ranolazine) in anesthetized rabbits. *Journal of Pharmacology and Experimental Therapeutics*. 2008;325:875-881

62. Yang XY, Jiang SQ, Zhang L, Liu QN, Gong PL. Inhibitory effect of dauricine on inflammatory process following focal cerebral ischemia/reperfusion in rats. *Am J Chinese Med*. 2007;35:477-486

63. Zhao J, Lian Y, Lu C, Jing L, Yuan H, Peng S. Inhibitory effects of a bisbenzylisoquinline alkaloid dauricine on herg potassium channels. *J Ethnopharmacol*. 2011

64. Wu YJ, Fang DC. Quantitative studies on dauricine block of cardiac sodium-channels. *Acta Pharm Sinic*. 1992;13:55-58

65. Xia JS, Guo DL, Zhang Y, Zhou ZN, Zeng FD, Hu CJ. Inhibitory effects of dauricine on potassium currents in guinea pig ventricular myocytes. *Acta Pharm Sinic*. 2000;21:60-64

66. Chai S, To KK, Lin G. Circumvention of multi-drug resistance of cancer cells by chinese herbal medicines. *Chin Med*. 2010;5:26

67. Tang XD, Zhou X, Zhou KY. Dauricine inhibits insulin-like growth factor-i-induced hypoxia inducible factor 1alpha protein accumulation and vascular endothelial growth factor expression in human breast cancer cells. *Acta Pharmacol Sin*. 2009;30:605-616

68. Mahajan A, Sato D, Shiferaw Y, Baher A, Xie LH, Peralta R, Olcese R, Garfinkel A, Qu Z, Weiss JN. Modifying l-type calcium current kinetics: Consequences for cardiac excitation and arrhythmia dynamics. *Biophysical Journal*. 2008;94:411-423

69. January CT, Riddle JM, Salata JJ. A model for early afterdepolarizations: Induction with the ca2+ channel agonist bay k 8644. *Circulation Research*. 1988;62:563-571

70. Nemec J, Kim JJ, Gabris B, Salama G. Calcium oscillations and t-wave lability precede ventricular arrhythmias in acquired long qt type 2. *Heart Rhythm*. 2010;7:1686-1694

71. January CT, Riddle JM. Early afterdepolarizations: Mechanism of induction and block. A role for l-type ca2+ current. *Circulation Research*. 1989;64:977-990

72. Madhvani RV, Xie Y, Pantazis A, Garfinkel A, Qu Z, Weiss JN, Olcese R. Shaping a new ca2+ conductance to suppress early afterdepolarizations in cardiac myocytes. *J Physiol*. 2011;589:6081-6092

73. Antoons G, Volders PGA, Stankovicova T, Bito V, Stengl M, Vos MA, Sipido KR. Window ca2+ current and its modulation by ca2+ release in hypertrophied cardiac myocytes from dogs with chronic atrioventricular block. *J Physiol*. 2007;579:147-160

74. Henry C T. Quantitative aspects of l-type ca2+ currents. *Progress in Neurobiology*. 2012;96:1-31

75. Tuckwell HC. Quantitative aspects of l-type ca2+ currents. *Prog Neurobiol*. 2012;96:1-31

76. Efimov IR, Huang DT, Rendt JM, Salama G. Optical mapping of repolarization and refractoriness from intact hearts. *Circulation*. 1994;90:1469-1480

77. Salama G, Kanai A, Efimov IR. Subthreshold stimulation of purkinje-fibers interrupts ventricular-tachycardia in intact hearts - experimental-study with voltage-sensitive dyes and imaging techniques. *Circulation Research*. 1994;74:604-619

78. Liu QN, Zhang L, Gong PL, Yang XY, Zeng FD. Inhibitory effects of dauricine on early afterdepolarizations and l-type calcium current. *Can J Physiol Pharm*. 2009;87:954-962

79. Shannon TR, Wang F, Puglisi J, Weber C, Bers DM. A mathematical treatment of integrated ca dynamics within the ventricular myocyte. *Biophysical Journal*. 2004;87:3351-3371

80. Parikh A, Mantravadi R, Kozhevnikov D, Roche MA, Ye Y, Owen LJ, Puglisi JL, Abramson JJ, Salama G. Ranolazine stabilizes cardiac ryanodine receptors: A novel mechanism for the suppression of early afterdepolarization and torsades de pointes in long qt type 2. *Heart Rhythm*. 2012

81. Choi BR, Salama G. Simultaneous maps of optical action potentials and calcium transients in guinea-pig hearts: Mechanisms underlying concordant alternans. *J Physiol-London*. 2000;529:171-188

82. Baker LC, London B, Choi BR, Koren G, Salama G. Enhanced dispersion of repolarization and refractoriness in transgenic mouse hearts promotes reentrant ventricular tachycardia. *Circulation Research*. 2000;86:396-407

83. Yang Z, Li C, Wang X, Zhai C, Yi Z, Wang L, Liu B, Du B, Wu H, Guo X, Liu M, Li D, Luo J. Dauricine induces apoptosis, inhibits proliferation and invasion through inhibiting nf-kappab signaling pathway in colon cancer cells. *J Cell Physiol*. 2010;225:266-275

84. Xia JS, Guo DL, Zhang Y, Zhou ZN, Zeng FD, Hu CJ. Inhibitory effects of dauricine on potassium currents in guinea pig ventricular myocytes. *Acta Pharmacol Sin*. 2000;21:60-64

85. Liu T, Choi BR, Drici MD, Salama G. Sex modulates the arrhythmogenic substrate in prepubertal rabbit hearts with long qt 2. *J Cardiovasc Electrophysiol*. 2005;16:516-524

86. Splawski I, Timothy KW, Sharpe LM, Decher N, Kumar P, Bloise R, Napolitano C, Schwartz PJ, Joseph RM, Condouris K, Tager-Flusberg H, Priori SG, Sanguinetti MC, Keating MT. Ca(v)1.2 calcium channel dysfunction causes a multisystem disorder including arrhythmia and autism. *Cell*. 2004;119:19-31

87. Sicouri S, Timothy KW, Zygmunt AC, Glass A, Goodrow RJ, Belardinelli L, Antzelevitch C. Cellular basis for the electrocardiographic and arrhythmic manifestations of timothy syndrome: Effects of ranolazine. *Heart Rhythm*. 2007;4:638-647

88. Best JM, Kamp TJ. A sympathetic model of l-type ca2+ channel-triggered arrhythmias. *Am J Physiol Heart Circ Physiol*. 2010;298:H3-4

89. Arikkath J, Campbell KP. Auxiliary subunits: Essential components of the voltage-gated calcium channel complex. *Curr Opin Neurobiol*. 2003;13:298-307

90. Piepho R. Pharmacology of the calcium channel blockers

91. Gudzenko V, Shiferaw Y, Savalli N, Vyas R, Weiss JN, Olcese R. Influence of channel subunit composition on l-type ca2+ current kinetics and cardiac wave stability. *Am J Physiol Heart Circ Physiol*. 2007;293:H1805-1815

92. Keyan F. A clinical analysis of 402 arrhythmia cases treated with dauricine. *Journal of Clinical Cardiology*. 1989;04

93. Zhou ZM. Dauricine caused first-degree atrioventricular block and complete left bundle branch block: A case report. *New Drugs and Clinical Remedies*. 1985;6:32

94. Triggle DJ. Calcium-channel antagonists: Mechanisms of action, vascular selectivities, and clinical relevance. *Cleve Clin J Med*. 1992;59:617-627

95. Fuster V, Ryden LE, Cannom DS, Crijns HJ, Curtis AB, Ellenbogen KA, Halperin JL, Le Heuzey JY, Kay GN, Lowe JE, Olsson SB, Prystowsky EN, Tamargo JL, Wann S, Smith SC, Jr., Jacobs AK, Adams CD, Anderson JL, Antman EM, Halperin JL, Hunt SA, Nishimura R, Ornato JP, Page RL, Riegel B, Priori SG, Blanc JJ, Budaj A, Camm AJ, Dean V, Deckers JW, Despres C, Dickstein K, Lekakis J, McGregor K, Metra M, Morais J, Osterspey A, Tamargo JL, Zamorano JL. Acc/aha/esc 2006 guidelines for the management of patients with atrial fibrillation: A report of the american college of cardiology/american heart association task force on practice guidelines and the european society of cardiology committee for practice guidelines (writing committee to revise the 2001 guidelines for the management of patients with atrial fibrillation): Developed in collaboration with the european heart rhythm association and the heart rhythm society. *Circulation*. 2006;114:e257-354

96. Jalife ANaJ. Atrial fibrillation: From bench to beside 2008

97. Yue LX, Feng JL, Gaspo R, Li GR, Wang ZG, Nattel S. Ionic remodeling underlying action potential changes in a canine model of atrial fibrillation. *Circulation Research*. 1997;81:512-525

98. Van Wagoner DR, Pond AL, Lamorgese M, Rossie SS, McCarthy PM, Nerbonne JM. Atrial l-type ca2+ currents and human atrial fibrillation. *Circulation Research*. 1999;85:428-436

99. Nishida K, Michael G, Dobrev D, Nattel S. Animal models for atrial fibrillation: Clinical insights and scientific opportunities. *Europace*. 2010;12:160-172

100. Dobrev D, Voigt N, Wehrens XH. The ryanodine receptor channel as a molecular motif in atrial fibrillation: Pathophysiological and therapeutic implications. *Cardiovascular research*. 2011;89:734-743

101. Hove-Madsen L, Llach A, Bayes-Genis A, Roura S, Rodriguez Font E, Aris A, Cinca J. Atrial fibrillation is associated with increased spontaneous calcium release from the sarcoplasmic reticulum in human atrial myocytes. *Circulation*. 2004;110:1358-1363

102. El-Armouche A, Boknik P, Eschenhagen T, Carrier L, Knaut M, Ravens U, Dobrev D. Molecular determinants of altered ca2+ handling in human chronic atrial fibrillation. *Circulation*. 2006;114:670-680

103. Lai LP, Su MJ, Lin JL, Lin FY, Tsai CH, Chen YS, Huang SK, Tseng YZ, Lien WP. Down-regulation of l-type calcium channel and sarcoplasmic reticular ca(2+)-atpase mrna in human atrial fibrillation without significant change in the mrna of ryanodine receptor, calsequestrin and phospholamban: An insight into the mechanism of atrial electrical remodeling. *Journal of the American College of Cardiology*. 1999;33:1231-1237

104. Brundel BJ, van Gelder IC, Henning RH, Tuinenburg AE, Deelman LE, Tieleman RG, Grandjean JG, van Gilst WH, Crijns HJ. Gene expression of proteins influencing the calcium homeostasis in patients with persistent and paroxysmal atrial fibrillation. *Cardiovascular research*. 1999;42:443-454

105. Gaspo R, Bosch RF, Bou-Abboud E, Nattel S. Tachycardia-induced changes in na+ current in a chronic dog model of atrial fibrillation. *Circ Res*. 1997;81:1045-1052

106. Gaspo R, Bosch RF, Talajic M, Nattel S. Functional mechanisms underlying tachycardia-induced sustained atrial fibrillation in a chronic dog model. *Circulation*. 1997;96:4027-4035

107. van der Velden HM, Ausma J, Rook MB, Hellemons AJ, van Veen TA, Allessie MA, Jongsma HJ. Gap junctional remodeling in relation to stabilization of atrial fibrillation in the goat. *Cardiovascular research*. 2000;46:476-486

108. Goodenough DA, Paul DL. Gap junctions. *Cold Spring Harb Perspect Biol*. 2009;1:a002576

109. Delmar M. Connexin43 regulates sodium current; ankyrin-g modulates gap junctions: The intercalated disc exchanger. *Cardiovascular Research*. 2012;93:220-222

110. Burstein B, Nattel S. Atrial fibrosis: Mechanisms and clinical relevance in atrial fibrillation. *J Am Coll Cardiol*. 2008;51:802-809

111. de Jong S, van Veen TA, de Bakker JM, van Rijen HV. Monitoring cardiac fibrosis: A technical challenge. *Neth Heart J*. 2012;20:44-48

112. de Jong S, van Veen TA, van Rijen HV, de Bakker JM. Fibrosis and cardiac arrhythmias. *J Cardiovasc Pharmacol*. 2011;57:630-638

113. Burstein B, Comtois P, Michael G, Nishida K, Villeneuve L, Yeh YH, Nattel S. Changes in connexin expression and the atrial fibrillation substrate in congestive heart failure. *Circulation Research*. 2009;105:1213-1222

114. Nattel S, Maguy A, Le Bouter S, Yeh YH. Arrhythmogenic ion-channel remodeling in the heart: Heart failure, myocardial infarction, and atrial fibrillation. *Physiol Rev*. 2007;87:425-456

115. Aldhoon B, Melenovsky V, Peichl P, Kautzner J. New insights into mechanisms of atrial fibrillation. *Physiol Res*. 2010;59:1-12

116. Anter E, Callans DJ. Pharmacological and electrical conversion of atrial fibrillation to sinus rhythm is worth the effort. *Circulation*. 2009;120:1436-1443

117. Xiao HD, Fuchs S, Campbell DJ, Lewis W, Dudley SC, Kasi VS, Hoit BD, Keshelava G, Zhao H, Capecchi MR, Bernstein KE. Animal model - mice with cardiac-restricted angiotensin-converting enzyme (ace) have atrial enlargement, cardiac arrhythmia, and sudden death. *Am J Pathol*. 2004;165:1019-1032

118. Fuster V, Ryden LE, Cannom DS, Crijns HJ, Curtis AB, Ellenbogen KA, Halperin JL, Le Heuzey JY, Kay GN, Lowe JE, Olsson SB, Prystowsky EN, Tamargo JL, Wann S. Acc/aha/esc 2006 guidelines for the management of patients with atrial fibrillation-executive summary: A report of the american college of cardiology/american heart association task force on practice guidelines and the european society of cardiology committee for practice guidelines (writing committee to revise the 2001 guidelines for the management of patients with atrial fibrillation). *Eur Heart J*. 2006;27:1979-2030

119. Verheule S, Sato T, Everett Tt, Engle SK, Otten D, Rubart-von der Lohe M, Nakajima HO, Nakajima H, Field LJ, Olgin JE. Increased vulnerability to atrial fibrillation in transgenic mice with selective atrial fibrosis caused by overexpression of tgf-beta1. *Circulation Research*. 2004;94:1458-1465

120. Liao CH, Akazawa H, Tamagawa M, Ito K, Yasuda N, Kudo Y, Yamamoto R, Ozasa Y, Fujimoto M, Wang P, Nakauchi H, Nakaya H, Komuro I. Cardiac mast cells cause atrial fibrillation through pdgf-a-mediated fibrosis in pressure-overloaded mouse hearts. *J Clin Invest*. 2010;120:242-253

121. Aliot E, Ruskin JN. Controversies in ablation of atrial fibrillation. *Eur Heart J Suppl*. 2008;10:H32-H54

122. Chen SA, Tai CT, Yeh HI, Chen YJ, Lin CI. Controversies in the mechanisms and ablation of pulmonary vein atrial fibrillation. *Pace*. 2003;26:1301-1307

123. Fuster V, Ryden LE, Asinger RW, Cannom DS, Crijns HJ, Frye RL, Halperin JL, Kay GN, Klein WW, Levy S, McNamara RL, Prystowsky EN, Wann LS, Wyse DG, Gibbons RJ, Antman EM, Alpert JS, Faxon DP, Gregoratos G, Hiratzka LF, Jacobs AK, Russell RO, Smith SC, Alonso-Garcia A, Blomstrom-Lundqvist C, De Backer G, Flather M, Hradec J, Oto A, Parkhomenko A, Silber S, Torbicki A. Acc/aha/esc guidelines for the management of patients with atrial fibrillation: Executive summary. A report of the american college of cardiology/ american heart association task force on practice guidelines and the european society of cardiology committee for practice guidelines and policy conferences (committee to develop guidelines for the management of patients with atrial fibrillation): Developed in collaboration with the north american society of pacing and electrophysiology. *J Am Coll Cardiol*. 2001;38:1231-1266

124. Bani D, Yue SK, Bigazzi M. Clinical profile of relaxin, a possible new drug for human use. *Curr Drug Saf*. 2009;4:238-249

125. Teichman SL, Unemori E, Dschietzig T, Conrad K, Voors AA, Teerlink JR, Felker GM, Metra M, Cotter G. Relaxin, a pleiotropic vasodilator for the treatment of heart failure. *Heart Fail Rev*. 2009;14:321-329

126. Du XJ, Samuel CS, Gao XM, Zhao L, Parry LJ, Tregear GW. Increased myocardial collagen and ventricular diastolic dysfunction in relaxin deficient mice: A gender-specific phenotype. *Cardiovasc Res*. 2003;57:395-404

127. Lekgabe ED, Kiriazis H, Zhao C, Xu Q, Moore XL, Su Y, Bathgate RA, Du XJ, Samuel CS. Relaxin reverses cardiac and renal fibrosis in spontaneously hypertensive rats. *Hypertension*. 2005;46:412-418

128. Nishida K, Michael G, Dobrev D, Nattel S. Animal models for atrial fibrillation: Clinical insights and scientific opportunities. *Europace*. 2009

129. Okamoto K, Aoki K. Development of a strain of spontaneously hypertensive rats. *Jpn Circ J*. 1963;27:282-293

130. Doggrell SA, Brown L. Rat models of hypertension, cardiac hypertrophy and failure. *Cardiovascular Research*. 1998;39:89-105

131. Choisy SC, Arberry LA, Hancox JC, James AF. Increased susceptibility to atrial tachyarrhythmia in spontaneously hypertensive rat hearts. *Hypertension*. 2007;49:498-505

132. Samuel CS, Unemori EN, Mookerjee I, Bathgate RA, Layfield SL, Mak J, Tregear GW, Du XJ. Relaxin modulates cardiac fibroblast proliferation, differentiation, and collagen production and reverses cardiac fibrosis in vivo. *Endocrinology*. 2004;145:4125-4133

133. Debrah DO, Conrad KP, Danielson LA, Shroff SG. Effects of relaxin on systemic arterial hemodynamics and mechanical properties in conscious rats: Sex dependency and dose response. *J Appl Physiol*. 2005;98:1013-1020

134. Debrah DO, Debrah JE, Haney JL, McGuane JT, Sacks MS, Conrad KP, Shroff SG. Relaxin regulates vascular wall remodeling and passive mechanical properties in mice. *J Appl Physiol*. 2011

135. Marques FD, Ferreira AJ, Sinisterra RDM, Jacoby BA, Sousa FB, Caliari MV, Silva GAB, Melo MB, Nadu AP, Souza LE, Irigoyen MCC, Almeida AP, Santos RAS. An oral formulation of angiotensin-(1-7) produces cardioprotective effects in infarcted and isoproterenol-treated rats. *Hypertension*. 2011;57:477-U261

136. Ziv O, Morales E, Song YK, Peng XW, Odening KE, Buxton AE, Karma A, Koren G, Choi BR. Origin of complex behaviour of spatially discordant alternans in a transgenic rabbit model of type 2 long qt syndrome. *J Physiol-London*. 2009;587:4661-4680

137. Frustaci A, Caldarulo M, Buffon A, Bellocci F, Fenici R, Melina D. Cardiac biopsy in patients with primary atrial-fibrillation - histologic evidence of occult myocardial diseases. *Chest*. 1991;100:303-306

138. Dobrev D, Nattel S. New antiarrhythmic drugs for treatment of atrial fibrillation. *Lancet*. 2010;375:1212-1223

139. Moe GK. On the multiple wavelet hypothesis of atrial fibrillation. *Arch Int Pharmacodyn Ther*. 1962;140:183-188

140. Haissaguerre M, Jais P, Shah DC, Takahashi A, Hocini M, Quiniou G, Garrigue S, Le Mouroux A, Le Metayer P, Clementy J. Spontaneous initiation of atrial fibrillation by ectopic beats originating in the pulmonary veins. *New Engl J Med*. 1998;339:659-666

141. Moe GK. Evidence for reentry as a mechanism of cardiac-arrhythmias. *Rev Physiol Bioch P*. 1975;72:55-81

142. Du XJ, Bathgate RA, Samuel CS, Dart AM, Summers RJ. Cardiovascular effects of relaxin: From basic science to clinical therapy. *Nat Rev Cardiol*. 2010;7:48-58

143. Samuel CS, Unemori EN, Mookerjee I, Bathgate RAD, Layfield SL, Mak J, Tregear GW, Du XJ. Relaxin modulates cardiac fibroblast proliferation, differentiation, and collagen production and reverses cardiac fibrosis in vivo. *Endocrinology*. 2004;145:4125-4133

144. Lee KW, Everett TH, Rahmutula D, Guerra JM, Wilson E, Ding CH, Olgin JE. Pirfenidone prevents the development of a vulnerable substrate for atrial fibrillation in a canine model of heart failure. *Circulation*. 2006;114:1703-1712

145. Ponikowski P, Metra M, Teerlink JR, Unemori E, Felker GM, Voors AA, Filippatos G, Greenberg B, Teichman SL, Severin T, Mueller-Velten G, Cotter G, Davison BA. Design of the relaxin in acute heart failure study. *Am Heart J*. 2012;163:149-U234

146. Voors AA, Davison BA, Felker GM, Ponikowski P, Unemori E, Cotter G, Teerlink JR, Greenberg BH, Filippatos G, Teichman SL, Metra M, Grp P-R-AS. Early drop in systolic blood pressure and worsening renal function in acute heart failure: Renal results of pre-relax-ahf. *Eur J Heart Fail*. 2011;13:961-967

147. Dickhout JG, Lee RM. Blood pressure and heart rate development in young spontaneously hypertensive rats. *Am J Physiol*. 1998;274:H794-800

148. Khanna D, Clements PJ, Furst DE, Korn JH, Ellman M, Rothfield N, Wigley FM, Moreland LW, Silver R, Kim YH, Steen VD, Firestein GS, Kavanaugh AF, Weisman M, Mayes MD, Collier D, Csuka ME, Simms R, Merkel PA, Medsger TA, Sanders ME, Maranian P, Seibold JR, Scleroderm RI. Recombinant human relaxin in the treatment of systemic sclerosis with diffuse cutaneous involvement a randomized, double-blind, placebo-controlled trial. *Arthritis Rheum-Us*. 2009;60:1102-1111